Aix*Marseille université
Socialement engagée

NNT : 2024AIXM0001

THÈSE DE DOCTORAT

Soutenue à Aix-Marseille Université
le 12 juillet 2024 par

Kseniia LEZHENNIKOVA

Manipulation of Electromagnetic Near-field Interactions

Discipline
Physique et sciences de la matière

Spécialité
Optique, Photonique et Traitement d'Image

École doctorale
ED 352 Physique et sciences de la matière

Laboratoire/Partenaires de recherche
Institut Fresnel, CNRS
Multiwave Technologies SAS

Composition du jury

Julien de Rosny Institut Langevin	Rapporteur
Matthieu Davy University of Rennes	Rapporteur
Anne Sentenac Aix Marseille University	Examinatrice
Stanislav Glybovski ITMO University	Examinateur
Boris Kuhlmey University of Sydney	Examinateur
Frédérique Gadot Université Paris Nanterre	Président du Jury
Stefan Enoch Aix Marseille University	Directeur de thèse
Redha Abdeddaim Aix Marseille University	Co-Directeur de thèse

Multiwave Technologies

INSTITUT FRESNEL MARSEILLE

Affidavit

I, undersigned, Kseniia Lezhennikova, hereby declare that the work presented in this manuscript is my own work, carried out under the scientific supervision of Stefan Enoch, in accordance with the principles of honesty, integrity and responsibility inherent to the research mission. The research work and the writing of this manuscript have been carried out in compliance with both the french national charter for Research Integrity and the Aix-Marseille University charter on the fight against plagiarism.

This work has not been submitted previously either in this country or in another country in the same or in a similar version to any other examination body.

Marseille 21/05/2024



This work is licensed under Creative Commons Attribution-NonCommercial-NoDerivatives 4.0 International Public License

Liste de publications et participation aux conférences

Liste des publications et/ou brevets réalisées dans le cadre du projet de thèse :

1. Kseniia LEZHENNIKOVA, Kaizad RUSTOMJI, Boris T. KUHLMEY, Tryfon ANTONAKAKIS, Pierre JOMIN, Stanislav GLYBOVSKI, C. Martijn DE STERKE, Jérôme WENGER, Redha ABDEDDAIM et Stefan ENOCH. « Experimental evidence of Förster energy transfer enhancement in the near field through engineered metamaterial surface waves ». en. In : *Communications Physics* 6.1 (2023), p. 229. ISSN : 2399-3650. DOI : 10.1038/s42005-023-01347-1
2. Ilya DERIY, Ksenia LEZHENNIKOVA, Stanislav GLYBOVSKI, Pavel BELOV, Ivan IORSH, Mingzhao SONG et Andrey BOGDANOV. « No reflection paradox at the boundary of hyperbolic medium ». In : *Optical Manipulation and Structured Materials Conference*. Sous la dir. de Takashige OMATSU, Síle N. CHORMAIC et Kishan DHOLAKIA. Yokohama, Japan : SPIE, sept. 2023, p. 45. DOI : 10.1117/12.3008377
3. Kseniia LEZHENNIKOVA, Sahand MAHMOODIAN, Boris T. KUHLMEY, Redha ABDEDDAIM, Stefan ENOCH, C. Martijn DE STERKE et Alessandro TUNIZ. « Broadband Terahertz Near-Field Excitation and Detection of Silicon Photonic Crystal Modes ». en. In : *ACS Photonics* 10.12 (2023), p. 4447-4455. ISSN : 2330-4022, 2330-4022. DOI : 10.1021/acsphotonics.3c01312
4. Kseniia LEZHENNIKOVA, Kaizad RUSTOMJI, Pierre JOMIN, Stanislav GLYBOVSKI, C. Martijn DE STERKE, Jerome WENGER, Redha ABDEDDAIM et Stefan ENOCH. « Microwave analogy of Förster resonance energy transfer and effect of finite antenna length ». en. In : *Scientific Reports* 14.1 (mai 2024), p. 10485. ISSN : 2045-2322. DOI : 10.1038/s41598-024-59824-8

Participation aux conférences et écoles d'été au cours de la période de thèse :

1. METANANO 2021, online conference, Oral talk
2. SPIE Photonic conference at Strasbourg, April 2022, Oral talk
3. Metamaterials 2022 Siena, Italy 12-17 September, Oral talk
4. META conference 18 - 21 July, 2023 Paris, France, Oral talk

Résumé

Cette thèse explore les interactions en champ proche et le contrôle dans les domaines de fréquence micro-onde et térahertz (THz). Dans le domaine optique, les émetteurs quantiques, tels que les atomes, les molécules et les points quantiques, sont capables d'émettre des photons dans l'environnement par émission spontanée. Le processus d'émission spontanée est affecté par l'environnement de l'émetteur à travers la densité locale des états (LDOS). Le transfert d'énergie par résonance de Förster (FRET) se produit entre des paires d'émetteurs, placées à proximité l'une de l'autre. Tout comme le LDOS, le FRET est affecté par un champ électrique proche de l'émetteur et peut être contrôlé par l'environnement. Le contrôle du FRET par l'environnement suscite un intérêt croissant ; cependant, les mesures aux fréquences optiques sont difficiles, notamment en raison de signaux faibles et d'une résolution spatiale limitée. Pour relever ces défis, des mesures d'antenne dans la gamme des micro-ondes ont été proposées comme analogie du FRET optique, afin de contourner les difficultés liées à la résolution spatiale et d'obtenir un contrôle d'orientation précis. Ce travail aborde la question de la taille de l'antenne sur les mesures de transfert d'énergie micro-onde en espace libre et à proximité d'un miroir parfaitement conducteur et propose une méthode de moyennage orienté. L'influence des métasurfaces et des cristaux photoniques (PC) sur la manipulation en champ proche est explorée. Les métasurfaces sont des structures artificielles avec une périodicité sub-longueur d'onde conçues pour avoir des propriétés uniques de contrôle des ondes électromagnétiques. Nous considérons les métasurfaces hyperboliques et un paradoxe de réflexion anormale au bord des métasurfaces hyperboliques. Ensuite, nous concevons des métasurfaces qui supportent les ondes de surface pour explorer l'amélioration du taux de FRET et sa relation avec le LDOS. Dans la plage THz, nous explorons les PC, présentant des bandes interdites photoniques et des régimes d'auto-collimation. Dans cette plage, les mesures en champ proche restent difficiles, et nous proposons un nouveau montage expérimental pour montrer les propriétés hautement dispersives du PC.

Cette thèse présente une investigation exhaustive allant des fondements théoriques aux démonstrations expérimentales. Les chapitres sont consacrés au transfert d'énergie basé sur les antennes, à l'exploration des métasurfaces et aux nouvelles mesures en champ proche dans la plage THz en utilisant des PC. La thèse se conclut en décrivant les voies futures de recherche, en expliquant la relation complexe entre les phénomènes en champ proche et en soulignant le potentiel de l'environnement photonique local pour moduler les processus de transfert d'énergie.

Mots clés : Champ proche, Transfert d'énergie, Métasurface, Cristal photonique

Abstract

This thesis explores near-field interactions and control in the microwave and Terahertz (THz) frequency domains. In the optic range, Quantum emitters, such as atoms, molecules, and quantum dots, are able to emit photons into the environment by spontaneous emission. The spontaneous emission process is characterized by the Purcell factor, which is affected by the emitter environment through the local density of states (LDOS). Förster Resonance Energy Transfer (FRET) is a phenomenon that occurs between pairs of emitters, placed near each other. FRET is widely used in solar energy harvesting, optoelectronics, biophysics, etc. Similarly to the LDOS, FRET is affected by an electric near field of the emitter and can be controlled by the environment. Controlling FRET by the environment is gaining interest; however, measurements at optical frequencies are challenging, including weak signals and limited spatial resolution. To address the challenges, antenna measurements in the microwave range were proposed as an analog of optical FRET to overcome the difficulties associated with spatial resolution and achieve precise orientation control and precise orientation control. This thesis addresses the issue of antenna size on microwave energy-transfer measurements in free-space and near a perfectly conductive mirror and proposes an orientational averaging method.

Moreover, the influence of metasurfaces and photonic crystals (PCs) on near-field manipulation is explored. Metasurfaces are artificial structures with subwavelength periodicity designed to have unique properties for electromagnetic wave control. We consider hyperbolic metasurfaces and experimentally show an anomalous reflection paradox at the edge of hyperbolic metasurfaces in the microwave range. Then, we designed metasurfaces that support surface waves to explore the energy transfer and its relationship with LDOS. In the THz frequency range, we explore PCs, exhibiting photonic band gaps and self-colimation regimes. In this range, the near-field measurements remain challenging, and we propose a novel experimental setup to show the highly dispersive properties of the PC.

This thesis presents a comprehensive investigation that ranges from theoretical foundations to experimental demonstrations. We present an antenna-based energy transfer in the microwave range, metasurface exploration, and novel near-field measurements in the THz range using photonic crystals. The thesis concludes by describing a future perspective of research, explaining the complex relationship between near-field phenomena and energy transfer mechanisms, and highlighting the potential of the local photonic environment to modulate energy transfer processes.

Keywords: Near-field, energy transfer, metasurface, photonic crystal

Résumé long

Cette thèse porte porte sur les interactions et le contrôle du champ électromagnétique proche dans les gammes de fréquences micro-ondes et terahertz (THz). Ces dernières années, l'étude et la manipulation des processus de transfert d'énergie à l'échelle nanométrique sont devenues une direction prometteuse en photonique et en nanotechnologie. Dans le domaine optique, les émetteurs quantiques, tels que les atomes, les molécules, les points quantiques ou les structures nanométriques, sont des composants impliqués dans diverses applications, y compris le traitement de l'information quantique, les communications et la détection. Les émetteurs quantiques sont capables d'émettre des photons uniques, l'énergie y est quantifiée, et l'émission se produit à la suite de processus quantiques. Ce processus est appelé émission spontanée, un processus au cours duquel un émetteur excité émet spontanément un photon et passe à un état d'énergie inférieure. Le processus d'émission spontanée est illustré sur la figure 1 (a). Le taux d'émission spontanée, qui est influencé par l'environnement de l'émetteur, est quantifié par le facteur de Purcell. Le facteur de Purcell mesure l'augmentation ou la diminution du taux d'émission par rapport à l'espace libre. Comprendre l'interaction entre les émetteurs et l'environnement, caractérisée par la densité des états optiques (DOS), la densité locale des états (LDOS) et la densité locale des états partiels (PLDOS), est crucial pour contrôler l'émission spontanée.

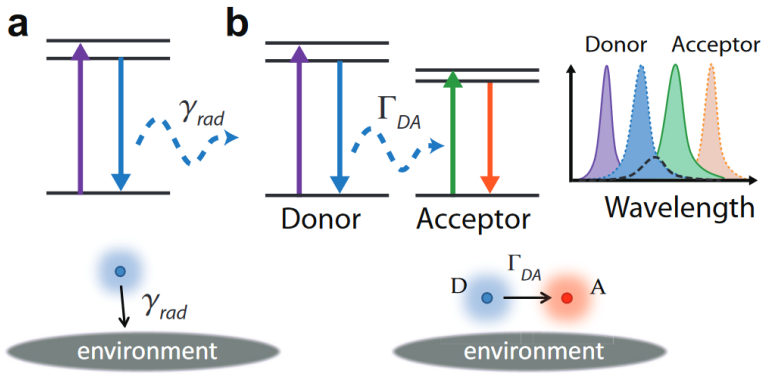

Figure 1 – (a) Diagramme des niveaux d'énergie représentant l'émission spontanée. γ_{rad} désigne le taux de transfert d'énergie radiative vers n'importe quel endroit dans l'environnement. (b) Diagramme des niveaux d'énergie montrant le FRET. Le FRET se produit lorsque deux atomes ou molécules voisins, désignés comme donneur et accepteur, ont des spectres d'émission et d'absorption qui se chevauchent et se couplent en raison d'une interaction dipôle-dipôle coulombienne. Le taux de FRET Γ_{DA} désigne le transfert d'énergie vers l'emplacement de l'accepteur uniquement.(Source: [5])

Un transfert d'énergie résonant de Förster (FRET) est un processus de transfert d'énergie en champ proche entre deux émetteurs quantiques. Il se produit lorsque deux émetteurs sont placés à proximité l'un de l'autre et que l'énergie est transférée directement sans être transmise à l'environnement et le schéma de ce processus est montré dans la figure 1. Le FRET trouve des applications dans divers domaines, notamment la récupération de l'énergie solaire, l'optoélectronique et la biophysique. Le taux de FRET dépend fortement de facteurs tels que la distance donneur-accepteur, les propriétés spectrales ains qu'à l'environnement à l'environnement de l'émetteur. Comprendre et contrôler le FRET et l'émission spontanée est important pour diverses applications, de l'optoélectronique à la biophysique.

Malgré l'intérêt significatif pour les mesures de FRET optique, certains défis persistent dans ce domaine, notamment les signaux faibles, la résolution spatiale limitée, les limitations sur l'espacement des dipoles et les défis liés au contrôle de l'orientation des dipoles. Ces limitations ne nous permettent pas de comprendre pleinement l'influence de l'environnement sur le FRET. Pour relever ces défis, une analogie entre le taux de FRET dans le domaine optique et les mesures d'antenne dans la domaine micro-ondes a été montrée dans des travaux précédents [6]. Cette analogie établit des parallèles entre les émetteurs quantiques en optique et les antennes classiques en micro-ondes et ouvre de nouvelles approches expérimentales. En utilisant des techniques micro-ondes, nous pouvons surmonter les limitations des mesures de FRET optique, offrant une force de signal améliorée, une résolution spatiale améliorée et un contrôle précis de la position des dipôles. Cependant, des défis liés à la taille de l'antenne persistent, soulignant la nécessité d'une conception et d'une analyse

expérimentales soignées.

Nous caractérisons théoriquement et expérimentalement l'amélioration du taux de transfert d'énergie par résonance de Förster (FRET) près d'un miroir parfaitement conducteur en utilisant des antennes micro-ondes. Cette géométrie de base a fait l'objet d'études théoriques précédentes [7] et d'études expérimentales [8] sur le taux de FRET. Nous avons utilisé le formalisme de la fonction de Green de [7] pour calculer l'amélioration du taux de FRET dans une large gamme de distances dipôle-dipôle R et de hauteurs dipôle-miroir h, comme indiqué dans la Figure 2 pour les orientations (a) perpendiculaire, (b) parallèle et (c) alignée.

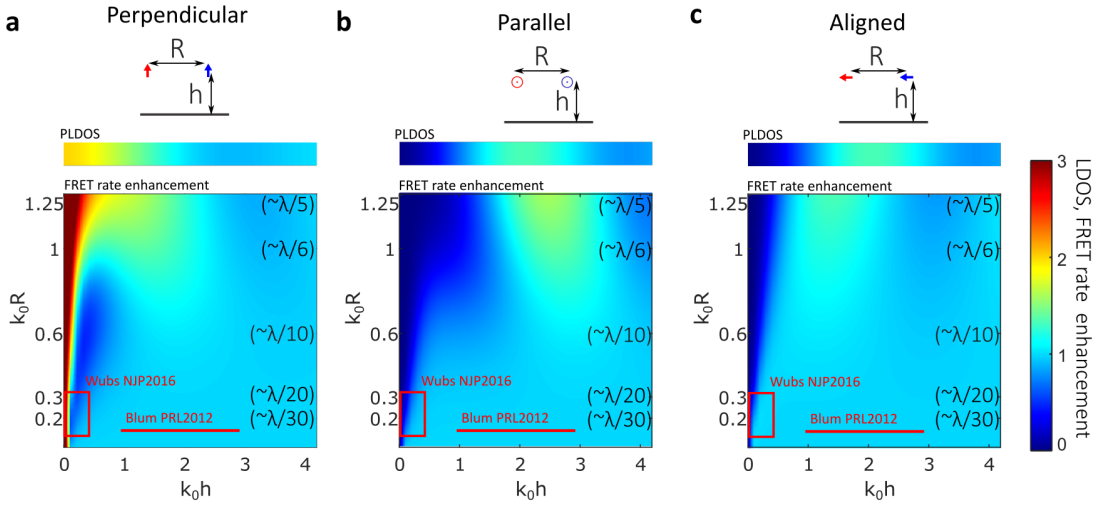

Figure 2 – Les améliorations du PLDOS et du taux de FRET près d'un miroir PEC sont calculées avec le formalisme de la fonction de Green pour les orientations (a) perpendiculaires, (b) parallèles et (c) alignées. R est la distance dipôle-dipôle, k_0 est le nombre d'onde et h est la hauteur du dipôle par rapport au miroir. Les boîtes rouges représentent les domaines relatives étudiées dans les travaux précédents en optique.

Le modèle analytique développé dans cette étude prend en compte l'effet de la taille de l'antenne sur le transfert d'énergie en calculant l'impédance mutuelle d'un réseau à deux ports composé de deux antennes identiques de taille finie. Les résultats obtenus à partir du modèle ont été confirmés par des mesures en micro-ondes près du miroir PEC, et une bonne concordance a été trouvée avec une étude théorique antérieure sur l'amélioration du taux de FRET dans le domaine optique. Nous avons noté la différence entre le transfert d'énergie pour des antennes de taille finie et l'amélioration du taux de FRET pour des dipôles ponctuels. Nous avons comparé notre modèle avec des résultats expérimentaux à haute résolution spatiale ($\Delta h = \lambda/300$ à 1 GHz et $\Delta h = \lambda/60$ à 5 GHz) et l'amélioration du taux de FRET pour les dipôles ponctuels. Pour les cas où la longueur du dipôle a un impact sur les mesures ($L > \lambda/20$), notre modèle peut nous donner une estimation de l'erreur due à la longueur du dipôle. Nous pouvons mesurer le transfert d'énergie du champ proche au régime intermédiaire pour

des séparations d'antennes R allant de $\lambda/30$ à $\lambda/6$. L'étude met également en évidence l'importance de prendre en compte l'orientation des dipôles dans l'amélioration du taux de FRET et les mesures de LDOS, qui peuvent être imitées dans le domaine des micro-ondes en mesurant le transfert d'énergie pour toutes les orientations possibles et en moyennant le résultat. Une moyenne sur les orientations pour les mesures de transfert d'énergie basées sur les antennes est une façon de comparer avec les mesures typiques de FRET optique effectuées avec un ensemble d'émetteurs ayant des moments dipolaires orientés de manière aléatoire. Les résultats ont montré une bonne concordance entre l'amélioration du taux de FRET et le transfert d'énergie moyen mesuré pour toutes les fréquences. De plus, contrairement aux métaux en micro-ondes, qui se comportent comme des miroirs conducteurs électriques (PEC) idéaux, dans le domaine optique, les métaux supportent des ondes de surface appelées plasmons de surface (SP). L'effet des SP sur le taux de FRET et la densité locale des états (LDOS) reste incertain en optique.

Le champ proche de l'émetteur peut être manipulé par des métasurfaces et des cristaux photoniques (PC). Les métasurfaces sont des structures artificielles composées de réseaux périodiques de cellule élémentaire ou de méta-atomes sublongueur d'onde. Les métasurfaces peuvent être conçues pour manipuler la phase, l'amplitude et la polarisation de l'excitation électromagnétique incidente à des échelles sublongueur d'onde. Les métasurfaces peuvent être isotropes, anisotropes et hautement anisotropes. Une métasurface isotrope ne présente aucune dépendance de ses propriétés électromagnétiques en fonction de la direction des champs, telle que la conductivité effective. En d'autres termes, l'onde électromagnétique se propage dans toutes les directions avec les mêmes propriétés. Les propriétés électromagnétiques d'une métasurface anisotrope dépendent de la direction des champs. Les cas extrêmes d'anisotropie sont appelés métasurfaces hautement anisotropes. Un exemple d'une telle métasurface est une métasurface hyperbolique, qui peut présenter des propriétés uniques. De plus, les métasurfaces peuvent être conçues pour supporter la propagation d'ondes de surface, similaires aux ondes de plasmons de surface sur des surfaces métalliques-diélectriques dans le domaine optique.

Nous avons utilisé la méthode développée pour mesurer le champ proche de la métasurface dans le domaine des micro-ondes. Nous avons considéré la métasurface hyperbolique pour montrer la résolution du paradoxe de non-réflexion à la frontière entre le milieu hyperbolique et le diélectrique isotrope. Le paradoxe de l'absence du champ réfléchi a été discuté dans la référence [9] et mentionné dans la référence [10]. La résolution de ce paradoxe a été formulée par nos collaborateurs [2] : l'onde réfléchie est présente dans le système mais décroît fortement lorsque le paramètre de perte tend vers zéro. Le paradoxe est résolu en introduisant des pertes infinitésimales dans le milieu hyperbolique. Ces modes sont concentrés à l'interface, décroissent fortement et sont généralement négligés. La conclusion contre-intuitive de cette étude est que plus les pertes sont faibles, plus le taux de décroissance des ondes fantômes est élevé. Par conséquent, toute l'énergie dispersée dans le canal réfléchi est absorbée près de l'interface.

Nous avons étudié numériquement et expérimentalement comment la présence

de l'onde de surface peut faciliter le transfert d'énergie et la LDOS. Cette influence des ondes de surface sur le taux de FRET n'a pas été étudiée en détail auparavant, principalement en raison des défis expérimentaux dans le domaine optique [11, 6, 12, 8, 13, 14]. Ici, nous surmontons ces difficultés en utilisant l'analogie du FRET dans le domaine des micro-ondes. En utilisant des antennes dipolaires et la métasurface micro-onde qui peut supporter des ondes de surface de manière similaire aux métaux en optique, nous avons pu étudier l'impact du mode de surface sur le transfert d'énergie entre les antennes. Lors de la comparaison de la métasurface dispersive avec le miroir PEC non-dispersif et non résonant discuté en détail précédemment, nous trouvons des effets qualitativement différents sur le transfert d'énergie et la LDOS. Nous avons montré que les ondes de surface augmentent le champ électrique aux positions du dipôle donneur et accepteur définies par la fonction de Green, ce qui entraîne à son tour une augmentation à la fois de la LDOS et du transfert d'énergie. Nous mettons en évidence l'influence de la métasurface en démontrant une relation linéaire importante entre le transfert d'énergie et la LDOS lorsque le donneur et l'accepteur sont proches de la métasurface. Dans le travail de [7], la relation entre la LDOS et l'amélioration du taux de FRET a déjà été étudiée pour des milieux sans absorption et sans dispersion sur l'exemple du miroir PEC à $k_0 R = \lambda/100$, où le taux de FRET ne montre pas de corrélation linéaire avec la LDOS. Dans la Figure 3 (a), nous montrons la corrélation du transfert d'énergie et de la LDOS près du miroir PEC, mais pour une distance plus grande $k_0 R$ plutôt que celle présentée dans [7]. Dans cet exemple, la LDOS et le taux de FRET n'ont toujours pas de corrélation linéaire et nous pouvons observer un comportement nettement différent pour les orientations des dipôles parallèles et perpendiculaires. Pour la métasurface, la relation entre le transfert d'énergie et la LDOS présente une tendance linéaire pour les deux orientations des dipôles lorsque les antennes sont proches de la surface. Dans ce cas, les ondes de surface jouent un rôle majeur dans le contrôle à la fois de la LDOS et du transfert d'énergie dans le champ proche. Les ondes de surface contribuent à l'augmentation du champ électrique du dipôle donneur qui définit la fonction de Green, ce qui conduit à une augmentation à la fois de la LDOS et du transfert d'énergie [15]. Par conséquent, une relation approximativement linéaire entre le transfert d'énergie et la LDOS apparaît dans le cas de la métasurface.

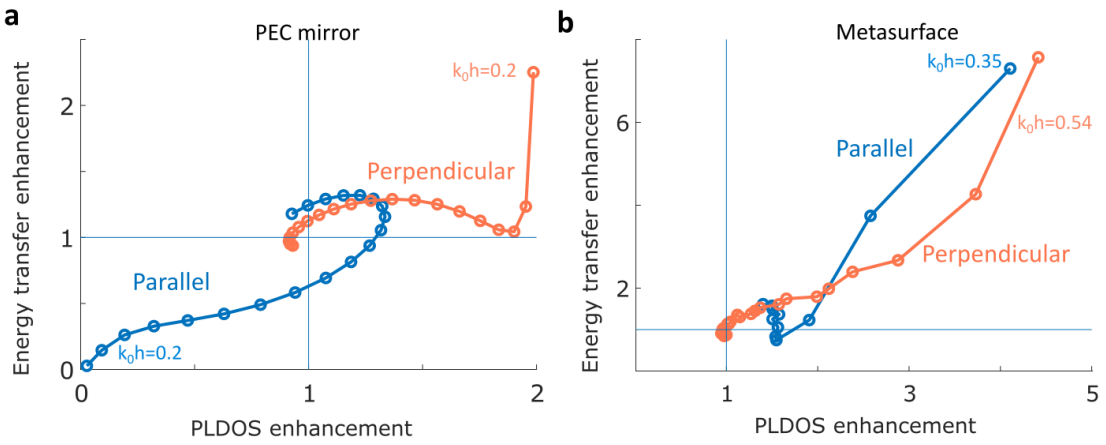

Figure 3 – Les diagrammes LDOS vs. Amélioration du transfert d'énergie pour le miroir PEC (a) et pour la métasurface (b). Les données correspondent aux résultats numériques de la Fig. 3.15(a) et (b) avec une distance dipôle-dipôle $R = \lambda/7$ et à la Fig. 3.14. Les marqueurs sont indiqués pour différentes hauteurs $k_0 h$ par rapport à la surface. Lorsque la distance h augmente, toutes les courbes convergent vers la valeur de l'espace libre (1,1).

Il a été démontré pour le domaine de champ proche (pour $k_0 R$ entre $\lambda/20$ et $\lambda/2$), qui est la région en optique la plus difficile à mesurer [16, 17]. De plus, comme cela a été montré dans le chapitre précédent, les antennes d'une longueur de $\lambda/7$ peuvent être considérées comme petites dans ce domaine de distance pour les mesures d'amélioration du transfert d'énergie. Ces résultats nous permettent de faire une analogie avec le taux de FERT et de montrer son comportement proche des SP des métaux dans la domaine optique.

Les cristaux photoniques sont des matériaux nanostructurés périodiques, similaires aux métasurfaces, qui présentent une bande interdite photonique et des régimes de d'auto-collimation. Les bandes interdites sont les gammes de fréquences où la propagation des ondes électromagnétiques est interdite. Dans le régime d'auto-collimation, l'onde se propage dans une direction sans divergence. Dans le domaine de fréquences térahertz (THz), les mesures en champ proche présentent des défis persistants différents de ceux de la région micro-ondes. Les effets en champ proche mentionnés du cristal photonique dans ce domaine de fréquences n'ont pas été étudiés expérimentalement.

Notre configuration innovante de génération/détection de champ proche en térahertz, avec des antennes à large bande situées sur des côtés opposés de l'échantillon, constitue une percée dans la réalisation de telles mesures. La vue schématique complète de l'installation expérimentale est présentée dans la figure 4(a) avec une photo de l'antenne émettrice et du détecteur près du PC, ainsi qu'une image détaillée de l'antenne (figures 4(b) et (c)). En utilisant cette méthode polyvalente, nous avons caractérisé les propriétés d'émission directionnelle d'un cristal photonique à base de silicium. Nos expériences révèlent une suppression du champ proche dans deux ban-

des interdites quasi-TE à 0,365 THz et 0,495 THz, ainsi qu'une émission directionnelle à 0,445 et 0,465 THz avec seulement des différences de 20 GHz.

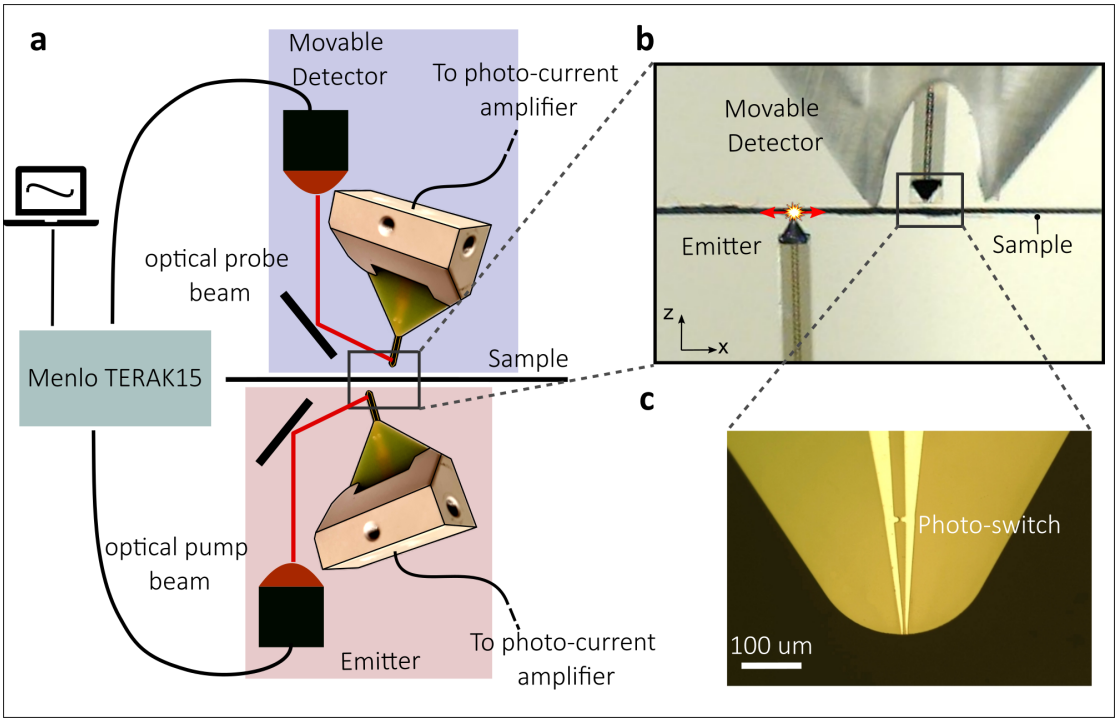

Figure 4 – Configuration expérimentale. (a) Représentation schématique de l'expérience; (b) Photographie de l'émetteur de dipôle térahertz orienté selon l'axe x (flèches rouges) fixé et du détecteur térahertz mobile placé de chaque côté du cristal photonique; (c) Image détaillée de l'embout d'antenne.

L'émission directionnelle observée est contrainte par la structure de bande complexe du cristal photonique. Il est à noter qu'une simple réorientation de l'axe du dipôle par rapport à la maille du cristal photonique a entraîné une redirection du signal. Nos résultats expérimentaux concordent bien avec les simulations, avec une erreur de prédiction de 3%. Cela souligne la nécessité de mesures complètes sur des échantillons réels, adressant des imperfections inaccessibles aux simulations seules. Ces résultats mettent en lumière le potentiel des cristaux photoniques en vrac comme une direction prometteuse pour les éléments de circuits 6G et soulignent la polyvalence des cristaux photoniques pour une émission maîtrisée sur des plateformes basées sur puce.

Dans le Chapitre 1, nous introduisons les fondements théoriques des phénomènes en champ proche des émetteurs quantiques. Ce chapitre présente le concept d'émission spontanée, le taux de FRET et les méthodes d'expérimentation micro-ondes de base, en établissant des analogies entre le taux de FRET dans les expériences optiques et les expériences micro-ondes. Les expériences d'antennes servent de pont entre ces domaines, fournissant une plate-forme pour étudier le transfert d'énergie à la fois aux

fréquences optiques et micro-ondes.

Dans le Chapitre 2, nous considérons un transfert d'énergie entre deux antennes dans l'espace libre et près d'un miroir conducteur électrique parfait (PEC). Nous obtenons un aperçu de l'interaction complexe entre la géométrie de l'antenne et l'efficacité de transfert d'énergie en comparant les résultats avec des dipoles ponctuels. Cependant, étant donné que nous utilisons ici des méthodes d'antenne micro-ondes pour compléter les expériences optiques, nous proposons une approche d'orientation moyenne. Cette méthode compare le taux de FRET de dipoles ponctuels orientés de manière aléatoire dans le domaine optique avec nos prédictions théoriques et nos mesures basées sur les antennes micro-ondes.

Le Chapitre 3 déplace le focus sur les métasurfaces. Nous montrons un exemple de mesures en champ proche micro-ondes près d'une métasurface hyperbolique pour détecter les effets de réflexion anormaux sur son bord. La métasurface hyperbolique est une métasurface avec une anisotropie extrême. Nous avons conçu une métasurface supportant des modes de surface, démontrant leur capacité à contrôler le transfert d'énergie et la LDOS.. Nous concevons une métasurface qui peut supporter la propagation de modes de surface pouvant imiter les ondes de plasmons de surface sur une interface métal-diélectrique dans le domaine optique. Par une combinaison de mesures expérimentales et de simulations numériques, nous montrons le rôle que jouent les modes de surface dans dans le transfert transfert d'énergie et de sa relation avec LDOS.

Dans le Chapitre 4, nous portons notre attention sur la gamme THz où nous considérons un cristal photonique avec une structure en nid d'abeille. Nous proposons une nouvelle technique expérimentale pour les mesures en champ proche avec une source de dipôle ponctuel qui nous permet de mesurer ces effets dans la gamme THz. Nous mesurons le champ proche du cristal photonique pour montrer la suppression de l'émission dans les bandes interdites et la redirection de l'émission due à sa structure de bande complexe.

En conclusion, nous discutons des perspectives futures de ce travail. Cette thèse explore les liens complexes entre les phénomènes en champ proche et les mécanismes de transfert d'énergie, explorant comment l'environnement photonique local peut être utilisé pour moduler les processus de transfert d'énergie.

Mots clés: Champ proche, Transfert d'énergie, Métasurface, Cristal photonique

Remerciements

First, I express my gratitude to my supervisors Stefan Enoch and Redha Abdeddaim for their unwavering support and invaluable guidance throughout my journey as academic advisors and mentors.

I am sincerely grateful to the distinguished jury members for dedicating their time and knowledge to evaluate my work.

1. Julien de Rosny, Institut Langevin
2. Matthieu Davy, University of Rennes
3. Stanislav Glybovski, ITMO University
4. Anne Sentenac, Aix Marseille Université
5. Frédérique Gadot, Université Paris Nanterre

I am also grateful for the productive collaboration with Jérôme Wenger, Martijn de Sterke, Alessandro Tuniz, Boris Kuhlmey, and Kaizad Rustomji, whose constant support and insightful guidance contributed significantly to the development of my research during my PhD.

Special thanks go to Muliwave Technologies and Tryfon Antonakakis for their generous support, which has allowed me to continue my research efforts and opened the door to future projects.

Contents

Affidavit 2

Liste de publications et participation aux conférences 3

Résumé 4

Abstract 5

Résumé 6

Remerciements 14

Contents 15

List of Figures 18

List of Tables 26

Introduction 27

1 Introduction near-field energy-transfer 30
- 1.1 Spontaneous Emission and Densities of States . . . 31
  - 1.1.1 Quantum Emitter . . . 31
  - 1.1.2 Spontaneous emission . . . 31
  - 1.1.3 Densities of States . . . 32
- 1.2 Förster Resonance Energy Transfer . . . 33
  - 1.2.1 FRET rate . . . 33
  - 1.2.2 Relationship of FRET and LDOS . . . 35
  - 1.2.3 Applications of FRET . . . 35
  - 1.2.4 Challenges of FRET measurements in the optical range . . . 36
- 1.3 Classical analogy to FRET rate enhancement . . . 37
  - 1.3.1 Classical antenna in the microwave range . . . 37
  - 1.3.2 Near-field of the antenna . . . 37
  - 1.3.3 Basics of the microwave experiments . . . 38
  - 1.3.4 Link between optical emitter and classical antenna for FRET and LDOS analogy . . . 40
- 1.4 Outline . . . 43

2 Energy transfer near a PEC mirror for finite-size antennas 45
- 2.1 FRET rate enhancement near a PEC mirror . . . 46

2.2 Analytical model for energy transfer for finite-size antennas in the microwave range . . . 47
2.2.1 Finite sized-dipole antenna . . . 47
2.2.2 Reference case in free space . . . 48
2.2.3 Comparison of the real-sized dipoles and point dipoles in free space . . . 51
2.2.4 Energy transfer for two finite-sized antennas near the PEC mirror 53
2.2.5 Comparison of the real-sized dipoles and point dipoles near the PEC mirror . . . 56
2.3 Measurements of the energy transfer near the PEC mirror at the Microwave range . . . 60
2.4 Energy transfer averaged over the dipoles orientations, comparison with FRET rate enhancement in optics . . . 62
2.5 Measurements of the LDOS near the PEC mirror . . . 64
2.6 Outline . . . 66

3 Near-field control with metasurface in the microwave range 67
3.1 Introduction to Metasurface . . . 68
3.1.1 Definition and versatility of Metasurfaces . . . 68
3.1.2 Dispersion and isofrequency contours . . . 70
3.1.3 Types of anisotropy and Hyperbolic Metasurface . . . 70
3.1.4 Complementary and Self-Complementary Metasurface . . . 72
3.1.5 Anomalous Reflection From Hyperbolic Media . . . 73
3.1.6 Near-field scanning in the Microwave range . . . 76
3.2 Energy-transfer enhanced by surface waves . . . 78
3.2.1 Introduction Surface Plasmons . . . 78
3.2.2 Design of the metasurface that supports surface modes . . . 79
3.2.3 Influence of the dipole's position respective to the metasurface unit cell . . . 81
3.2.4 Surface mode of the metasurface . . . 82
3.3 Energy transfer enhancement and LDOS of the dipole antennas near the metasurface . . . 83
3.3.1 Measurements methods . . . 83
3.3.2 LDOS near the metasurface . . . 85
3.3.3 Energy transfer near the metasurface . . . 86
3.3.4 Correlation of the energy transfer enhancement with the LDOS 88
3.4 Outline . . . 90

4 Methods of the near-field measurements in the THz range 92
4.1 Experimental methods in the terahertz range . . . 93
4.1.1 Introduction to terahertz range . . . 93
4.1.2 Photonic crystals . . . 94
4.1.3 Setup for THz measurements . . . 96

4.2 Broadband terahertz near-field excitation and detection of silicon PC modes . . . 99
4.2.1 Emission Suppression at the TE Bandgap . . . 99
4.2.2 Directed emission and field concentration . . . 101
4.2.3 Impact of the emitter position on the emission . . . 104
4.3 Outline . . . 108

Conclusion and Perspective **110**

Bibliography **114**

List of Figures

1 (a) Diagramme des niveaux d'énergie représentant l'émission spontanée. γ_{rad} désigne le taux de transfert d'énergie radiative vers n'importe quel endroit dans l'environnement. (b) Diagramme des niveaux d'énergie montrant le FRET. Le FRET se produit lorsque deux atomes ou molécules voisins, désignés comme donneur et accepteur, ont des spectres d'émission et d'absorption qui se chevauchent et se couplent en raison d'une interaction dipôle-dipôle coulombienne. Le taux de FRET Γ_{DA} désigne le transfert d'énergie vers l'emplacement de l'accepteur uniquement.(Source: [5]) 7

2 Les améliorations du PLDOS et du taux de FRET près d'un miroir PEC sont calculées avec le formalisme de la fonction de Green pour les orientations (a) perpendiculaires, (b) parallèles et (c) alignées. R est la distance dipôle-dipôle, k_0 est le nombre d'onde et h est la hauteur du dipôle par rapport au miroir. Les boîtes rouges représentent les domaines relatives étudiées dans les travaux précédents en optique. . . . 8

3 Les diagrammes LDOS vs. Amélioration du transfert d'énergie pour le miroir PEC (a) et pour la métasurface (b). Les données correspondent aux résultats numériques de la Fig. 3.15(a) et (b) avec une distance dipôle-dipôle $R = \lambda/7$ et à la Fig. 3.14. Les marqueurs sont indiqués pour différentes hauteurs $k_0 h$ par rapport à la surface. Lorsque la distance h augmente, toutes les courbes convergent vers la valeur de l'espace libre (1,1). 11

4 Configuration expérimentale. (a) Représentation schématique de l'expérience; (b) Photographie de l'émetteur de dipôle térahertz orienté selon l'axe x (flèches rouges) fixé et du détecteur térahertz mobile placé de chaque côté du cristal photonique; (c) Image détaillée de l'embout d'antenne. 12

1.1 Near-field interactions of quantum emitters (a) Energy-level diagram of the spontaneous emission. γ_{rad} is the rate of spontaneous emission. (b) Energy-level of FRET and overlapping emission and absorption spectra of a donor and acceptor. The FRET rate Γ_{DA} is the rate of the energy transfer from donor position to the acceptor position. (Source: [5]) . . 32

1.2 Schematic observations of the antenna field at different distances using the example of a dipole antenna. (a) Near field, where the phase difference of the field radiated by each part of the antenna cannot be neglected. (b) far field, where this difference is negligible. (Source: [22]) 38

1.3 Schematic illustration of (a) one-port and (b) two-port network 39

1.4 Experiment to measure the Purcell factor in a microwave range. (a) Geometry of an electric dipole antenna and a magnetic dipole antenna near a perfect metallic mirror. Measured results for the Purcell factor along with the analytical results for (b) a parallel and (c) perpendicular orientations of the electric dipole antenna with respect to the mirror. (Source: [67]) 41
1.5 Description of dipole-dipole energy transfer at (a) optical range from a quantum-mechanical point and from a (b) microwave point using a two-port network. (c) Photograph of two dipole antennas for microwave measurements. (d) Calibration of the dipole-dipole energy transfer power versus the dipole-dipole separation R in free space. Markers are experimental data for parallel dipoles (red) and aligned dipoles (blue) and dashed lines are theoretical predictions from Green's function theory (Source: [6]) 42

2.1 PLDOS and FRET rate enhancements near a PEC mirror calculated with Green function formalism for (a) perpendicular, (b) parallel, and (c) aligned orientations. R is the dipole-dipole distance, k_0 is the wave number, and h is the dipole's height to the mirror. Red boxes denote the relative ranges studied in the previous works in optics [7, 8]. 47
2.2 Schematic view for the considered cases. (a) reference parallel case and (b) reference aligned case; Two dipole antennas with PEC mirror (c) perpendicular and (d) parallel orientation corresponded to the reference parallel case, (d) aligned case. Antennas 1 and 2 are the donor and the acceptor, respectively, 1' is an image antenna, which appeared due to the presence of a PEC mirror. 49
2.3 Mutual impedance, normalized by the maximum, for the (a) parallel case $\left|Z^0_{21_{parl}}\right|^2$ and (b) aligned case $\left|Z^0_{21_{align}}\right|^2$ of the two finite antennas in the free space. The gray lines follow the slope $1/R^6$ for comparison. The dashed black line is the Fret rate calculated for an ideal point dipole. Colorful triangles correspond to the FDTD simulations. 52
2.4 Energy transfer in free space for parallel dipoles in the region $0.12 < k_0R < 0.57$. (a) Bicolor map showing the regions of antenna length L and antenna separations k_0R where the exponent of the energy transfer distance dependence deviates by more or less than 5% respective to the predicted $1/R^6$ dependence. (b) Distance dependence of the averaged exponent $1/R^n$ of energy transfer as a function of the dipole length L. . 53

2.5 Comparison of the energy transfer between two finite antennas with antenna length L (solid curves) and FRET rate enhancement for point-dipoles (dashed, black line) near a PEC mirror. The effects of finite-size are shown for parallel ((a), (c), and (e)), and perpendicular ((b), (d), and (f)) orientations for different antenna separation $k_0R = 0.2$ (a) and (b), $k_0R = 0.6$ (c) and (d), $k_0R = 1$ (e) and (f). On the right, color maps with percentage errors between the point dipole and finite-sized antennas are shown. The prohibited regimes of dipole positions for the perpendicular case are shown as gray areas in the colormaps. White lines highlight the dipole lengths shown in the graphs on the left. 57
2.6 Comparison of the energy transfer between two finite antennas with antenna length L (solid curves) and FRET rate enhancement for point-dipoles (dashed, black line) near a PEC mirror for aligned orientation. The effects of finite size are shown for different antenna separations $k_0R = 0.2$ (a), $k_0R = 0.6$ (b), $k_0R = 1$ (c). On the right, colormaps with percentage errors between the point-dipole and finite-sized antennas are shown. White lines highlight the dipole lengths shown in the graphs on the left. 58
2.7 A real part of the input impedance of dipole antenna as a function of its length L 60
2.8 Experimental setup for measuring energy transfer in the microwave range: (a) photo of the dipole antennas; (b) schematic view of the setup 61
2.9 Modification of energy transfer enhancement due to a PEC mirror for (a), (b), (c) perpendicular, (d), (e), (f) parallel, and (g), (h), (i) aligned configuration. The microwave measurements (Blue triangles) at 1 GHz (top row), 3 GHz (middle row), and 5 GHz (bottom row) were compared with analytical theory for finite antennas (purple) and FRET rate enhancement for point-dipoles (dashed, black). The length of the antennas is $L = 10$ mm and their separation is $R = 10$ mm. The root mean square error between experimental results and theory for the point-dipoles is shown in each case. 62
2.10 Averaging of energy transfer over orientation: (a) Schematic of all orientations for obtaining orientation averaged energy transfer. The averaged energy transfer enhancement as a function of antenna-mirror distance k_0h at (b) 0.5 GHz, (c) 1 GHz (d), 3 GHz, and (e) 5 GHz at fixed antenna to antenna distance $R = 10$ mm and antenna lengths $L = 10$ mm. Experiments (blue triangle) compared with point-dipole-based calculations for orientation averaged FRET rate enhancement (black dashed line). . 64
2.11 LDOS and PLDOS of dipole antenna placed near the PEC mirror, experimental and analytical results for (a) parallel, (b) perpendicular polarisation and averaged polarization 65

3.1 Examples of the metasurface functionalities: a — bandpass frequency selective surface; b — bandstop frequency selective surface; c — high impedance surface; d — narrowband perfect absorber; e — twist polarizer; f — right-handed circular-polarization frequency selective surface; g — linear-to-circular polarization converter; h — two-dimensional leaky-wave antenna with a conical-beam pattern; i — focusing transmit array; j — focusing reflectarray; k — flat Luneburg lens; l — hologram (Source: [74]) 68
3.2 Examples of metasurface IFCs. The color map is the vertically polarized electric field E_z excited by a dipole oriented z placed above the metasurface. The curves in the graphs are IFCs of each metasurface. a) Isotropic metasurface, $\sigma_{xx} = \sigma_{yy} = 1.5 + i20\ \mu S$. b) Hyperbolic metasurface, $\sigma_{xx} = 1.5–i20\ \mu S$, $\sigma_{yy} = 1.5 + i20\ \mu S$. c) Hyperbolic metasurface, $\sigma_{xx} = 1.5 + i20\ \mu S$, $\sigma_{yy} = 1.5–i20\ \mu S$. d) σ-near-zero metasurface, $\sigma_{xx} = 1.5 + i20\ \mu S$, $\sigma_{yy} = 1.5\ \mu S$ (Source: [92]). 72
3.3 Schematic geometry of a self-complementary metasurface constructed as an array of inductive and capacitive parallel strips. The polarization of TE and TM surface-wave modes with a parallel and orthogonal propagation direction is shown on top of the metasurface (Source: [91]). 73
3.4 IFCs and refraction at the interface between two media. (a) Example of the solution of a refraction problem using IFCs for two isotropic media. (b) The illustration of the no-reflection paradox, when there is no point on the hyperbolic IFC, corresponding to the reflected wave. Here is also shown that when the wavevector in the first medium is larger than the wavevector in the second medium, the transmitted wave is absent as well. In both figures (a) and (b) it is assumed that electromagnetic wave is incident from the first medium. (c), (d) - Schematic representation of IFCs for a lossless and a lossy hyperbolic medium. In the lossless case, there are two quadrants in the phase plane, in which IFC is absent, while, in the lossy case, IFC is present in all quadrants (Source: [2]). . . 74
3.5 Isofrequency contours for lossy hyperbolic media with $\varepsilon = 1$, $Re[k_z] \equiv k_z'$, $Im\ [k_z] \equiv k_z''$ and $\tilde{k}_{x,z} = k_{x,z}/k_0$ for different values of loss parameter κ, $\kappa = \varepsilon, \kappa = 0.1\varepsilon, \kappa = 0.01\varepsilon$. Colorbar encodes the modulus of the imaginary part of $\tilde{k}_z$. Panels A, B, and C show that as $\kappa \to 0$, precisely in those quadrants in which the branches of the dispersion equation are absent for the lossless hyperbolic media, the imaginary part of k_z is going to infinity, $Im(k_z) \to \pm\infty$. Panel D shows a schematical representation of the IFC for ordinary and ghost modes in lossless and lossy hyperbolic medium. 75
3.6 Self-complementary hyperbolic metasurface. (a) unit cell of the metasurface. (b) photo of the excitation loop over a metasurface. (c) square and rhombic samples respectively. The insets show the orientation of the unit cell. 76

3.7 Numerical simulation and experimental results. (a) and (b) numerical and experimental results for rhombic and square samples, respectively. modulus and real parts of H_y, respectively. Dashed rectangles represent the edge of the sample. (c) - two-dimensional Fourier transform of the experimentally measured normal component of the magnetic field, for the square and rhombic samples, respectively, showing the hyperbolic dispersion of the metasurface. Brown lines correspond to the numerically calculated IFCs using the Eigenfrequency Solver of CST Microwave Studio. 78
3.8 SPs at the interface between a metal and a dielectric material (a) A transverse magnetic field in the y direction, and an electric field E normal to the metallic surface. The field component perpendicular to the surface is enhanced near the surface and decays exponentially with distance away from it (b). The field in this perpendicular direction is evanescent, reflecting the bound, non-radiative nature of SPs, and it prevents power from propagating away from the surface. In the dielectric medium above the metal the decay length of the field, δ_d is of the order of half the wavelength, whereas the decay length into the metal, δ_m is determined by the skin depth. (c) the dispersion relation of the SP (k_{SP}) (Source: [72]) 79
3.9 Metasurface supporting surface waves in the microwave regime. (a) Illustration of the unit cell (a=8 mm, h=1.9 mm, $w_1 = 7$ mm, $w_2 = 5$ mm, and $w_3 = 0.5$ mm). (b) Photograph of the metasurface. (c) Dispersion curve of the first propagating surface mode of the metasurface (blue curve). The shaded region indicates the deviation range due to ±4% variations in the unit cell dimensions. The orange curve is the dispersion of the silver in the optical range. Both dispersion curves are normalized by their plasmon frequency (F_p) 80
3.10 The effective permittivity ε_{eff} of the metasurface in the microwave range for the normal incidence and the permittivity of the silver ε_m in the optical range 81
3.11 Electric field distribution (E_y and E_z components) of the surface wave eigenmode of the metasurface at 4 GHz on top of the unit cell: for the height from the surface $h = 1$ mm and the height $h = 5$ mm. 82
3.12 Simulated and measured magnetic field maps and simulated electric field maps of a parallel and perpendicular dipole in the presence of a metasurface and PEC mirror, showing that surface waves are excited near the metasurface. The source dipole is located at a distance of 5 mm ($\lambda/14$) from the surface. 83
3.13 Experimental setup for measuring energy transfer in the microwave range: (a) schematic view of the setup for energy transfer enhancement vs h measurements ; (b) schematic view of the setup for energy transfer enhancement vs R measurements ; (c) photo of the dipole antenna near the metasurface 84

3.14 The influence of surface-wave excitation on the LDOS detected by the dipole antenna. LDOS as a function of the height h between the plane of the dipole's center and the boundary plane for parallel (a) and perpendicular (b) dipoles orientation. 85
3.15 The influence of surface-wave excitation on the near-field interaction processes between two dipoles. (a,b) energy transfer enhancement as a function of height h between the dipole antennas and the surface. The dipole-dipole distance is set at $k_0R = 0.9$, corresponding to $R = \lambda/7$. (c, d) energy transfer enhancement as a function of the distance R between the two dipoles. For (d), the height is set at $k_0h = 0.47$, while for (c) due to the finite size of the dipoles, we switch to $k_0h = 0.45$. In (a, c), both dipoles have parallel orientation to the surface and perpendicular orientation in (b, d). In all graphs, markers correspond to experimental data, while lines are numerical calculations. 87
3.16 A comparison of the gains in energy transfer and LDOS found with the metasurface to the PEC shows the spatial distribution of the surface wave impact. The dipole-dipole distance for the energy transfer enhancement corresponds to $k_0R = 0.9$ as for the results above. 89
3.17 The LDOS vs. Energy transfer enhancement diagrams for the PEC mirror (a) and for the metasurface (b). The data corresponds to the numerical results of Fig. 3.15 (a) and (b) with a dipole-dipole distance $R = \lambda/7$ and Fig. 3.14. The markers are shown for different heights k_0h to the surface. When the distance h increases, all the curves converge towards the free space (1,1) value 89

4.1 Convex (red), concave (blue) and flat (black) iso-frequency contours. Iso-frequency contours on the left (right) panel correspond to the second band of a two-dimensional square (triangular) lattice PC made of dielectric rods in free space. The wave vectors resulting in the Bloch eigenwaves with the group velocity pointing to the direction normal to the Brillouin zone boundary are depicted with arrows (Source: [146]) . 95
4.2 Silicon PC with hexagonal periodic lattice. (a) The emission of the x-polarized point dipole near the surface of a PC and the emitter is placed at the center of the sample. The direction of the emission is highly dependent on the frequency: f_1 corresponds to the suppression of the emission and redirection of the emission at frequencies f_2 and f_3 which are shown with white dashed lines (b) PC micrograph. Black: silicon; white: air; period: $a = 240$ μm; hole radius: $r = 72$ μm. The unit cell is highlighted in white, the emitter dipole direction is shown by red arrows. (d) Calculated PC band structure. Grey-shaded regions highlight the first and second quasi-TE band gaps, respectively, and the dashed black lines highlight the first and second frequencies of the directional emission in (a). The first Brillouin zone is shown in the inset. 96

4.3 Experimental setup. (a) Schematic representation of the experiment; (b) Photograph of the fixed x-oriented terahertz dipole emitter (red arrows) and moveable terahertz detector placed on either side of the PC; (c) Detailed image of the antenna tip. 98
4.4 Signal, detected by the detector placed near the emitter in the free space with the presence of only emitter. (a) temporal response when the detector is placed right on top of the emitter; (b) associated signal in the frequency domain, obtained by using Fast Fourier Transforms; (b) 2D Measurements of the near electric field $|E_x^0|$ and its imaginary part imag(E_x^0) at 0.365 THz; (c) An electric field $|E_x^0|$ and it's imaginary part imag(E_x^0) at 0.495 THz; These free-space measurements are used as a reference case in the following experiments 99
4.5 Dipole emission suppression within the two band gaps. (a) Measured x-component of the electric field magnitude $|E_x|$ near the surface of the PC for an x-polarized emitter, at 0.365 THz (left) and the ratio $|E_x|/|E_x^0|$ (right), revealing suppression of dipole emission. (b) Corresponding FDTD numerical simulations. (c) and (d) respectively show the corresponding experiment and simulation at 0.495 THz within the second band gap. All window sizes are 8 mm × 8 mm. 100
4.6 Directed emission of the x-polarized dipole. The PC and dipole are oriented as in Fig. 4.3 (b). (a) The measured x component of the electric field magnitude $|E_x|$ for a x polarized emitter at 0.445 THz. (b) the ratio with the reference case of the free-space $|E_x|/|E_x^0|$. (b) Shows the corresponding FDTD numerical simulations. (c) Corresponding IFC for quasi-TE (red) and quasi-TM (blue) modes. The black arrow corresponds to dipole orientation, which preferentially excites the quasi-TE Bloch modes that are close to the light line and propagated perpendicular to it (purple arrows). (d) Show the corresponding experiment at 0.465 THz and simulation (e) at 0.45 THz, and (f) IFC. The Bloch modes close to the light line are excited by the dipole that lies on the diagonal axes, as observed in both experiment and simulation. The window sizes for all field maps are 8 mm × 8 mm. All the field maps are normalized by the maximum of $|E_x|$. 102
4.7 Two-dimensional Fourier transform of the experimentally measured and simulated electric field E_x (a) Measurements of the transmitted electric field $Im(E_x)$ of a x polarized electric dipole (left), the associated amplitude of the 2D Fourier transform of the complex field (right) at 0.445 THz and in a dB scale, superimposed with simulated TE IFCs. Its regions of maximum intensity overlap with parts of the IFCs that are close to the light line. (b) The corresponding numerical simulations at 0.43 THz. Dipole excitation and field detection are at 200 μm from the edge of the membrane. The x-polarized dipole in b) excites only a subset of the quasi-TE modes shown in d). The data set in (a) and (b) is the same as in Figure 4.2. 104

4.8 Redirection of the emission by rotating the PC keeping the dipole at the same position, as highlighted by the schematics of the unit cell in the corner of the field-maps. (a) Measured x-component of the electric field magnitude for an x-polarized emitter placed on the opposite side and at 0.445 THz. (b) Corresponding numerical simulations at 0.43 THz. (c) and (f) show the corresponding IFC. (d) and (e) are the experiment and simulation at 0.465 THz, and 0.45 THz. Black arrows in (c) and (f) indicate dipole orientation on the surface. 105
4.9 FDTD simulations show the effect of increasing detector distance. (a) We consider the same emitter configuration as in previous simulations at 0.45 THz, keeping the distance $h_e = 200\,\mu$m between the emitter and the PC constant, but we vary the distance h_d between the detector and the PC. (b) The field magnitude $|E_x|$ is shown for $h_d = 0\,\mu$m, $h_d = 100\,\mu$m, $h_d = 200\,\mu$m $h_d = 300\,\mu$m, and $h_d = 400\,\mu$m. All amplitudes are normalized to the maximum of the $h_d = 0\,\mu$m. (c) The ratio of the electric field $|E_x|$ to the reference case of the free space. Note that the overall emission pattern is nominally unchanged, but the field amplitude goes down as the detector distance increases. (d) Two-dimensional Fourier transform of the simulated electric field. 107
4.10 Simulations when a z-polarized (a) electric- and (b) magnetic- dipole is placed at the center of the PC. In this case, the high-k quasi-TM and quasi-TE Bloch modes can be excited independently. In contrast, the x-polarized dipole in b) excites only a subset of the quasi-TE modes shown in d). The schematics on top, show the reference frame and simulation configurations. The dark blue region represents the PC. 108
4.11 Distance dependence of FRET efficiency for the parallel, aligned, and averaged orientated dipoles in the vacuum. R is the dipole-dipole distance, k_0 is the wave number for the vacuum 111
4.12 Numerical simulations of the Energy transfer efficiency compared for real-sized antennas (linear scale): a) parallel case; b) aligned 112

List of Tables

2.1 Distances r_0, r_1, and r_2 are used in calculations of the mutual impedance from Eq 2.5 in the parallel ($Z^0_{21_{\text{parl}}}$) and aligned ($Z^0_{21_{\text{align}}}$) orientations in free space. 50

2.2 Distances r'_0, r'_1, and r'_2 used in the calculation of mutual impedance between image antenna $1'$ and antenna 2, used for calculating the mutual impedance in the perpendicular ($Z'_{21_{perp}}$), parallel ($Z'_{21_{parl}}$), and aligned ($Z'_{21_{align}}$) configurations. A schematic can be seen in Figure 1 (a), (b), (c). 55

Introduction

This thesis is about near-field interactions and near-field control in microwave and Terahertz (THz) frequency ranges. In recent years, the study and manipulation of energy transfer processes at the nanoscale have become a promising direction in photonics and nanotechnology. In the optical range, quantum emitters, such as atoms, molecules, quantum dots, or nanoscale structures, are integral components of various applications including quantum information processing, communications, and sensing. Quantum emitters serve as fundamental objects capable of emitting single photons. Their energy is quantized, and the emission occurs as a result of quantum mechanical processes. This process is called spontaneous emission when an excited emitter spontaneously emits a photon and transitions to a lower energy state. The rate of spontaneous emission, which is influenced by the emitter's environment, is quantified by a Purcell factor. The Purcell factor measures the increase or decrease in the emission rate compared to the free space. Understanding the interaction between emitters and the environment, characterized by the local density of states (LDOS), is critical to controlling spontaneous emission.

A Förster resonance energy transfer (FRET) is a near-field energy transfer process between two quantum emitters. It occurs when two emitters, namely donor and acceptor, are placed in proximity of each other and the energy is transferred directly without being propagated into the environment. FRET has applications in various fields, including solar energy harvesting, optoelectronics, and biophysics. The FRET highly depends on factors such as donor-acceptor distance, spectral properties of the emitters, and LDOS, making it very sensitive to the emitter environment. Understanding and controlling FRET and spontaneous emission is important for various applications, from optoelectronics to biophysics.

Despite significant interest in optical FRET measurements, some challenges remain in this field, including weak signals, limited spatial resolution, limitations on donor-acceptor spacing, and challenges in controlling the emitter's orientation. These limitations permit us to fully understand the influence of the nanophotonic environment on the FRET. To address these issues, an analogy between the FRET rate in the optical range and antenna measurements in the microwave range was shown in previous work[6]. This analogy draws parallels between quantum emitters in optics and classical dipole antennas in microwaves and opens up new experimental approaches. By using microwave techniques, we can overcome the limitations of optical FRET measurements, providing improved signal strength, spatial resolution, and precise control over antenna positioning. The antennas used in such experiments were highly sub-wavelength, however, they still have a finite size. Unlike optics, where the quantum emitters are assumed to be point dipoles, microwave antennas cannot

be as electrically small as atoms/molecules, and therefore their finite size can affect the measurement of energy transfer, particularly at short distances. Here we incorporate the effect of antenna size on the microwave antenna-based analogy of the FRET measurements. We theoretically and experimentally characterize energy transfer enhancement near a perfect electrical conductor (PEC) mirror using microwave antennas. In addition, we demonstrate individual contributions of the different antenna orientations. Finally, we propose a scheme of orientational averaging for antenna energy transfer measurements, as a way to compare typical optical FRET measurements done with an ensemble of emitters with randomly oriented dipole moments to microwave antenna-based measurements where dipole orientations are precisely defined.

Moreover, unlike metals in the microwave range, which behave like PEC mirrors, in the optical range, metals support surface waves known as surface plasmons (SPs). The effect of SP on FRET rate and LDOS remains unclear in optics. This effect can be studied in the microwave range by applying a specially designed metasurface. Metasurfaces are artificial structures that represent a periodic array of unit cells or sub-wavelength metaatoms. Metasurfaces can be designed to manipulate the phase, amplitude, and polarization of incident electromagnetic excitation at sub-wavelength scales. They can be designed to support surface waves, similar to SPs on metal surfaces in the optical range. We designed such a metasurface and showed the improvement in energy transfer and LDOS of the two dipole antennas in the presence of surface modes. We show that the relationship between energy transfer and LDOS became linear, unlike in the case of the PEC mirror.

The near field of the emitter can be significantly manipulated by metasurfaces and photonic crystals (PCs). Metasurfases can be isotropic, anisotropic, and highly anisotropic. The electromagnetic properties of an isotropic metasurface do not depend on the direction of wave propagation. In other words, the electromagnetic wave propagates in all directions with the same properties. On the other hand, the electromagnetic properties of an anisotropic metasurface depend on the direction of propagation. The extreme cases of anisotropy are called highly anisotropic metasurfaces. An example of such a metasurface is a hyperbolic metasurface, which can exhibit unique properties. Using microwave measurement methods, we show an anomalous reflection paradox at the edge of the hyperbolic metasurface.

PCs are periodic nanostructured materials, similar to metasurfaces, that exhibit photonic band gaps and self-colimation regimes. The band gaps are the frequency ranges where the propagation of electromagnetic waves in the PCs is forbidden. In the self-colimation regime, the wave propagates in one direction without scattering. In the THz frequency range, near-field measurements present ongoing challenges that are different from those in the microwave region. We present an experimental setup for near-field measurements at THz that allows us to study the mentioned near-field effects of photonic crystals that have not been studied experimentally.

In Chapter 1, we introduce the theoretical foundations of the near-field phenomena of quantum emitters. This chapter introduces the concept of spontaneous emission, the FRET rate, and basic microwave experiment methods, drawing analogies between

the FRET rate in optical experiments and microwave experiments. Antenna experiments serve as a bridge between these fields, providing a platform to study the energy transfer at both optical and microwave frequencies.

In Chapter 2 we consider an energy transfer between two antennas in free-space and near the PEC mirror. We improve our understanding of the complex interaction between antenna geometry and energy-transfer by comparing the results with point dipoles. However, considering that we use microwave antenna methods here to complement optical experiments, we propose an orientational averaging approach. This method compares the FRET rate of randomly oriented point dipoles in the optical domain with our theoretical predictions and measurements based on microwave antennas.

The Chapter 3 shifts the focus to metasurfaces. We show an example of microwave near-field measurements near a hyperbolic metasurface to detect anomalous reflection effects on its edge. The hyperbolic metasurface is a metasurface with extreme anisotropy. In the second part of the chapter, we design a metasurface that can support the propagation of surface modes that can mimic surface plasmon waves on metal-dielectric interference in the optical range. We demonstrate their ability to control energy transfer and LDOS of dipole antennas. Through a combination of experimental measurements and numerical simulations, we show the role that surface modes play in shaping energy transfer and its relationship with LDOS.

In Chapter 4, we turn our attention to the THz range where we consider a photonic crystal with a hexagonal lattice. We suggest a novel experimental technique for near-field measurements with a point dipole source that allows us to measure these effects at the THz range. We measure the near-field of the photonic crystal to show the emission suppression in the band gaps and redirection of the emission due to its complex band structure.

In conclusion, we discuss the prospects of this work. This thesis delves into the complex connections between near-field phenomena and energy-transfer mechanisms, exploring how the local photonic environment can be used to modulate energy-transfer processes. Our findings provide new insights into the fundamental physics of energy transfer and FRET and reveal new opportunities for exploring these phenomena in a wider range of conditions.

1 Introduction near-field energy-transfer

This chapter introduces the theoretical foundations of the near-field phenomena of quantum emitters, the concept of spontaneous emission, the FRET rate, and basic microwave experiment methods, drawing analogies between the FRET rate in optical experiments and microwave experiments. FRET measurements in optics have received a lot of attention in recent years, but some challenges remain unresolved, including weak signals, limited spatial resolution, limitations in emitters spacing, and challenges in controlling the orientation of the emitters. These limitations permit us to fully understand the influence of the nanophotonic environment on the FRET. An analogy between the FRET rate in the optical region and antenna measurements in the microwave region was shown in previous work[6] to address these issues. The parallel between quantum emitters in optics and classical antennas in microwaves serves as a bridge between these fields, providing a platform for studying energy transfer at both optical and microwave frequencies. In the following chapters, we present original experimental and theoretical studies that aim to expand our understanding of the role of near-field control in energy-transfer processes.

1.1 Spontaneous Emission and Densities of States

1.1.1 Quantum Emitter

A quantum emitter is a physical system capable of emitting individual photons due to quantum mechanical processes. These emitters can be atoms, molecules, quantum dots, or other nanoscale structures [15]. Quantum emitters are important components in applications such as quantum information processing, quantum communication, and quantum sensing [18]. Examples of quantum emitters include individual atoms or ions, semiconductor quantum dots, color centers in diamonds, and organic molecules. These systems have distinct advantages and limitations depending on their stability, coherence properties, and ease of manipulation, making them suitable for various applications in quantum technologies. They can be manipulated and controlled at the single-photon level, allowing experiments to be carried out and technologies to be developed that take advantage of the unique properties of quantum mechanics.

In quantum mechanics, energy is quantized, meaning it comes in discrete packets of energy. When a quantum emitter experiences a transition between energy levels, it emits or absorbs photons with an energy corresponding to the energy difference between those levels, and individual photons are emitted one at a time rather than continuously. The emitter size is usually smaller than the field variation scale ($\lambda/100$). It allows us to consider only a dipole moment and consider an atom as an oscillating dipole. Such a dipole approximation is the most common type of spontaneous emission source.

1.1.2 Spontaneous emission

The spontaneous emission process is where a quantum emitter in its excited state spontaneously emits a photon in the environment and is transitioned to a ground energy state. The spontaneous emission process is shown in Figure 1.1 (a). The rate at which the emitter decays to the ground state γ is a pure quantum effect and requires a description of quantum electrodynamics (QED). The spontaneous decay rate is given by

$$\gamma_{rad} = \frac{1}{\tau} = \frac{\pi\,\omega}{\hbar\,\varepsilon_0} \left|\boldsymbol{\mu}\right|^2 PLDOS \tag{1.1}$$

where ω is the frequency of the transition, ε_0 is the permittivity of the free space, $\hbar$ is the Planck constant, τ is the lifetime of the emitter, and $\boldsymbol{\mu} = \mu\boldsymbol{n}$ is the transition dipole moment. According to QED, the spontaneous emission rate is related to the transition probability. This connection between the transition probability per unit of time from the initial state to the final state and the spontaneous emission rate can be expressed by Fermi's golden rule [15]. The partial local density of states (PLDOS) is the factor determined by the environment and directly affects the emission; it will be discussed in the next section.

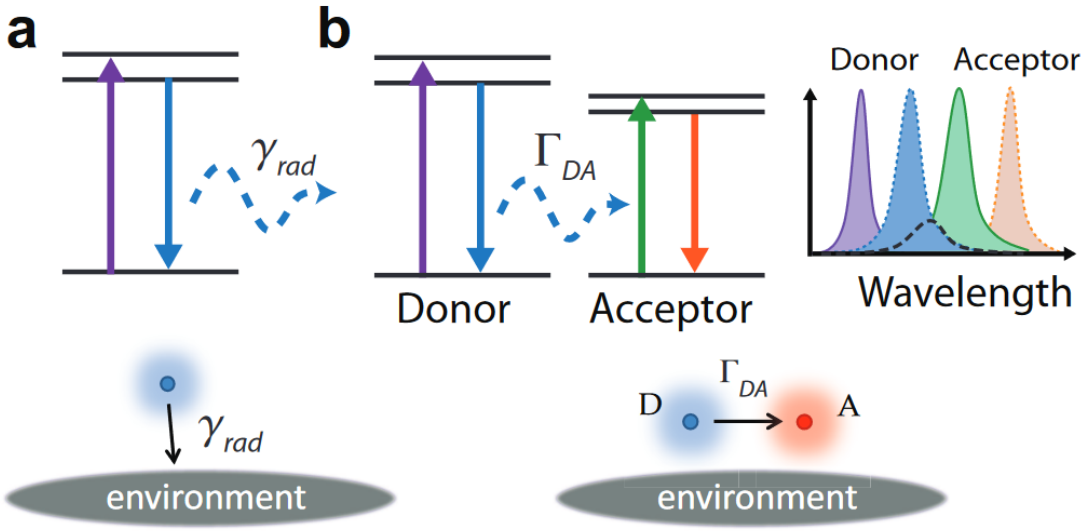

Figure 1.1 – Near-field interactions of quantum emitters (a) Energy-level diagram of the spontaneous emission. γ_{rad} is the rate of spontaneous emission. (b) Energy-level of FRET and overlapping emission and absorption spectra of a donor and acceptor. The FRET rate Γ_{DA} is the rate of the energy transfer from donor position to the acceptor position. (Source: [5])

1.1.3 Densities of States

The spontaneous emission is not an inherent property of the emitter. It is now understood that spontaneous emission is modified by the environment in which the emitter is located. Purcell's research [19] showed that the spontaneous decay rate of a magnetic dipole placed in a resonant electronic device was higher than the decay rate in a free space. This demonstrated that the environment of the atom can alter its radiative characteristics. The density of optical states was introduced to characterize this effect of the environment on spontaneous emission and measure the availability of electromagnetic modes to decay into the environment. [20].

There are many ways of describing the densities of states in the literature. The most common definitions are the density of optical states (DOS), the local density of states (LDOS), and the partial (or projected) local density of states (PLDOS) [18, 20]. The DOS(ω) of the system is the number of optical states allowed per unit volume, at the given frequency. This density of states does not provide us with information about the spatial distribution of the modes and the emitter position. Typically, the DOS is applied for an infinite space. LDOS ($\boldsymbol{r}, \omega$) indicates the number of modes available for emission at a specific position $\boldsymbol{r}$ and frequency ω. It depends on the emitter's electric field intensity at that position and considers the local availability of modes. The LDOS is important when the DOS varies in space and can be applied when the emitter has a random orientation in space. PLDOS ($\boldsymbol{n}_D, \boldsymbol{r}_D, \omega$) is important when the

LDOS depends on the emitter's orientation in space. PLDOS considers the strength of each mode based on the electric field projected along the dipole direction $\boldsymbol{n}_D$. For instance, if a dipole aligns with $\boldsymbol{n}_D$, it interacts more with modes having electric fields in the same direction and less with perpendicular fields. All these densities can be found using a Green function:

$$DOS = \ 2\frac{\omega}{\pi\ c^2\ V}\int_V d^3\boldsymbol{r}\ \mathrm{Tr}Im\{\overleftrightarrow{\boldsymbol{G}}(\omega)\} \tag{1.2}$$

$$LDOS = \ 2\frac{\omega}{\pi\ c^2}\mathrm{Tr}Im\{\overleftrightarrow{\boldsymbol{G}}(\boldsymbol{r}_D,\omega)\} \tag{1.3}$$

$$PLDOS = \ 2\frac{\omega}{\pi\ c^2}\boldsymbol{n}_D \cdot Im\{\overleftrightarrow{\boldsymbol{G}}(\boldsymbol{n}_D,\boldsymbol{r}_D,\omega)\}\cdot\ \boldsymbol{n}_D \tag{1.4}$$

Here $\overleftrightarrow{\boldsymbol{G}}$ is a Green function that is directly connected with an electric field generated from a point dipole in the particular environment. The electric field of a point dipole $\boldsymbol{E}_D(\boldsymbol{r}_D)$ at position $\boldsymbol{r}_D$ and evaluated at a position $\boldsymbol{r}_D$ is defined as [15]:

$$\boldsymbol{E}_D(\boldsymbol{r}_D) = \frac{\omega^2\ |\mu_D|}{c^2\ \varepsilon_0}\ \overleftrightarrow{\boldsymbol{G}}(\boldsymbol{r}_D,\omega), \tag{1.5}$$

where $|\mu_D|\ \boldsymbol{n}_D$ is the donor's dipole moment.

All the values in Eq. 1.2, 1.3, 1.4 denote the emission from a single dipole in a particular environment. The Purcell factor (F) or the enhancement of the densities of state is a quantity that indicates the emission rate of a quantum emitter when it is placed in a specific environment compared to when it is in free space:

$$F = \frac{PLDOS}{PLDOS^0} \tag{1.6}$$

Here and below, the superscript 0 represents the reference case of free space. A Purcell factor greater than 1 indicates an enhancement in the emission rate, while a factor less than 1 indicates a reduction.

1.2 Förster Resonance Energy Transfer

Förster Resonance Energy Transfer (FRET) is a near-field, nonradiative energy transfer process between two quantum emitters, called the donor and acceptor, which takes place at nanoscale distances. The FRET was first described in 1948 by Theodor Forster [21]. Overall, FRET is a well-characterized tool that enables non-radiative transfer of excitation energy between donor and acceptor fluorophores.

1.2.1 FRET rate

FRET occurs when the emission spectrum of the donor overlaps with the absorption spectrum of the acceptor, and the two molecules are placed in close proximity to

each other. Energy is transferred when the donor relaxes from its excited state to the ground state, and the acceptor excites from its ground state [15]. The energy level diagram and the overlapping spectra are shown in Figure 1.1 (b). The donor and acceptor possessing dipole moments $\boldsymbol{\mu}_D$ and $\boldsymbol{\mu}_A$, $\boldsymbol{n}_D$ and $\boldsymbol{n}_A$ are the unit vectors in the direction of the dipole moment. The distance between emitters is R. If the initial emission rate of the donor is γ_{rad}, then the presence of the acceptor provides additional decay channels through FRET. The energy is transferred directly, without being emitted into the environment, as happens in the case of spontaneous emission. The rate of energy transfer from the donor to the acceptor is called the FRET rate $\Gamma_{D\to A}$. The FRET rate can be affected by many factors. The distance between the donor and acceptor molecules plays a critical role in determining the efficiency of FRET. The FRET rate is inversely proportional to the sixth power of the distance between the donor and the acceptor $1/R^6$. Therefore, any changes in the distance in the nanometer scale can affect the FRET rate. Changes in the spectral properties of the donor or acceptor and their relative dipole orientations can also affect the FRET rate.

In optics, the FRET rate quantifies the power transferred from a donor to an acceptor. The Green function formalism can be used here to describe this mechanism. The amount of energy transferred from the donor to the acceptor is proportional to $|\boldsymbol{n}_A \cdot \overleftrightarrow{\boldsymbol{G}}(\boldsymbol{r}_D, \boldsymbol{r}_A) \cdot \boldsymbol{n}_D|^2$. Here, the Green function characterizes the electric field $\boldsymbol{E}(\boldsymbol{r}_A)$ generated by a point dipole source with dipole moment $\boldsymbol{\mu}_D$ oriented along $\boldsymbol{n}_D$ located at $\boldsymbol{r}_D$, at the acceptor position, which has an induced dipole moment $\boldsymbol{\mu}_A$ oriented along $\boldsymbol{n}_A$ located at $\boldsymbol{r}_A$.

Similarly, as the environment affects the spontaneous emission and LDOS, it is now understood that the FRET rate is also affected by the environment of the donor-acceptor pair. Enhancement of the FRET rate (F^R) quantifies how much the photonic environment affects the FRET rate:

$$F^R = \frac{\Gamma_{D\to A}}{\Gamma^0_{D\to A}}, \tag{1.7}$$

Here, the superscript 0 represents the reference case, where $\Gamma^0_{D\to A}$ is the FRET rate in the reference photonic environment, which is usually taken to be a free space. The $\Gamma_{D\to A}$ is the FRET rate modified by the particular environment. The effect of the photonic environment on FRET rate can be expressed theoretically as a ratio of the Green function [22]:

$$F^R = \frac{|\boldsymbol{n}_A \cdot \overleftrightarrow{\boldsymbol{G}}(\boldsymbol{r}_D, \boldsymbol{r}_A) \cdot \boldsymbol{n}_D|^2}{|\boldsymbol{n}_A \cdot \overleftrightarrow{\boldsymbol{G}}^0(\boldsymbol{r}_D, \boldsymbol{r}_A) \cdot \boldsymbol{n}_D|^2}, \tag{1.8}$$

Both FRET rate enhancement (Eq. 1.8) and PLDOS (Eq. 1.4) are connected with the Green function, that determined by the emitter's environment.

1.2.2 Relationship of FRET and LDOS

The connection between spontaneous emission and FRET is a topic of growing interest in photonics research. Although spontaneous emission of a single quantum emitter is influenced by the local photonic environment and the density of optical states [18, 23], the FRET rate is also dependent on the distance and orientation between the donor and acceptor. The idea of controlling the FRET rate by creating a photonic environment and controlling spontaneous emission has gained a lot of attention [5]. However, many experimental observations in this field led to seemingly contradictory conclusions.

On the one hand, some studies report enhanced FRET due to the generated photonic environment, demonstrating cases where energy transfer between emitters is greatly enhanced [11, 25, 6, 26, 16, 27, 12, 28, 29, 24]. On the other hand, other studies have found no noticeable effect on FRET when the photonic environment is manipulated. These results suggest that certain conditions may not result in any noticeable effect on energy transfer [8, 30, 31, 13, 32, 33, 34, 35]. Furthermore, there are cases where the engineered environment suppresses FRET, reducing the efficiency of energy transfer [36, 37, 38]. This contradiction of results highlights the complexity of the interactions between energy transfer and the photonic environment of emitters. A new experimental approach is needed to better understand the underlying mechanisms governing the FRET rate in the context of engineered photonic environments. The understanding of how to control the FRET rate by controlling the near electromagnetic environment of the donor-acceptor pair can open new possibilities in many fields of research.

1.2.3 Applications of FRET

In the visible spectrum, FRET acts as the main mechanism for energy transfer between quantum emitters, playing a key role in various chemical and biological processes with broad real-world applications. For example, solar light harvesting is based on FRET for efficient energy transfer in photovoltaic systems, which governs the conversion of sunlight into electricity [39, 40]. FRET plays an important role in the photosynthesis [41, 42] development of organic lighting sources, efficient and environmentally friendly lighting technologies [43, 44]. In single-molecule biophysics, FRET is a fundamental tool for studying molecular interactions and dynamics at the nanoscale [45]. Biosensing applications use FRET sensitivity to detect and quantify specific molecules, allowing fast and accurate analysis in applications ranging from medical diagnostics to environmental monitoring [46, 47]. Beyond its practical applications, FRET also plays a key role in our understanding of fundamental physical phenomena. This includes concepts such as strong coupling, where quantum emitters interact with confined electromagnetic modes, resulting in hybrid modes with unique properties [48, 49, 50]. Moreover, FRET studies many-body quantum systems, where interactions between multiple quantum emitters result in collective behavior [51, 52, 53]. The cooperative dipole-dipole interactions mediated by FRET provide informa-

tion on the collective behavior of quantum emitters, providing valuable information on phenomena such as energy transfer efficiency and spatial organization [54, 55, 56]. The wide application of FRET in chemistry, biology, and optoelectronics highlights its importance as a versatile and powerful tool for scientific research and technological innovation. Continued research on FRET mechanisms and their applications promises to facilitate further progress in various fields and pave the way for new methods and technologies.

1.2.4 Challenges of FRET measurements in the optical range

In optical experiments, the FRET rate is often determined indirectly by measuring the lifetime of donor molecules. The FRET rate is very sensitive to the distance between the emitters R and varies significantly depending on it. For very short distances, when the dipole-dipole distance is less than $\lambda/100$ (corresponding to $k_0R \approx 0.06$, deep subwavelength), the influence of the photonic environment on the FRET rate is usually minimal or weak[6, 8, 13, 35, 34]. On the contrary, in the far-field regime, where the separation distance exceeds several wavelengths, the presence of propagating surface plasmons or waveguide modes can significantly enhance energy transfer between dipoles[57, 14, 58, 59, 60]. This regime is characterized by conventional radiative energy transfer, with a distance dependence of $1/R^2$ in free space, in contrast to the FRET regime in the near field, where a characteristic distance dependence is $1/R^6$.

However, there is an intermediate dipole-dipole separation regime in the range of $R = \lambda/100$ to $R = \lambda/2$ ($0.06 < k_0R < 3$), known as the near-field regime [61, 62, 17]. In this regime, the energy-transfer process is driven by rich physics, but experimental measurements face challenges. Traditional FRET rate experiments in optics have difficulty accurately measuring energy transfer rates at distances greater than 15 nm or $\lambda/40$ ($k_0R \approx 0.16$) [16]. This is largely due to the technical difficulty in accurately controlling the dipole-dipole distance and orientation of each dipole emitter, which affects the FRET rate. The control of the FRET rate in this near-field region poses technical and conceptual challenges that require precise design of the photonic environment. However, single-molecule FRET techniques are now used to address some of these problems [27, 63, 64, 65]. Typical FRET rate experiments are performed with a large number of donor-acceptor pairs. Interpretation of the results of these experiments without precise knowledge of the dipole orientation often assumes orientation averaging, resulting in a loss of information about the role of dipole orientation in the FRET rate. An analogy between an energy transfer in optical and energy transfer for classical antennas in the microwave range was suggested to address these issues [6, 18].

1.3 Classical analogy to FRET rate enhancement

1.3.1 Classical antenna in the microwave range

In the microwave range, an antenna can be defined simply as a device for radiating or receiving radio waves, typically from hundreds of megahertz (MHz) to tens of gigahertz (GHz). All antennas produce electromagnetic radiation according to the principles of classical physics, as opposed to the principles of quantum mechanics in quantum emitters. Usually, they are referred to as "classical emitters" or "classical antennas". They are macroscopic objects that emit radiation from the movement of electric charges within them. Maxwell's equations fundamentally describe the induction and propagation in space of the electric field in classical electromagnetism. Microwave antennas come in various shapes and configurations, each optimized for specific applications. Common types of microwave antenna include dipole antennas, horn antennas, patch antennas, parabolic antennas, and phased array antennas [66]. The dipole antenna is one of the most fundamental and widely used antenna designs. It consists of a straight conductor or pair of conductors that are fed at the center or at one end, and the current has a sine distribution along the antenna. In the classical case, the antenna is center fed, and at the center, the current is at maximum amplitude, while it gradually decreases to zero at the ends of the antenna. Usually, the current in the antenna is approximated by a sine function, and this approximation works for all dipole lengths.

1.3.2 Near-field of the antenna

The regions surrounding an emitter are usually divided into far-field and near-field where the behavior of electromagnetic fields differs significantly due to the distance from the antenna [66]. The boundaries of these regions are not strict, and there are various criteria to distinguish them. However, there are distinct differences between these regions. From a microwave point of view, if we talk about antennas of finite size, in the far-field the phase difference of the emitted field from a different part of the antenna is negligibly small. The far field is the region farther away from the antenna, typically beyond a distance of several wavelengths from the antenna. In the far field, a radiation pattern is well-defined with properties such as directivity, polarization, and amplitude, which are determined by the antenna's design and orientation. However, in the near-field, the phase difference of the emitted field from a different part of the antenna is significant, and this error contributes to the measurements, as can be seen in figure 1.2. The near field is the region closer to the antenna, typically within a distance smaller than one wavelength from the antenna. In the near field, the electromagnetic fields produced by the antenna are dominated by reactive components (electric and magnetic fields), and the radiated energy does not propagate as electromagnetic waves but remains concentrated near the antenna.

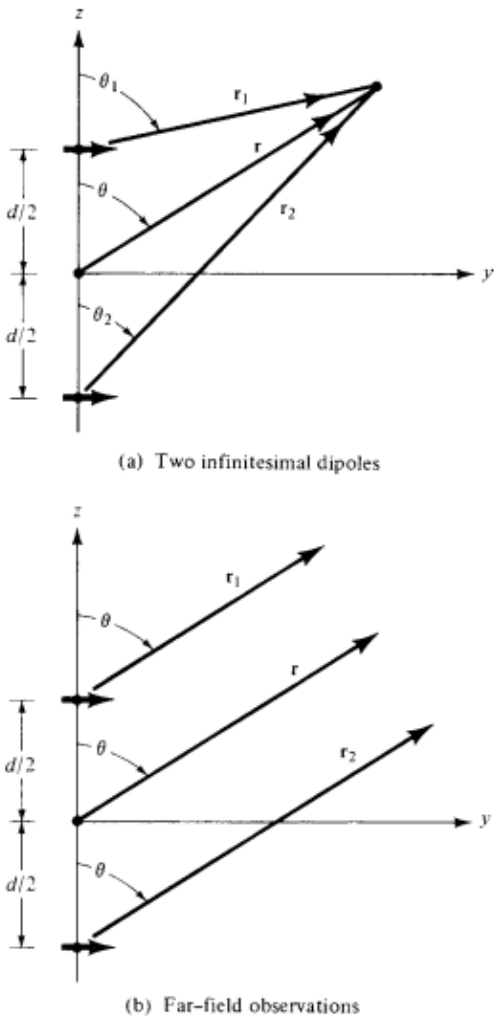

Figure 1.2 – Schematic observations of the antenna field at different distances using the example of a dipole antenna. (a) Near field, where the phase difference of the field radiated by each part of the antenna cannot be neglected. (b) far field, where this difference is negligible. (Source: [22])

The difference between the near- and far-field observations is shown in figure 1.2 on the example of a dipole antenna.

1.3.3 Basics of the microwave experiments

The energy is transferred to the antenna through a transmission line or the connecting network. For transmitting antennas, the feeding delivers the radio frequency signal from the generator (source) to the antenna element, where it is radiated as electromagnetic waves. For receiving antennas, feeding collects the incoming electromagnetic waves and delivers them to the receiver through the transmission line. A point where the input or output signals are measured is called a "port". Ports are the

connection points of a device with a transmission line and they are used to interface with external equipment such as signal generators, amplifiers, detectors, or other components of the measurement setup. A vector network analyzer (VNA) is usually used as a signal source and a device for measuring waves passing through a coaxial cable connected to the antenna. The number of measured parameters depends on the number of ports used for the measurements. The one-port and two-port networks are the most common and fundamental concepts in electrical engineering and circuit analysis, the schematic image is shown in Figure 1.3. They are used to model and analyze the behavior of electrical circuits and systems.

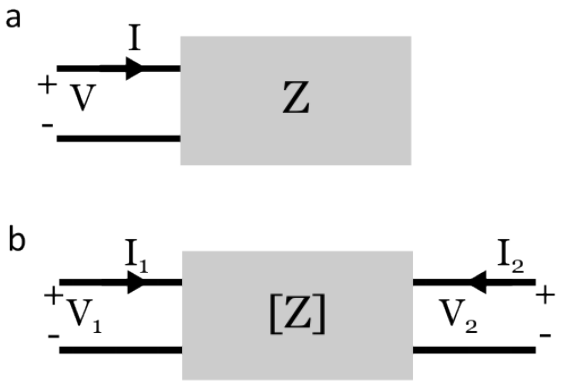

Figure 1.3 – Schematic illustration of (a) one-port and (b) two-port network

A one-port network is an electrical network with one port, for example, a single antenna connected to the VNA (figure 1.3 (a)). The behavior of a one-port network can be characterized by a single transfer function or impedance parameter, such as impedance (Z). An input impedance here is defined by the formula

$$Z_{in} = \frac{V}{I} \tag{1.9}$$

Where V is the voltage between the conducting terminals and I is the current flowing through the conductor in the transmission line. The input impedance is the impedance that an external source "sees" when trying to deliver power to the antenna and it is an important characteristic in the antenna design. When the input impedance of the antenna matches the impedance of the transmission line or the source feeding the antenna, the power transfer between the source and the antenna is maximized, leading to higher efficiency. The mismatch of the antenna and transmission line impedance leads to high reflections. The reference impedance of a coaxial cable is generally 50 Ohm, and for the best efficiency, the antenna has to match this impedance.

A two-port network is an electrical network with two ports, as it can be seen in figure1.3 (b). The behavior of a two-port network can be characterized by a set of four parameters like the impedance matrix $[Z]$ (Z parameters). Here, ports 1 and 2 have the corresponding currents and voltages (V_1 and I_1 at port 1 and V_2 and I_2 at port 2),

and we should consider the relationship (coupling) between the input and output voltages and currents.

$$\begin{bmatrix} V_1 \\ V_2 \end{bmatrix} = \begin{bmatrix} Z_{11} & Z_{12} \\ Z_{21} & Z_{22} \end{bmatrix} \begin{bmatrix} I_1 \\ I_2 \end{bmatrix} \tag{1.10}$$

Where Z_{11} is the impedance seen at port 1 when port 2 is terminated with its characteristic impedance; Z_{12} is the impedance seen at port 1 when port 2 is the source; Z_{21} is the impedance seen at port 2 when port 1 is the source, and Z_{22} represents the impedance seen at port 2 when port 1 is terminated with its characteristic impedance. In other words:

$$Z_{11} = \left.\frac{V_1}{I_1}\right|_{I_2=0} \quad Z_{12} = \left.\frac{V_1}{I_2}\right|_{I_1=0} \tag{1.11}$$

$$Z_{21} = \left.\frac{V_2}{I_1}\right|_{I_2=0} \quad Z_{22} = \left.\frac{V_2}{I_2}\right|_{I_1=0} \tag{1.12}$$

The diagonal elements of the Z matrix (Z_{12} and Z_{21}) determine the coupling between the ports and are called the mutual impedance. Since classical antennas follow the principle of reciprocity [66], $Z_{21} = Z_{12}$. Two-port networks are widely used to model more complex electrical circuits and systems, such as amplifiers, filters, transmission lines, and energy transfer of two antennas. The goal of microwave measurements is to collect and analyze the response of the ports.

1.3.4 Link between optical emitter and classical antenna for FRET and LDOS analogy

The electric field generated by the current flowing into the antenna can be reflected back, affecting its input impedance Z_{in}. In this way, the surrounding environment alters the antenna impedance through these reflected fields. This interaction essentially determines the amount of energy emitted. Conceptually, the radiation reaction can be understood as the extraction of energy from the oscillating current, which is then transferred to the available modes of the electromagnetic environment. The behavior of the antenna depends largely on the presence of available modes. If there are no available modes for radiation propagation, radiation does not occur, and if there are many propagating modes at the antenna location, the radiation becomes more efficient. Therefore, changes in impedance can provide insight into the antenna environment [18]. For sub-wavelength antennas, these measurements of impedance changes can be used to find the Purcell factor and the LDOS. The power radiated by the antenna can be written as $P = |I^2|Re(Z_{in})$, where I is an effective current in the antenna. Thus, the Purcell factor of a lossless antenna in the weak-coupling regime is:

$$F = \frac{P}{P^0} = \frac{Re(Z_{in})}{Re(Z_{in}^0)}. \tag{1.13}$$

Where index 0 indicates the reference case of a free space. The eq. 1.13 allows the direct measurements of the Purcell factor. Krasnok et al. in [67] demonstrated the measurement of the Purcell factor for microwave antennas through the input impedance, showing how LDOS regulates the amount of power emitted by the antenna. They measured a Purcell factor for electric- and magnetic- dipole antennas near perfect metallic mirror. The magnetic dipole is a simple wire loop that creates an electric field normal to its surface. The image of the antennas and the measurement results are shown in Figure 1.4. The solid blue and dashed red curves represent the theoretical calculations of the Purcell factor and squares and triangles correspond to the experiment. They showed that the Purcell factor exhibits oscillations with the period on the order of the wavelength when the source is moved vertically. These oscillations are due to interference of the initial field of the antenna and the reflected field that affects the input impedance.

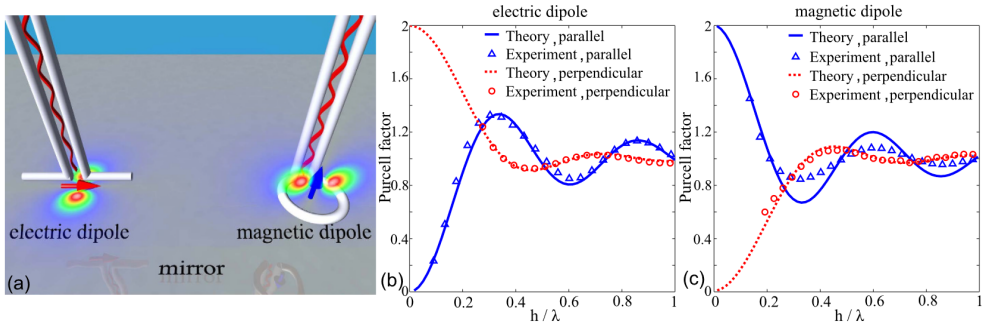

Figure 1.4 – Experiment to measure the Purcell factor in a microwave range. (a) Geometry of an electric dipole antenna and a magnetic dipole antenna near a perfect metallic mirror. Measured results for the Purcell factor along with the analytical results for (b) a parallel and (c) perpendicular orientations of the electric dipole antenna with respect to the mirror. (Source: [67])

Recent studies have also proposed using microwave measurements to investigate the dependence of FRET rate on the optical environment and LDOS [6, 20]. The mutual impedance Z_{21} characterizes the energy transfer ET between two antennas, similar to the Green functions used in optics for analytical calculations of the FRET rate. When the emitters are represented by dipole antennas significantly smaller than the wavelength, the mutual resistance Z_{21} of the corresponding microwave two-port network is proportional to the electric field and the Green function of the point dipole. This is the underlying physics of the Green function and the microwave antenna impedance analogy. Just as the effect of the photonic environment on FRET rate enhancement can be expressed theoretically as a ratio of the change in Green function Eq. 1.8, the impact of the environment on energy transfer can be described as a change in mutual impedance [6]:

$$\text{Energy transfer enhancement} = \frac{|Z_{21}|^2}{\left|Z_{21}^0\right|^2}. \tag{1.14}$$

The Z_{21} is the mutual impedance of the two-port network that describes the two dipoles. Here index 0 indicates the reference case without the presence of a conductive plane. The mutual impedance values for parallel $\left|Z^0_{21\text{parl}}\right|^2$ and aligned $\left|Z^0_{21\text{align}}\right|^2$ cases represent energy transfer from one antenna to another, as the FRET rate represents the transfer from a donor to an acceptor. The schematic image of this analogy is shown in Figure 1.5 of [6] as well as the dipole antenna used in these experiments. On the figure 1.5 (d), the characteristic decay of $1/R^6$ for near-field energy transfer is shown for parallel and aligned antennas.

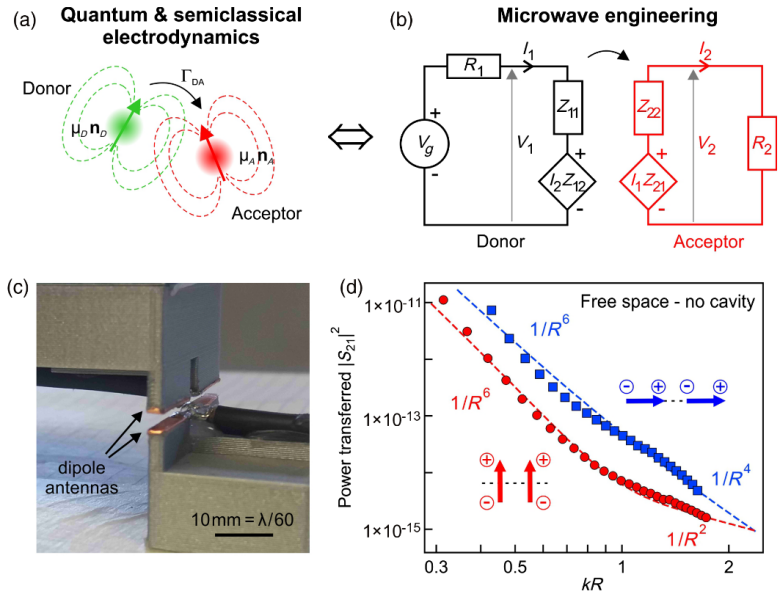

Figure 1.5 – Description of dipole-dipole energy transfer at (a) optical range from a quantum-mechanical point and from a (b) microwave point using a two-port network. (c) Photograph of two dipole antennas for microwave measurements. (d) Calibration of the dipole-dipole energy transfer power versus the dipole-dipole separation R in free space. Markers are experimental data for parallel dipoles (red) and aligned dipoles (blue) and dashed lines are theoretical predictions from Green's function theory (Source: [6])

Resonant energy transfer for quantum emitters means that the overlap between the donor's emission spectra and the emitter's absorption spectra is needed for this transfer to occur. However, for the classical antenna, the reciprocity theorem is valid, and the antenna can emit and detect at the same given frequency. For the classical antenna, we work outside the impedance resonance. Microwave measurements offer a direct way to quantify energy transfer because the emitters (antennas) are connected to coaxial cables. This contrasts with optical FRET rate enhancement measurements, where energy transfer is inferred from changes in the decay rate of the emitters (molecules). Therefore, microwave measurements provide an advantage over optical FRET rate measurements.

An important factor when interpreting FRET rate experiments in optics is the random orientation of the emitter's dipole moments. For many optical experiments with quantum emitters, the emitter's orientations are not known and the transfer rate has to be determined by a statistical average over many donor-acceptor pairs. The same applies to one single donor-acceptor pair with a random rotational diffusion. On the contrary, using microwave antennas as an example, we show that changing antenna orientation can enhance or suppress energy transfer depending on the environment, as predicted in [7].

Despite its advantages, the microwave antenna technique for FRET measurements has limitations. This is because the electrical size of the antennas is not as small as the atoms or molecules used for optical FRET experiments. The sizes of the typical emitters (atoms/molecules) in optical FRET are so small compared to the wavelength that electrically they can be considered randomly oriented infinitesimal point dipoles. Although microwave antennas are electrically larger than atoms and much smaller than wavelength, their size can still affect fields at short distances. This leads to the problem that we cannot assume a uniform field over the length of the antenna when measuring highly spatially varying phenomena such as the near-field energy transfer – it becomes necessary to account for the finite length of the antennas. An added motivation is that the use of an extremely small antenna presents measurement challenges. The shorter the antenna, the more inefficiently it acts as a transmitter and receiver, leading to weak signals. Since the input impedance of such an antenna is much smaller than the characteristic impedances of practical transmission lines, which have characteristic impedances of 50 or 75 ohms, it will present a large mismatch when connected. As a result, the overall efficiency of the antenna is very small [66]. For this reason, measurements are ideally carried out with the shortest possible antenna that provides a sufficient signal-to-noise ratio. By understanding the role of antenna length and carefully characterizing the deviation from point-dipole theory, we can identify the cases where longer antennas can be used, finding the right balance between power transfer and measurement accuracy. Our analytical model developed in this work, is based on calculating the mutual impedance Z_{21} of finite-length thin-wire dipole antennas without assuming a uniform current distribution over the antennas allowing us to characterize microwave FRET measurements with longer antenna lengths.

1.4 Outline

In this chapter, the theory of near-field effects like spontaneous emission and FRET rate was presented. The challenges of FRET measurements in the optical range include weak signal, lack of fine detail in spatial resolution, limitation of the dipole-dipole distance, and inability to control the orientation of the dipoles. These limitations can be critical for studying the effect of the nanophotonic environment on FRET. To overcome these limitations, an analogy of the FRET rate enhancement in the microwave range was previously suggested in [6]. We draw an analogy between the quantum emitters in the optical range and classical antennas in the microwave range

and describe the basics of experimental methods. Direct measurements of energy transfer between dipole antennas in the microwave range can provide sufficient signal, good spatial resolution, and full control over the position of the dipole. In the following chapters, we present new experimental and theoretical studies aimed at exploring the role of near-field control in energy-transfer.

2 Energy transfer near a PEC mirror for finite-size antennas

In this chapter, we expand our understanding of the FRET rate by studying the energy transfer for two dipole antennas placed next to a perfect electric conductor (PEC) mirror in the microwave range. An antenna length in this range determines the mutual impedance (Z_{21}) and input impedance (Z_{in}), which define the emission efficiency and energy transfer of the antennas. The antennas can be considered point dipoles only for very sub-wavelength sizes where the length can be neglected. However, since we work in the near field, an estimate of the error that may arise due to the actual size of the antenna is necessary. We discuss the effects of the finite length of the dipole antenna on energy transfer. We aim to develop an analytical model for energy transfer of the dipole antennas to show the comparison of the analytically calculated energy transfer in optical and microwave ranges and perform experiments in the microwave range to validate our theory and compare them with existing experiments in the optical range. Furthermore, we will perform an orientation averaging of the dipole antenna's orientation to match them with FRET rate enhancement and LDOS experiments in the optical range.

Related Article

— Kseniia Lezhennikova, Kaizad Rustomji, Pierre Jomin, Stanislav Glybovski, C. Martijn De Sterke, Jerome Wenger, Redha Abdeddaim, and Stefan Enoch. "Microwave analogy of Förster resonance energy transfer and effect of finite antenna length". en. In: *Scientific Reports* 14.1 (May 2024), p. 10485. ISSN: 2045-2322. DOI: 10.1038/s41598-024-59824-8

2.1 FRET rate enhancement near a PEC mirror

As a test bench for our approach, we use the simple geometry of the two dipoles placed near a PEC mirror. The FRET rate for this geometry was previously theoretically studied at optical frequencies ($\lambda = 628$ nm) by Wubs et al. [7], who developed an exact solvable analytical model of energy transfer near the PEC mirror using the point-dipole Green function formalism. We used this formalism to calculate the enhancement of the FRET rate in a wide range of dipole-dipole distance R and dipole-mirror height h, as shown in Figure 2.1 for (a) perpendicular, (b) parallel, and (c) aligned orientations. As was shown in [7], we show in Figure 2.1 that the FRET rate enhancement for each orientation changes depending on the dipole-dipole distance R and the dipole-mirror distance h. This geometry was also experimentally studied in the optical range by Blum et al. [8] but in a limited range of distances. The orientation of the dipoles to each other and the mirror wasn't fixed and the measurements were done for the many donor-acceptor pairs with random orientations of dipole moments. The results of these two works showed that the FRET rate is not affected by the mirror in the given ranges. The ranges explored in these two works are shown in Figure 2.1 (a), (b), and (c) with red boxes. Indeed, in the color map 2.1, when the dipole-dipole distances are small ($k_0R < 0.6$), the FRET rate gain is mostly 1, i.e it does not depend on the environment. Also, near the mirror ($k_0h < 0.5$), the influence of the reflected field is noticeable, the FRET rate experiences a sharp enhancement in the perpendicular orientation and a sharp quenching for the parallel. However, considering the wider range of possible parameters R and h, we can note some major trends. At large distances between dipoles ($k_0R > 0.6$), PLDOS has a more pronounced effect on the FRET rate. In this region for $k_0h < 1$ we observe a similar enhancement for the perpendicular orientation (see figure 2.1 (a)) and quenching for the parallel and aligned orientation (see figures 2.1 (b) and (c)). For $k_0h > 1$, the increase in FRET rate exhibits an oscillation pattern similar to PLDOS. This intermediate range of dipole-dipole separation R between $\lambda/100$ and $\lambda/2$ ($0.06 < k_0R < 3$) is challenging to study at the optical frequencies.

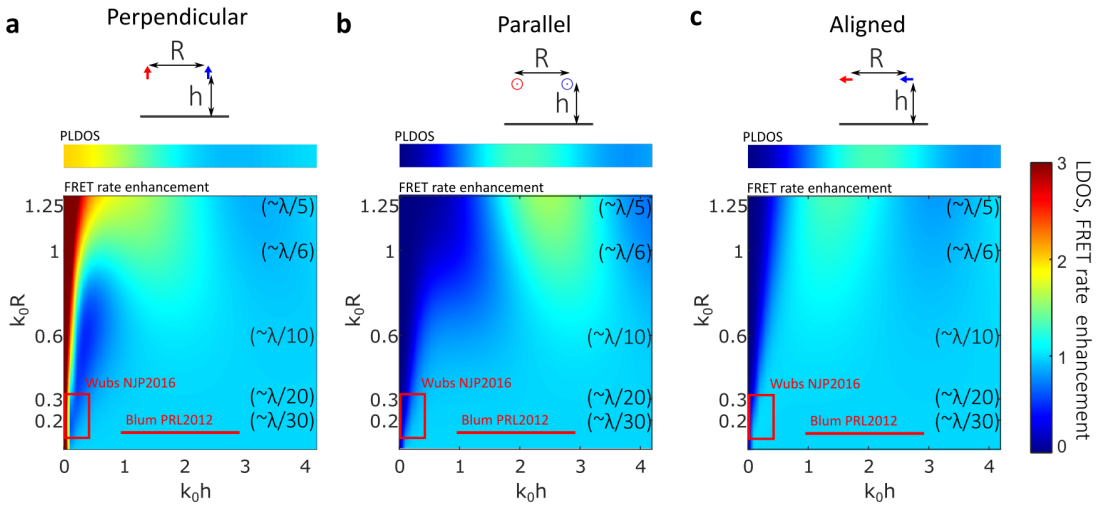

Figure 2.1 – PLDOS and FRET rate enhancements near a PEC mirror calculated with Green function formalism for (a) perpendicular, (b) parallel, and (c) aligned orientations. R is the dipole-dipole distance, k_0 is the wave number, and h is the dipole's height to the mirror. Red boxes denote the relative ranges studied in the previous works in optics [7, 8].

2.2 Analytical model for energy transfer for finite-size antennas in the microwave range

2.2.1 Finite sized-dipole antenna

In order to construct our theory, we examine two identical dipole antennas with length L. We use an approximation of wire-thin antennas, whose width is always much smaller than their length. We will refer to the antenna 1 as the donor and antenna 2 as the acceptor.

For dipole antennas in the microwave range, energy transfer can be defined through mutual impedance Z_{21} which can be found as [66]:

$$Z_{21} = -\frac{2}{I_{02}^* I_{01}} \int_{l_2=-L/2}^{L/2} E_{21}(l_2) I_2^*(l_2) dl_2. \tag{2.1}$$

This formula links the Z_{21} with an electric field $E_{21}(l_2)$ and with an induced current flowing along antenna 2 ($I_2(l_2)$). The electric field $E_{21}(l_2)$ here is a component of an electric field induced on the position of the acceptor antenna 2 by the donor antenna 1. The I_{01} is the amplitude of a current flowing in the donor antenna 1. The integral is taken over the antenna length L and the l_2 is the coordinate over the antenna length 2 ($-L/2 < l_2 < L/2$).

For the thin center-fed dipole we can use the current approximation with sinusoidal distribution over the length L, where the current vanishes at the endpoints ($l_2 = \pm L/2$),

and riches its maximum at the central point. In this case, the current induced in the acceptor antenna 2 can be written as

$$I_2(l_2) = I_{02}\frac{sin(k_0(L/2-|l_2|))}{sin(k_0L/2)}. \tag{2.2}$$

Where I_{02} is the amplitude of the current $I_2(l_2)$, $k_0 = 2\pi/\lambda$ is the wave number in the free space and λ is the wavelength. If the lengths of the antennas are infinitely smaller than the wavelength ($k_0L \ll 1$), we can go to the assumption that the electric field in Eq. 2.1 is the field of the point dipole, and the induced current and the electric field on the antenna 2 are uniform. This means that $E_{21}(l_2) \equiv E_{21}$, $I_2 \equiv I_{02}$ and the integral in Eq. 2.1 simplifies to

$$Z_{21} = -\frac{E_{21}L}{I_{01}}. \tag{2.3}$$

Here, Z_{21} is directly proportional to the electric field created by the donor E_{21}. Then upon substitution of Eq. 2.3 into Eq. 1.14 the length L cancels out, so the resulting energy transfer enhancement is independent of the length of the antenna. For all previous experiments measuring microwave analogs for optical phenomena such as spontaneous emission [68, 67, 69], FRET rate enhancement [6], and dipole-dipole interaction [20] this approximation was used. For these interactions occurring within the near field, where the distances are smaller than the wavelength ($k_0R \ll 1$), this approximation may be invalid. When the field became not uniform along the antennas, we could no longer use Eq. 2.3. The length of the antenna L modifies the energy transfer, and, at this point, we cannot treat our antennas as point dipoles. Consequently, the FRET rate enhancement, derived from the Green function formalism, may differ from the energy transfer obtained through the antenna impedance. Moreover, extremely short antennas are challenging to use in microwave experiments because they become inefficient and have weak signal strengths leading to very weak signals being measured.

To achieve a balance between measurement accuracy and the lowest possible power we can detect, we are developing a tool to calculate the error accumulated due to the size of the antenna relative to the dipole point. We are going to calculate the mutual impedance of the antennas without assuming field uniformity, using the equation. 2.1. To take into account the presence of the PEC mirror we are going to use a method of the image current. We find the energy transfer as a ratio of the mutual impedances, and we directly compare these results with the FRET rate enhancement for point dipoles under the same experimental setup.

2.2.2 Reference case in free space

2.2.2.1 Analytical solution

To begin with, we need to consider the reference case of two antennas in a free space. As in the previous chapter, the reference case is denoted by the superscript 0.

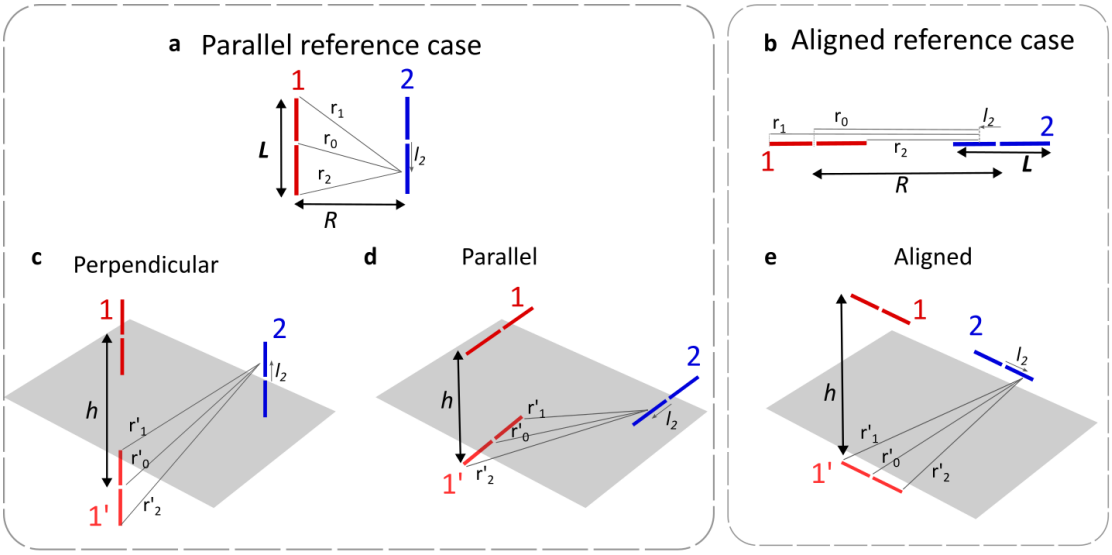

Figure 2.2 – Schematic view for the considered cases. (a) reference parallel case and (b) reference aligned case; Two dipole antennas with PEC mirror (c) perpendicular and (d) parallel orientation corresponded to the reference parallel case, (d) aligned case. Antennas 1 and 2 are the donor and the acceptor, respectively, 1' is an image antenna, which appeared due to the presence of a PEC mirror.

The mutual impedance Z_{21}^0 in free space will be found using equation 2.1. The electric field $E_{21}^0(l_2)$ induced at the antenna position 2 by the antenna 1 can be written as ([66] Chapter 8):

$$E_{21}^0(l_2) = -i\frac{k_0}{\omega\varepsilon_0 4\pi}\frac{I_{01}}{sin(k_0 L/2)}\left(\frac{exp(-ik_0 r_1)}{r_1} + \frac{exp(-ik_0 r_2)}{r_2} - 2cos(k_0 L/2)\frac{exp(-ik_0 r_0)}{r_0}\right). \tag{2.4}$$

Where $\frac{k}{\omega\varepsilon_0 4\pi} \simeq 30$ Ohm, $\boldsymbol{r}_0$ is the distance between the center of antenna 1 and the coordinate along the length of antenna 2 ($-L/2 < l_2 < L/2$). The r_1 and r_2 denote the distances between the ends of the antenna 1 and the point l_2. In free space, there are two main configurations: parallel (Fig. 2.2 (a)), when the antennas are oriented perpendicular to the line connecting their midpoints, and aligned (Fig. 2.2 (b)), in which the antennas are oriented parallel to this line. The values of r_1, r_2, and r_0 differ for each orientation, as indicated in the table 2.1. For antennas of finite size, R denotes the distance between their center points.

By substituting the induced electric field Eq. 2.4 and sinusoidal current distribution Eq. 2.2 into Equation 2.1, we derive an expression for the mutual impedance of two antennas of length L in a free space ([66] Chapter 8).

	Parallel $Z^0_{21_{\text{parl}}}$	Aligned $Z^0_{21_{\text{align}}}$
r_0	$\sqrt{R^2+l_2^2}$	$R+l_2$
r_1	$\sqrt{R^2+(L/2-l_2)^2}$	$R+l_2-L/2$
r_2	$\sqrt{R^2+(L/2+l_2)^2}$	$R+l_2+L/2$

Table 2.1 – Distances r_0, r_1, and r_2 are used in calculations of the mutual impedance from Eq 2.5 in the parallel ($Z^0_{21_{\text{parl}}}$) and aligned ($Z^0_{21_{\text{align}}}$) orientations in free space.

$$Z^0_{21} = i\frac{30}{sin^2(k_0L/2)}\int_{l_2=-L/2}^{L/2}\left(\frac{exp(-ik_0r_1)}{r_1}+\frac{exp(-ik_0r_2)}{r_2}-2cos(k_0L/2)\frac{exp(-ik_0r_0)}{r_0}\right)\cdot sin(k_0(L/2-|l_2|))dl_2 \tag{2.5}$$

To obtain a mutual impedance for parallel ($Z^0_{21_{\text{parl}}}$) and aligned orientations ($Z^0_{21_{\text{align}}}$), we need to use the values provided in Table 2.1 in Eq. 2.5. Explicit expressions for the mutual impedance $Z^0_{21_{\text{parl}}}$ and $Z^0_{21_{\text{align}}}$ are obtained by integration throughout the antenna length.

The parallel case is symmetrical and the integral can be divided by two identical integrals with integration limits from $l_2 = 0$ to $l_2 = L/2$. In this integration, we do not neglect any terms and seek a complete analytical solution without any simplifications or assumptions.

The final analytical form of the mutual impedances $Z^0_{21_{\text{parl}}}$ for free space is

$$\begin{aligned}Z^0_{21_{\text{parl}}} = 2i\frac{30}{sin^2(k_0L/2)}\cdot\\ \Big[\Big[1+2cos(k_0L/2)exp(-ik_0L/2)\Big]\Big[Ci(u_0)-Ci(u_2)-iSi(u_0)+iSi(u_2)\Big]+\\ \Big[1+2cos(k_0L/2)exp(ik_0L/2)\Big]\Big[Ci(u_0)-Ci(u_2')-iSi(u_0)+iSi(u_2')\Big]+\\ +exp(ik_0L)\Big[Ci(u_1')-Ci(u_2')-iSi(u_1')+iSi(u_2')\Big]+\\ +exp(-ik_0L)\Big[Ci(u_1)-Ci(u_2)-iSi(u_1)+iSi(u_2)\Big]\Big]\end{aligned} \tag{2.6}$$

Where $Si(x)$ and $Ci(x)$ are the Sine and Cosine integrals: $Si(x) = \int_0^x \sin(t)/t\,dt$ and $Ci(x) = -\int_0^x \cos(t)/t\,dt$,

$u_0 = k_0R$, $u_1 = k_0\left(\sqrt{R^2+L^2}-L\right)$, $u_1' = k_0\left(\sqrt{R^2+L^2}+L\right)$,
$u_2 = k_0\left(\sqrt{R^2+L^2}-L\right)$, $u_2' = k_0\left(\sqrt{R^2+(L/2)^2}+L/2\right)$.

The aligned case is not symmetrical and we first divide the integration domain in Eq.2.5 into two parts: from $l_2 = 0$ to $l_2 = L/2$ and from $l_2 = -L/2$ to $l_2 = 0$.

$$Z^0_{21_{\text{align}}} = i\frac{30}{sin^2(k_0L/2)}\left[\int_{l_2=0}^{L/2}\left(\frac{exp(-ik_0r_1)}{r_1}+\frac{exp(-ik_0r_2)}{r_2}-2cos(k_0L/2)\frac{exp(-ik_0r_0)}{r_0}\right)\cdot sin(k_0(L/2-l_2))dl_2+\int_{l_2=-L/2}^{0}\left(\frac{exp(-ik_0r_1)}{r_1}+\frac{exp(-ik_0r_2)}{r_2}-2cos(k_0L/2)\frac{exp(-ik_0r_0)}{r_0}\right)\cdot sin(k_0(L/2+l_2))dl_2\right] \tag{2.7}$$

By doing so we can remove the sign of modulus in the integral. Then we solve two integrals similarly to the previous case.

$$Z^0_{21_{\text{align}}} = \frac{i15}{sin^2(k_0L/2)}\cdot \tag{2.8}$$
$$\left[-ln\left(\frac{R-L/2}{R-L}\right)exp(-iu_1)+\left[Ci(2u_2)-Ci(2u_1)-iSi(2u_2)-iSi(2u_1)\right]exp(iu_1)+\right.$$
$$+ln\left(\frac{R+L}{R+L/2}\right)exp(-iu_1')-\left[Ci(2u_1')-Ci(2u_2')-iSi(2u_1')-iSi(2u_2')\right]exp(iu_1')+$$
$$+ln\left(\frac{R}{R-L/2}\right)\left[exp(-iu_0)+2cos(k_0L/2)exp(-iu_2)\right]-$$
$$-\left[Ci(2u_0)-Ci(2u_2)-iSi(2u_0)-iSi(2u_2)\right]\left[exp(iu_0)+2cos(k_0L/2)exp(iu_2)\right]-$$
$$-ln\left(\frac{R+L/2}{R}\right)\left[exp(-iu_0)+2cos(k_0L/2)exp(-iu_2')\right]+$$
$$\left.+\left[Ci(2u_2')-Ci(2u_0)-iSi(2u_0)-iSi(2u_2)\right]\left[exp(iu_0)+2cos(k_0L/2)exp(iu_2')\right]\right]$$

where $u_0 = k_0R$, $u_1 = k_0(R-L)$, $u_1' = k_0(R+L)$, $u_2 = k_0(R-L/2)$, $u_2' = k_0(R+L/2)$.

2.2.3 Comparison of the real-sized dipoles and point dipoles in free space

Figures 2.3 (a) and (b) show the energy transfer for finite antennas ($|Z^0_{21_{\text{paral}}}|^2$ and $|Z^0_{21_{\text{align}}}|^2$ from the equations 2.2.2.1 and 2.6) as a function of the antennas separation. We compare the mutual impedance of the dipole antennas of different sizes (colorful lines) with the FRET rate for point dipoles calculated with the Green function formalism (dashed black lines). All values are normalized by their maximum. The results for smaller antennas are expected to have a characteristic dependence $1/R^6$ (shown with gray lines in Fig. 2.3 in the near region ($k_0R < 1$). When the distance between emitters increases further ($k_0R > 1$), the energy transfer now follows the slope of $1/R^2$ for the

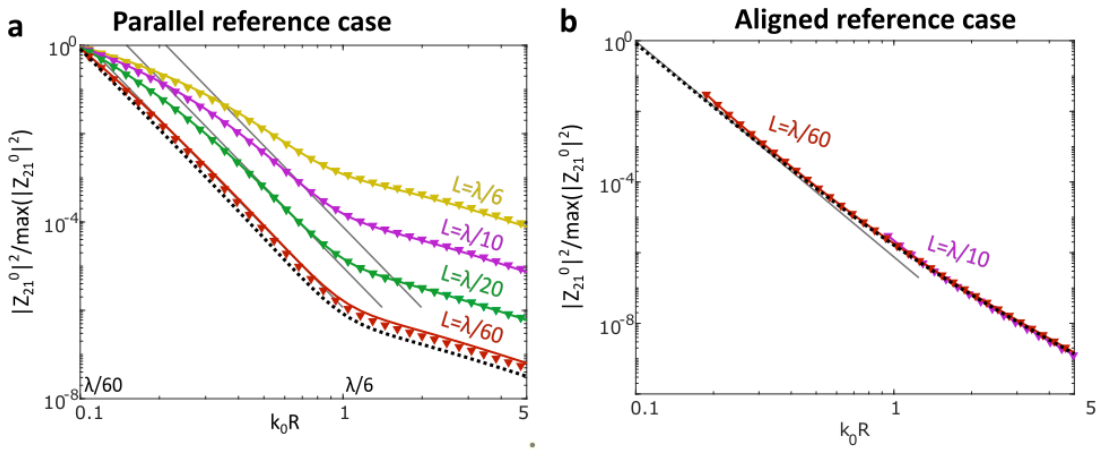

Figure 2.3 – Mutual impedance, normalized by the maximum, for the (a) parallel case $\left|Z^0_{21_{parl}}\right|^2$ and (b) aligned case $\left|Z^0_{21_{align}}\right|^2$ of the two finite antennas in the free space. The gray lines follow the slope $1/R^6$ for comparison. The dashed black line is the Fret rate calculated for an ideal point dipole. Colorful triangles correspond to the FDTD simulations.

parallel case and $1/R^4$ for the aligned case. The results for point dipoles closely match the expected trends. For both orientations, the mutual impedance behavior of smaller antennas ($L = \lambda/60$) is very close to the FRET rate for the point dipole (red line in Fig. 2.3). The other lines in Fig. 2.3 (a) show that the energy transfer between finite-sized antennas ($L > \lambda/60$) changes more slowly than the expected $1/R^6$ behavior for shorter distances ($k_0R < 1$). In the aligned configuration, the mutual impedance follows the FRET rate more consistently, but the length of the longer antennas prevents them from being placed closer than L. In this case, it is not possible to measure energy transfer in the near region.

By conducting simple numerical simulations, we confirmed our analytical results (triangles in figure 2.3). The simulations were done using the time-domain (FDTD) solver of CST Microwave Studio 2019. In the numerical model, the dipole antennas were made of PEC and driven by discreet ports placed in the gap between the branches.

For a better understanding of energy transfer in free space, it is interesting to consider the parallel case more thoroughly. In figure 2.4 we analyze changes in the slope of energy transfer within the range $0.12 < k_0R < 0.6$. In figure2.4 (a) we show a color map that illustrates the values of antenna length L and antenna separations k_0R where the dependence of energy transfer on distance deviates by more than ±5% compared to the expected dependence of $1/R^6$ (black region in the colormap). As the antenna length increases, the way the energy transfer varies with distance R significantly diverges from the expected $1/R^6$ trend associated with point dipoles and FRET. In figure2.4 (b) we plot the dependence of the averaged exponent of the energy transfer slope in the region $0.12 < k_0R < 0.6$ on the dipole length L. For antenna lengths L shorter than $\lambda/40$, we find that n is greater than 5.5 and close to 6, suggesting negligi-

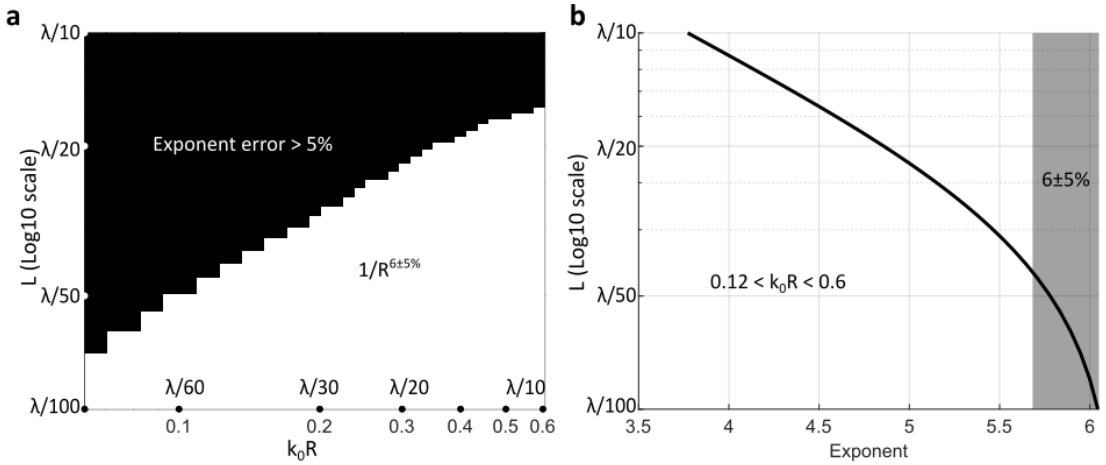

Figure 2.4 – Energy transfer in free space for parallel dipoles in the region $0.12 < k_0R < 0.57$. (a) Bicolor map showing the regions of antenna length L and antenna separations k_0R where the exponent of the energy transfer distance dependence deviates by more or less than 5% respective to the predicted $1/R^6$ dependence. (b) Distance dependence of the averaged exponent $1/R^n$ of energy transfer as a function of the dipole length L.

ble effects of finite size. However, with lengths greater than $\lambda/20$, the energy transfer behaves closer to a trend $1/R^4$. This is critical for guiding the design of experiments in which finite-size effects between dipole antennas in free space can be ignored. Short antennas with lengths less than $\lambda/50$ can be used to explore the entire range of $0.1 < k_0R < 1$. However, longer antennas with lengths around $\lambda/20$, offering a better signal-to-noise ratio, can still be utilized in a slightly narrower range of $0.4 < k_0R < 1$. Antennas with lengths exceeding $\lambda/10$ are not suitable for investigating energy transfer in free space.

2.2.4 Energy transfer for two finite-sized antennas near the PEC mirror

Finally, we can consider the same antennas near the PEC mirror; we will limit ourselves to the situation where the centers of both emitters are at the same distance h from the mirror. Schematic views of the geometries: parallel, perpendicular, and aligned, are shown in Figure 2.2 (c), (d), and (e), respectively. We note that when the mirror is removed, the parallel and perpendicular geometries become identical, corresponding to the parallel case in free space ($Z^0_{21_{perp}} = Z^0_{21_{\text{parl}}}$). To take into account the impact of the PEC mirror, we are using a method of image current [66]. The image current creates image antenna $1'$ with current $I'_1(l'_1)$ and excites an electric field $E'_{21}(l_2)$ as shown in figure 2.2 (c), (d), and (e). The resulting electric field $E_{21}(l_2)$ can be expressed as a superposition of the field generated by the antenna 1 ($E^0_{21}(l_2)$) in the absence of the PEC mirror and the field generated by the image antenna $1'$ ($E'_{21}(l_2)$)

[70, 71]:

$$E_{21}(l_2) = E^0_{21}(l_2) + E'_{21}(l_2). \tag{2.9}$$

The image antenna is identical to antenna 1 with the same current distribution (Eq. 2.2). Thus, the resulting mutual impedance Z_{21} can also be expressed as the sum of the mutual impedance of antennas 1 and 2 in free space (Z^0_{21} Eq. 2.5) and a mutual impedance of the image antenna $1'$ and antenna 2 (Z'_{21}):

$$Z_{21} = \underbrace{-\frac{2}{I^*_{02} I_{01}} \int_{l_2=-L/2}^{L/2} E^0_{21}(l_2)\ I^*_2(l_2)\, dl_2}_{Z^0_{21}} \underbrace{-\frac{2}{I^*_{02} I_{01}} \int_{l_2=-L/2}^{L/2} E'_{21}(l_2)\ I^*_2(l_2)\, dl_2}_{Z'_{21}}, \tag{2.10}$$

The Z'_{21} can be found with the same formula as we used in the reference case: Eq.2.5, but with different values for r'_0, r'_1, and r'_2, depending on their orientation as tabulated in Table 2.2. We have to take into account that for parallel and aligned orientations, antenna 1 and image antenna $1'$ are parallel to the PEC mirror. It results in an out-of-phase current flow in the image antenna $1'$ and a negative sign.

For parallel orientation, the final formula for Z'_{21} is:

$$\begin{aligned} Z'_{21_{\text{parl}}} = \frac{-15}{sin^2(k_0 L/2)} \cdot \\ \Big[\Big[Ci(u_0) - Ci(u_2) - iSi(u_0) + iSi(u_2)\Big]\Big(1 + 2cos(k_0 L/2) exp(-ik_0(L/2))\Big) + \\ \Big[Ci(u_0) - Ci(u'_2) - iSi(u_0) + iSi(u'_2)\Big]\Big(1 + 2cos(k_0 L/2) exp(ik_0(L/2))\Big) + \\ \Big[Ci(u'_1) - Ci(u'_2) - iSi(u'_1) + iSi(u'_2)\Big] exp(ik_0 L) + \\ \Big[Ci(u_1) - Ci(u_2) - iSi(u_1) + iSi(u_2)\Big] exp(-ik_0 L)\Big] \end{aligned} \tag{2.11}$$

Where $u_0 = k_0\sqrt{R^2 + (2h)^2}$, $u_1 = k_0\left(\sqrt{R^2 + (2h)^2 + L^2} - L\right)$, $u'_1 = k_0\left(\sqrt{R^2 + (2h)^2 + L^2} + L\right)$, $u_2 = k_0\left(\sqrt{R^2 + (2h)^2 + (L/2)^2} - L/2\right)$, $u'_2 = k_0\left(\sqrt{R^2 + (2h)^2 + (L/2)^2} + L/2\right)$.

For perpendicular and aligned cases (figure 2.2 (c) and (e)) the relative position of the antenna $1'$ and 2 and the path of integration are very similar, as a result, their mutual impedance Z'_{21} is going to look similar. To obtain the associated forms of r'_0, r'_1, and r'_2 for the aligned orientation, we need make a substitution $R \leftrightarrow 2h$ (Table 2.2), but keeping in mind the out-of-phase current flow. The resulting formula for both cases is:

	Perpendicular $Z'_{21_{\text{perp}}}$	Parallel $Z'_{21_{\text{parl}}}$	Aligned $Z'_{21_{\text{align}}}$
r'_0	$\sqrt{R^2+(2h+l_2)^2}$	$\sqrt{R^2+4h^2+l_2^2}$	$\sqrt{4h^2+(R+l_2)^2}$
r'_1	$\sqrt{R^2+(2h-L/2+l_2)^2}$	$\sqrt{R^2+4h^2+(L/2-l_2)^2}$	$\sqrt{4h^2+(R-L/2+l_2)^2}$
r'_2	$\sqrt{R^2+(2h+L/2+l_2)^2}$	$\sqrt{R^2+4h^2+(L/2+l_2)^2}$	$\sqrt{4h^2+(R+L/2+l_2)^2}$

Table 2.2 – Distances r'_0, r'_1, and r'_2 used in the calculation of mutual impedance between image antenna $1'$ and antenna 2, used for calculating the mutual impedance in the perpendicular ($Z'_{21_{perp}}$), parallel ($Z'_{21_{parl}}$), and aligned ($Z'_{21_{align}}$) configurations. A schematic can be seen in Figure 1 (a), (b), (c).

$$Z'_{21_{\text{perp}}} = -Z'_{21_{\text{align}}} = \frac{15}{sin^2(k_0L/2)}\cdot$$

$$\begin{aligned}
&\Big[\Big[Ci(u_0)-Ci(u_3)-iSi(u_0)+iSi(u_3)\Big]\Big(exp(ik_0(2h))+2cos(k_0L/2)exp(ik_0(2h-L/2))\Big)\\
&+\Big[Ci(u'_0)-Ci(u'_3)-iSi(u'_0)+iSi(u'_3)\Big]\Big(exp(-ik_0(2h))+2cos(k_0L/2)exp(-ik_0(2h-L/2))\Big)\\
&+\Big[Ci(u_0)-Ci(u_4)-iSi(u_0)-iSi(u_4)\Big]\Big(exp(ik_0(2h))+2cos(k_0L/2)exp(ik_0(2h+L/2))\Big)\\
&+\Big[Ci(u'_0)-Ci(u'_4)-iSi(u'_0)-iSi(u'_4)\Big]\Big(exp(-ik_0(2h))+2cos(k_0L/2)exp(-ik_0(2h+L/2))\Big)\\
&\quad+\Big[Ci(u_2)-Ci(u_4)-iSi(u_2)+iSi(u_4)\Big]exp(ik_0(2h+L))\\
&\quad+\Big[Ci(u'_2)-Ci(u'_4)-iSi(u'_2)+iSi(u'_4)\Big]exp(-ik_0(2h+L))\\
&\quad+\Big[Ci(u_1)-Ci(u_3)-iSi(u_1)+iSi(u_3)\Big]exp(ik_0(2h-L))\\
&\quad+\Big[Ci(u'_1)-Ci(u'_3)-iSi(u'_1)-iSi(u'_3)\Big]exp(-ik_0(2h-L))\Big]
\end{aligned}\tag{2.12}$$

Where for perpendicular case $u_0 = k_0\left(\sqrt{R^2+(2h)^2}+2h\right)$, $u'_0 = k_0\left(\sqrt{R^2+(2h)^2}-2h\right)$,
$u_1 = k_0\left(\sqrt{R^2+(2h-L)^2}+(2h-L)\right)$, $u'_1 = k_0\left(\sqrt{R^2+(2h-L)^2}-(2h-L)\right)$,
$u_2 = k_0\left(\sqrt{R^2+(2h+L)^2}+(2h+L)\right)$, $u'_2 = k_0\left(\sqrt{R^2+(2h+L)^2}-(2h+L)\right)$,
$u_3 = k_0\left(\sqrt{R^2+(2h-L/2)^2}+(2h-L/2)\right)$, $u'_3 = k_0\left(\sqrt{R^2+(2h-L/2)^2}-(2h-L/2)\right)$,
$u_4 = k_0\left(\sqrt{R^2+(2h+L/2)^2}+(2h+L/2)\right)$, $u'_4 = k_0\left(\sqrt{R^2+(2h+L/2)^2}-(2h+L/2)\right)$.

The coefficients for the aligned case are as follows:
$u_0 = k_0\left(\sqrt{R^2+(2h)^2}+R\right)$, $u'_0 = k_0\left(\sqrt{R^2+(2h)^2}-R\right)$,
$u_1 = k_0\left(\sqrt{(2h)^2+(R-L)^2}+(R-L)\right)$, $u'_1 = k_0\left(\sqrt{(2h)^2+(R-L)^2}-(R-L)\right)$,
$u_2 = k_0\left(\sqrt{(2h)^2+(R+L)^2}+(R+L)\right)$, $u'_2 = k_0\left(\sqrt{(2h)^2+(R+L)^2}-(R+L)\right)$,
$u_3 = k_0(\sqrt{(2h)^2+(R-L/2)^2}+(R-L/2))$, $u'_3 = k_0(\sqrt{(2h)^2+(R-L/2)^2}-(R-L/2))$,

$u_4 = k_0(\sqrt{(2h)^2 + (R + L/2)^2} + (R + L/2))$, $u_4' = k_0(\sqrt{(2h)^2 + (R + L/2)^2} - (R + L/2))$.

Finally, from the mutual impedance Z_{21} for antennas near a PEC mirror (Eq. 2.10) and the reference impedance of the free space Z_{21}^0 (Eq. 2.5) we determine energy transfer as in Eq. 1.14 for parallel, aligned, and perpendicular orientations.

2.2.5 Comparison of the real-sized dipoles and point dipoles near the PEC mirror

Figure 2.5 compares the energy transfer values for increasing antenna lengths ($L = \lambda/30$, $\lambda/10$ and $\lambda/6$) to FRET rate enhancement for point-dipoles for parallel and perpendicular orientations, calculated using the Green function. Our model also allows us to compute the error resulting from the dipole length L, which is shown in the figure as colormaps.

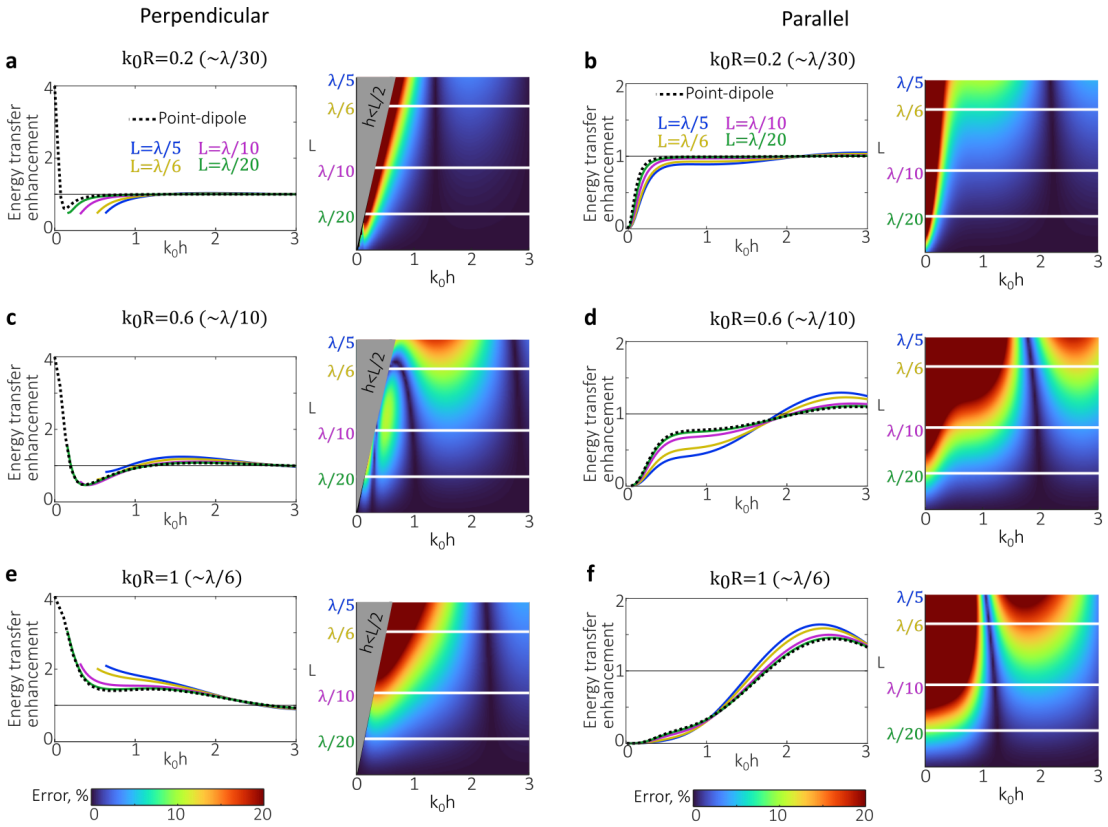

Figure 2.5 – Comparison of the energy transfer between two finite antennas with antenna length L (solid curves) and FRET rate enhancement for point-dipoles (dashed, black line) near a PEC mirror. The effects of finite-size are shown for parallel ((a), (c), and (e)), and perpendicular ((b), (d), and (f)) orientations for different antenna separation $k_0R = 0.2$ (a) and (b), $k_0R = 0.6$ (c) and (d), $k_0R = 1$ (e) and (f). On the right, color maps with percentage errors between the point dipole and finite-sized antennas are shown. The prohibited regimes of dipole positions for the perpendicular case are shown as gray areas in the colormaps. White lines highlight the dipole lengths shown in the graphs on the left.

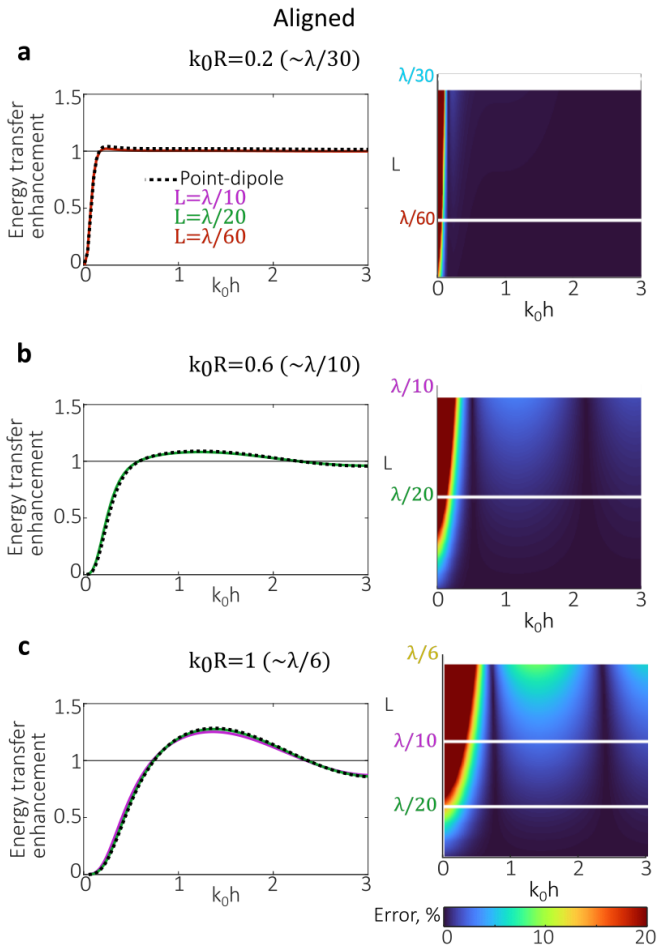

Figure 2.6 – Comparison of the energy transfer between two finite antennas with antenna length L (solid curves) and FRET rate enhancement for point-dipoles (dashed, black line) near a PEC mirror for aligned orientation. The effects of finite size are shown for different antenna separations $k_0R = 0.2$ (a), $k_0R = 0.6$ (b), $k_0R = 1$ (c). On the right, colormaps with percentage errors between the point-dipole and finite-sized antennas are shown. White lines highlight the dipole lengths shown in the graphs on the left.

The same analysis for the aligned orientation is shown in Figure 2.6. In this case, the considered range of antenna length is limited by geometry, since L cannot be larger than R. As we are limited with the shorter dipoles, the length impact is less pronounced. For the bigger $k_0R = 1$ shown in Figure 2.6 (c), the largest possible dipole length L is up to $\lambda/6$, and the resulting error is also increased.

With these figures, we show that the antenna length has a significant impact on energy transfer. Meanwhile, a qualitative agreement between energy transfer and FRET rate enhancement for point-dipoles is observed for all antenna lengths. For larger distances to the mirror ($k_0h > 0.5$) and smaller separations of the antennas $k_0R < 0.6$, energy transfer remains almost unchanged, as the antennas are too close

and the structure is effectively too far to influence the near field. As R increased, the energy transfer was influenced by the presence of the mirror, as the distance h between the antennas and the mirror varied. In the perpendicular configuration Figure 2.5 (a), (c), and (e) the theory predicts energy transfer by a factor of 4. In the perpendicular configuration, as the antenna-mirror distance decreases, the ends with opposite charge in antenna 1 and its image antenna $1'$ come close to the mirror and effectively create a single, larger dipole antenna. However, the energy transfer between parallel or aligned antennas and the mirror (Figure 2.5 (b), (d), and (f) and Figure 2.6 (a) - (c)) is quenched as the distance between the antenna and the mirror h decreases ($k_0 h < 0.5$), due to destructive interference of the antenna 1 and its mirror image antenna $1'$.

We can conclude that for smaller antennas ($L < \lambda/20$) this error is less than 10% and such antennas can be considered as point dipoles for measurements of energy transfer enhancement. For both parallel and perpendicular orientations, the biggest mismatch with point dipoles occurs and the shortest $k_0 h$. When antennas were moved away from the PEC mirror, the error was noticeably decreased. However, for bigger dipoles, especially for larger antenna separation $k_0 R$ the error became more significant.

This model gives us an accurate interpretation of microwave energy transfer experiments, particularly with long antennas, and requires the use of our analytical model to calculate the Eq. 1.14. Using this model, we can calculate the energy transfer enhancement for finite-sized antennas that match the FRET rate enhancement for infinite small dipoles, thus validating the measurements obtained with finite-sized antennas.

Input impedance of the dipole For the dipole antenna, the important parameter responsible for its efficiency is the input impedance, as discussed in the previous chapter. Input impedance strongly correlates with the length of the antenna. For small dipoles, the real part of the input impedance can be calculated as [66]:

$$Real(Z_{in}) = 20\pi^2 (L/\lambda)^2 \tag{2.13}$$

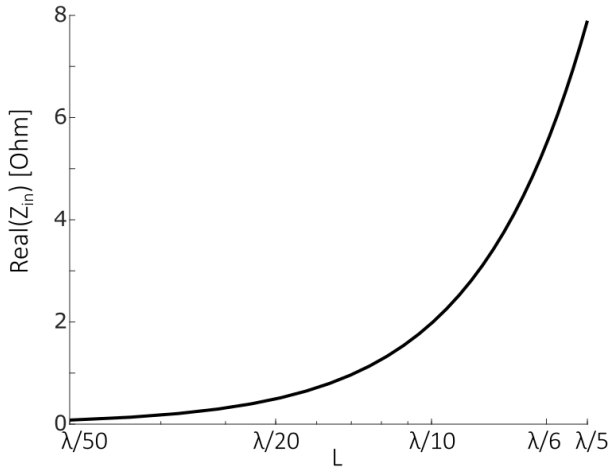

Figure 2.7 – A real part of the input impedance of dipole antenna as a function of its length L

Using this formula we calculate the input impedance for the dipoles that we use in the following experiments 2.7. For such small antennas, the estimated input impedance is less than 8 Ohm. It results in a very inefficient and mismatched antenna when connected to coaxial cable. Furthermore, the smaller the antenna we take to increase the accuracy of our measurements, the lower the signal we will have.

2.3 Measurements of the energy transfer near the PEC mirror at the Microwave range

To confirm our analytical results on the effect of antenna length on energy transfer, we carried out measurements with dipole antennas in the microwave range. For this purpose, dipole antennas with a length of $L = 10$ mm were made from a coaxial cable (Figure 2.8 (a)). The length was chosen to balance deviations from point dipole theory and keep the transmitted power within our measurement capabilities. The antennas were connected to an Anritsu MS2036C VNA using 1-meter coaxial cables. To ensure a stable positioning of the two antennas, they were mounted on a foam pad with a dielectric constant of $\varepsilon_r \approx 1.08$ next to a 1 x 1 meter square copper sheet. Copper is known to act as a perfect electrical conductor in the experiment frequency range (0.5 - 5 GHz). The copper sheet was fixed in a 3D positioning system for near-field measurements, as shown in Figure 2.8 (b). To ensure accurate data acquisition, the VNA was calibrated in the frequency range of 0.5–5 GHz at the end ports of coaxial cables. An Intermediate Frequency bandwidth (IFBW) of the VNA was 500 Hz, giving us higher resolution and a dynamic range up to 120 dB for accurate measurements. In the perpendicular case, the signal power was even lower, necessitating the use of a specialized electric field probe (MVG SAR PROBE SN 17/21 EP353). The measured voltage using the probe was up to 3*10-8 V. A technical error for the electric field probe

is around 1*10-9 V, which is smaller than the data points on the graphs and does not affect the calculations of the energy transfer.

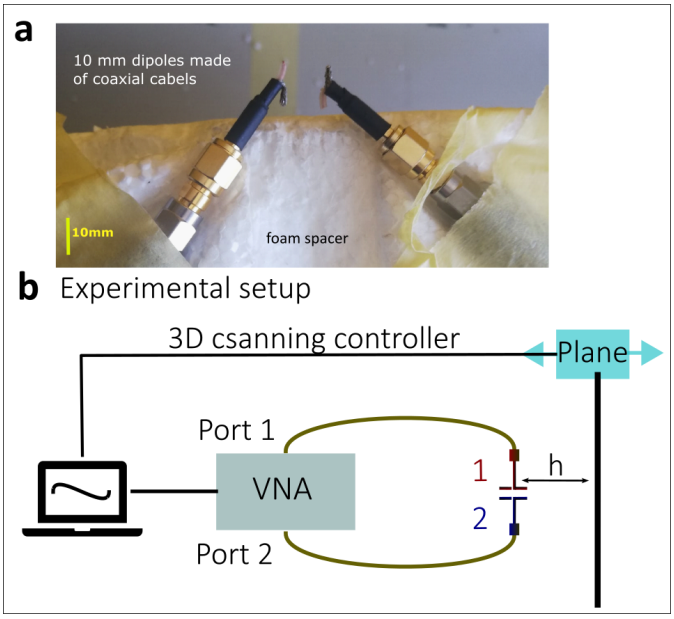

Figure 2.8 – Experimental setup for measuring energy transfer in the microwave range: (a) photo of the dipole antennas; (b) schematic view of the setup

Figure 2.9 shows the comparison of the experimental results of energy transfer enhancement and analytical calculations of FRET rate enhancement. The three vertical panels in Figure 2.9 illustrate the results for the three antenna orientations: perpendicular (left), parallel (middle), and aligned (right) near the PEC mirror. Experiments were carried out with fixed $R = 10$ mm and $L = 10$ mm at three frequencies: 1 GHz, which corresponds to $L = R = \lambda/30$ (Figure 2.9 (a), (d), (g)), 3 GHz corresponds to $L = R = \lambda/10$ (Figure 2.9 (b), (e), (h)) and at 5 GHz corresponds to $L = R = \lambda/6$ (Figure 2.9 (c), (f), (i)). To measure the dependence of the energy transfer on the antenna-mirror separation, the distance h between the antenna and the mirror was varied using a 3D positioning system with a $\Delta h = 1$ mm step size. Thus, high spatial resolutions of $\Delta h = \lambda/300$ at 1 GHz and $\Delta h = \lambda/60$ at 5 GHz.

The energy transfer measurements confirmed the major trends in the behavior of FRET rate enhancement for a wide range of distances. In each graph, we show a root mean square error between experimental results and theory for the point-dipoles. From our experimental results, follows that as the antenna size increased, the calculated energy transfer values matched the experimental data better than the FRET rate enhancement calculations for point-dipoles. This highlights the importance of considering the finite length of the antennas when interpreting microwave measurements accurately.

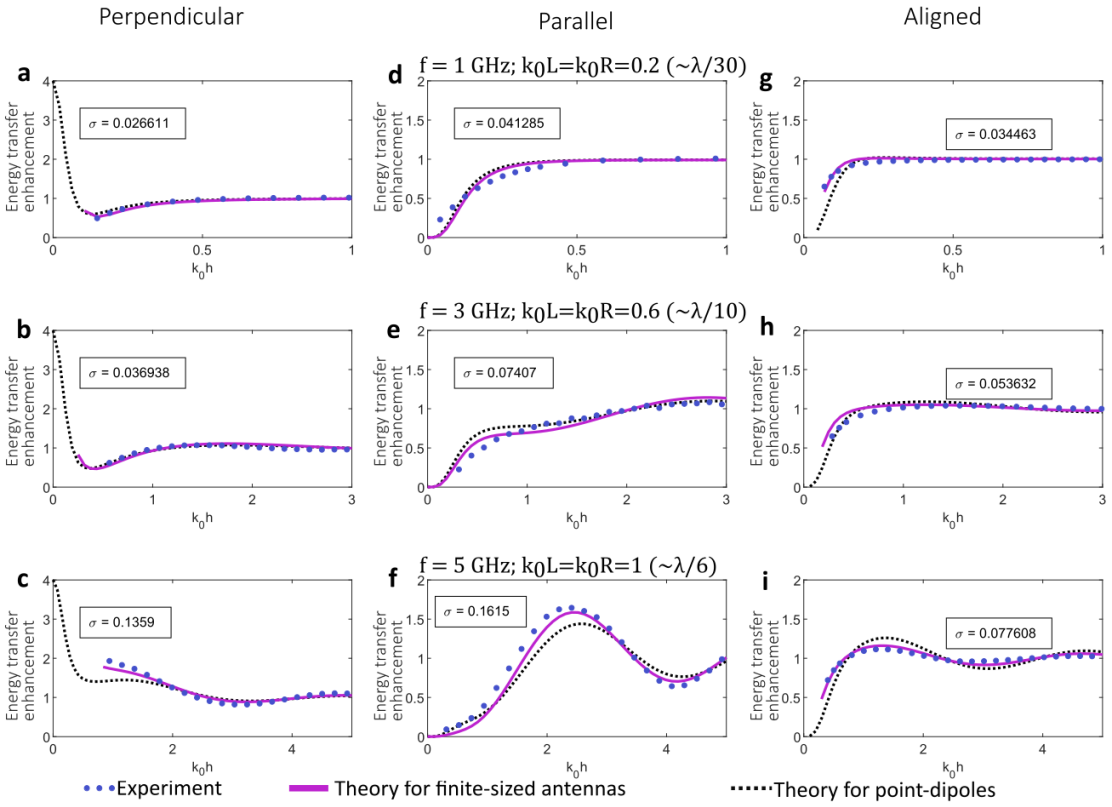

Figure 2.9 – Modification of energy transfer enhancement due to a PEC mirror for (a), (b), (c) perpendicular, (d), (e), (f) parallel, and (g), (h), (i) aligned configuration. The microwave measurements (Blue triangles) at 1 GHz (top row), 3 GHz (middle row), and 5 GHz (bottom row) were compared with analytical theory for finite antennas (purple) and FRET rate enhancement for point-dipoles (dashed, black). The length of the antennas is $L = 10$ mm and their separation is $R = 10$ mm. The root mean square error between experimental results and theory for the point-dipoles is shown in each case.

2.4 Energy transfer averaged over the dipoles orientations, comparison with FRET rate enhancement in optics

Optical measurements of FRET rate enhancement typically involve a large number of donor-acceptor pairs with random orientations of dipole moments [15]. The resulting FRET rate is averaged over orientations, and the exact position of the dipoles is unknown. This orientational averaging of FRET rate enhancement can be expressed through the sum of the components of the dyadic Green's tensor as

$$F_{\mathrm{av}}^{R} = \frac{\sum_{ij} |\hat{n}_{A_i} \cdot \overleftrightarrow{\boldsymbol{G}}(\boldsymbol{r}_D, \boldsymbol{r}_A) \cdot \hat{n}_{D_j}|^2}{\sum_{ij} |\hat{n}_{A_i} \cdot \overleftrightarrow{\boldsymbol{G}}^0(\boldsymbol{r}_D, \boldsymbol{r}_A) \cdot \hat{n}_{D_j}|^2}, \; i, j \; = \; x, y, z \tag{2.14}$$

In the microwave range, it is possible to mimic these experiments by measuring the energy transfer for all possible orientations and averaging the results. To do this, we fixed the distance between the antennas $R = 10$ mm, changing the antenna-mirror distance h, and measuring energy transfer at four frequencies: 0.5, 1, 3, and 5 GHz ($k_0 R = 0$, 1, 0.2, 0.6, and 1) with parallel, perpendicular, aligned, and cross-polarized antennas as shown in Figure 2.10 (a) to obtain

$$ET_{\mathrm{av}} = \frac{\sum \left| Z_{12_{ij}} \right|^2}{\sum \left| Z_{12}{}^{0}_{ij} \right|^2}, \; i, j \; = \; x, y, z \tag{2.15}$$

In Figures 2.10 (b)-(e), we demonstrate the agreement between the averaged energy transfer enhancement ET_{av} from our measurements and the $\mathrm{FRET}_{\mathrm{av}}$ rate enhancement for point dipoles of the equation 2.14. As expected, the $\mathrm{FRET}_{\mathrm{av}}$ rate enhancement decreases with decreasing mirror-plate distance ($k_0 h < 0.5$) due to quenching in the parallel and aligned orientations. When the distance between the dipole and the mirror increases ($k_0 h > 0.5$) and for smaller dipole separations R, the impact on the enhancement of $\mathrm{FRET}_{\mathrm{av}}$ is negligible ($\mathrm{FRET}_{\mathrm{av}} \approx 1$). Only for larger separations R (Figure 2.10 (e)), the $\mathrm{FRET}_{\mathrm{av}}$ rate enhancement is affected by the PEC mirror.

Our experiments for a smaller antenna were consistent with a previous theoretical study by Wubs et al. [7] and experimental work [8], which investigated the enhancement of the FRET rate enhancement in the optical range ($\lambda = 628$ nm) for a similar geometry. The energy transfer is not affected by the mirror when the dipoles are close to each other $R < \lambda/60$ and far from the mirror ($k_0 h > 0.5$). A similar behavior was shown at the optical frequency $\lambda = 570$ nm, where the dipole-dipole distance was $R = 6.8$ nm ($\lambda/77$), and the dipole-mirror distances ranged from 60 to 270 nm ($0.7 < k_0 h < 3.2$). The study also concluded that the metallic plane does not affect the FRET rate enhancement in this range, and $\mathrm{FRET}_{\mathrm{av}} \approx 1$. Our results indicate that observation of the effect of the PEC mirror on the FRET rate may be possible for a larger $k_0 R$ or closer distance to the mirror $k_0 h$. However, the dramatic increase in the FRET rate can only be observed when the dipoles are perpendicular to the mirror, and this possibility requires further research in the optical range.

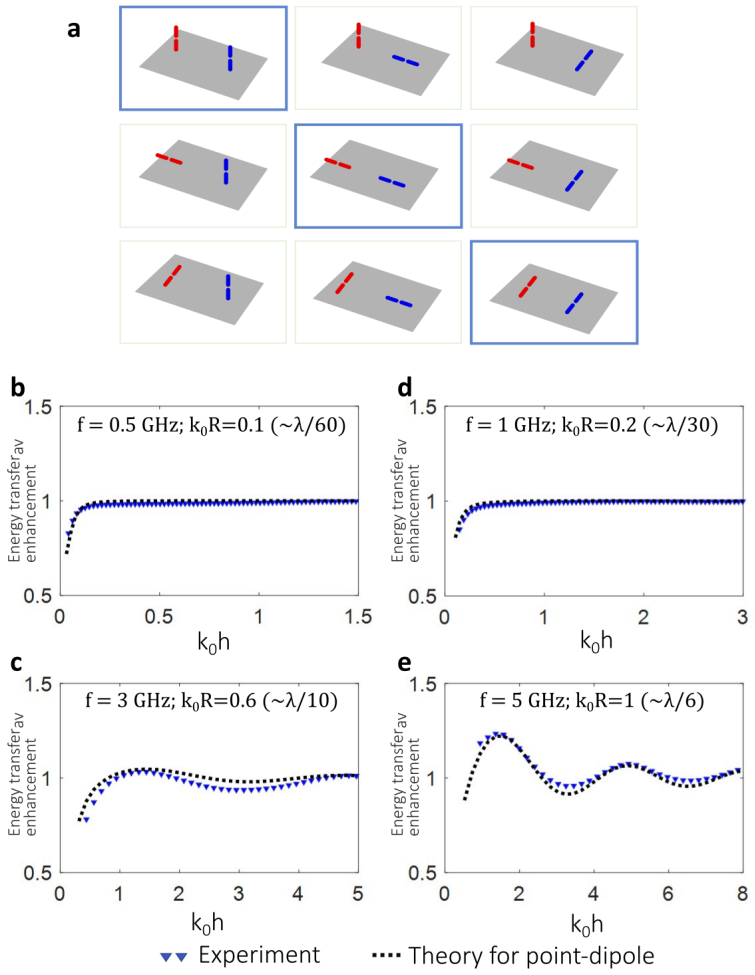

Figure 2.10 – Averaging of energy transfer over orientation: (a) Schematic of all orientations for obtaining orientation averaged energy transfer. The averaged energy transfer enhancement as a function of antenna-mirror distance $k_0 h$ at (b) 0.5 GHz, (c) 1 GHz (d), 3 GHz, and (e) 5 GHz at fixed antenna to antenna distance $R = 10$ mm and antenna lengths $L = 10$ mm. Experiments (blue triangle) compared with point-dipole-based calculations for orientation averaged FRET rate enhancement (black dashed line).

2.5 Measurements of the LDOS near the PEC mirror

In addition to averaging the energy transfer, we can also measure the PLDOS of a single-dipole antenna near the PEC mirror and find its average over orientation. For this, we measured the reflection coefficient S_{11} of the dipole placed parallel and then perpendicular near the mirror in the absence of a second dipole. In these measurements, we used the same dipole antennas and VNA as for the energy transfer. The PLDOS enhancement or the Purcell factor can be calculated as [67]

$$F = \frac{Re(Z_{in})}{Re(Z_{in}^0)} = \frac{\Gamma_D}{\Gamma_D^0} = \frac{\boldsymbol{n}_D \cdot Im(\overleftrightarrow{\boldsymbol{G}}(\boldsymbol{r}_D, \boldsymbol{r}_D)) \cdot \boldsymbol{n}_D}{\boldsymbol{n}_D \cdot Im(\overleftrightarrow{\boldsymbol{G}^0}(\boldsymbol{r}_D, \boldsymbol{r}_D)) \cdot \boldsymbol{n}_D}, \tag{2.16}$$

where R_{in} is the input impedance of the dipole antenna.

$$Re(Z_{in}) = Z_w \frac{1 - (Re(S_{11}))^2 - (Im(S_{11}))^2}{(1 - Re(S_{11}))^2 + (Im(S_{11}))^2}, \tag{2.17}$$

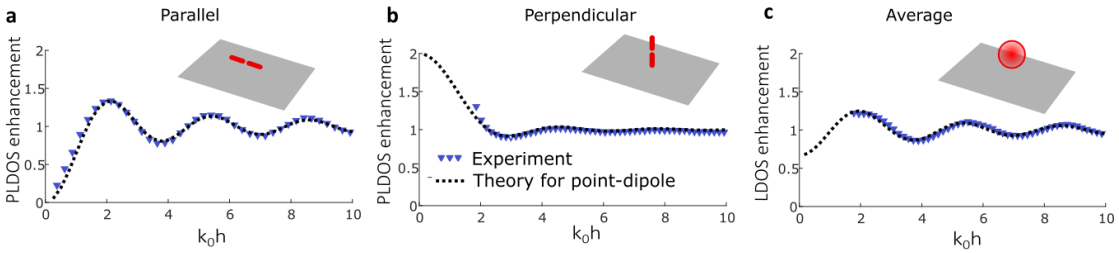

Figure 2.11 – LDOS and PLDOS of dipole antenna placed near the PEC mirror, experimental and analytical results for (a) parallel, (b) perpendicular polarisation and averaged polarization

If the reflected field is in phase with the original field emitted by the emitter, the PLDOS (or emission rate for a quantum emitter) increases, and vice versa. The period of oscillation is approximately half the wavelength of the radiation. As the distance between the emitter and the mirror increases, the amplitude of the oscillations decreases because of a decrease in interference contrast. At large emitter-mirror distances, PLDOS asymptotically approaches the value determined by the underlying medium (free space), regardless of the mirror. The image current neutralizes radiation for a parallel dipole (Figure 2.11 (a)). However, when the dipole is oriented perpendicularly, the image of the dipole in the PEC mirror doubles the radiation strength (see Figure 2.11 (b)). The orientation of the dipole affects the spatial location of the maxima and minima of PLDOS oscillations, since different orientations create different polarized electromagnetic fields at the surface that affect the dipole. As mentioned in Chapter 1, there are three levels of description of densities of states depending on the granularity of the description. When we average the PLDOS on every emitter orientation, we get the LDOS. To calculate the average PLDOS enhancement or LDOS enhancement across dipole orientations, we used the formula:

$$F = \frac{2Re(Z_{in_{\text{parl}}}) + Re(Z_{in_{\text{perp}}})}{3Re(Z_{in}^0)} \tag{2.18}$$

As for PLDOS, LDOS also has a similar oscillation pattern for $k_0 R > 1$, see Figure 2.11 (c). Because parallel dipole orientation has twice the effect on LDOS than perpendicular orientation, LDOS cancels out as the dipole approaches the mirror, but LDOS does not cancel out to 0. In the optical range with a real metal mirror, the situation

is more complex and surface modes also affect the radiation near the metal. We will look at this case in more detail in the next chapter.

2.6 Outline

The analytical model developed in this study explicitly considers the effect of antenna size on energy transfer by calculating the mutual impedance of a two-port network consisting of two identical antennas of finite size. The results obtained from the model were confirmed through microwave measurements near the PEC mirror, and good agreement was found with a previous theoretical study on FRET rate enhancement in the optical range. We noted the difference between energy transfer for finite-sized antennas and FRET rate enhancement for point dipoles.

We compared our model with experimental results with high spatial resolution ($\Delta h = \lambda/300$ at 1 GHz and $\Delta h = \lambda/60$ at 5 GHz) and FRET rate enhancement for the point dipoles. For the cases where the dipole length has an impact on the measurements ($L > \lambda/20$) our model can give us an estimate of the error due to the dipole length. We can measure energy transfer from the near-field to the intermediate regime for antenna separations R ranging from $\lambda/30$ to $\lambda/6$. The study also highlights the importance of dipole orientation for FRET rate enhancement and LDOS measurements, which can be mimicked in the microwave range by measuring energy transfer for all possible orientations and averaging the result. The results showed good agreement between the FRET rate enhancement and the averaged energy transfer measured for all frequencies. Overall, this chapter provides a comprehensive understanding of the effects of antennas' finite-size impact on the FRET rate in the near-field regime and the FRET rate enhancement near the PEC mirror.

3 Near-field control with metasurface in the microwave range

In this chapter, we shifted our attention to metasurfaces and their use to control the near field. In the first section, we review the metasurface properties and near-field measurement methods of a metasurface. We consider a hyperbolic metasurface to detect an effect of the anomalous reflection on its edge. In the second part of the chapter, we introduce a specialized metasurface designed to support surface waves similar to the SPs [72] found at metal boundaries in optics but operating at microwave frequencies [73, 74] to study how the electromagnetic environment and SPs affect the energy transfer and LDOS. A comparison with a PEC mirror clearly illustrates the ability of surface waves to enhance energy transfer and LDOS in the near-field regime. The connection between energy transfer and LDOS with the presence of an SPs and a PEC mirror is also considered.

Related Article

— Kseniia Lezhennikova, Kaizad Rustomji, Boris T. Kuhlmey, Tryfon Antonakakis, Pierre Jomin, Stanislav Glybovski, C. Martijn De Sterke, Jérôme Wenger, Redha Abdeddaim, and Stefan Enoch. "Experimental evidence of Förster energy transfer enhancement in the near field through engineered metamaterial surface waves". en. In: *Communications Physics* 6.1 (2023), p. 229. ISSN: 2399-3650. DOI: 10.1038/s42005-023-01347-1

— Ilya Deriy, Ksenia Lezhennikova, Stanislav Glybovski, Pavel Belov, Ivan Iorsh, Mingzhao Song, and Andrey Bogdanov. "No reflection paradox at the boundary of hyperbolic medium". In: *Optical Manipulation and Structured Materials Conference*. Ed. by Takashige Omatsu, Síle N. Chormaic, and Kishan Dholakia. Yokohama, Japan: SPIE, Sept. 2023, p. 45. DOI: 10.1117/12.3008377

3.1 Introduction to Metasurface

3.1.1 Definition and versatility of Metasurfaces

The metasurface is a two-dimensional array of sub-wavelength elements or structures designed to control electromagnetic waves in unconventional ways [74, 75, 76]. Unlike traditional bulk materials, which respond to electromagnetic waves depending on their bulk characteristics, metasurfaces are able to realize precise and unique optical effects. These structures can be used to manipulate various aspects of electromagnetic waves, including amplitude, phase, polarization, and direction[74].

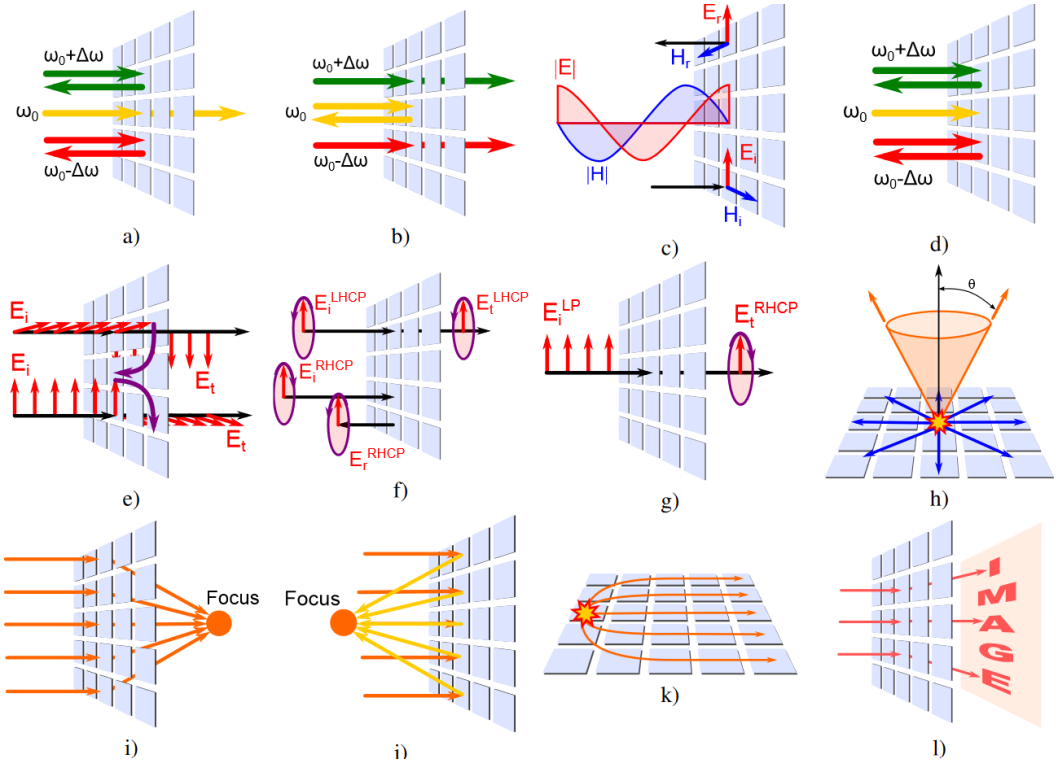

Figure 3.1 – Examples of the metasurface functionalities: a — bandpass frequency selective surface; b — bandstop frequency selective surface; c — high impedance surface; d — narrowband perfect absorber; e — twist polarizer; f — right-handed circular-polarization frequency selective surface; g — linear-to-circular polarization converter; h — two-dimensional leaky-wave antenna with a conical-beam pattern; i — focusing transmit array; j — focusing reflectarray; k — flat Luneburg lens; l — hologram (Source: [74])

Some examples of metasurface applications for the manipulation of electromagnetic waves are shown in figure 3.1. Bandpass frequency selective surfaces (FSS) (figure 3.1 (a)) are designed to transmit electromagnetic waves in a chosen frequency range while blocking or attenuating waves at other frequencies. The bandstop FSS (Figure

3.1 (b)), unlike the bandpass FSS, blocks or attenuates waves at a certain frequency while allowing waves at other frequencies to pass through. A high-impedance surface (Figure 3.1 (c)) is a metasurface with a high impedance to incident electromagnetic waves at certain frequencies. Unlike the PEC surface, the magnetic field vanishes $|H| = 0$ on the boundary of such a surface. It can be used to improve the efficiency of reflectors and suppress surface waves. The narrowband ideal absorber (Figure 3.1 (d)) absorbs electromagnetic waves in a narrow frequency range. A twist polarizer (Figure 3.1 (e)) converts linearly polarized light into twisted polarized light. A circularly polarized right-handed FSS (Figure 3.1 (f)) selectively transmits or reflects circularly polarized electromagnetic waves of the right-handed hand while blocking circularly polarized waves of the left-handed hand. A linear to circularly polarized converter (figure 3.1 (g)) converts linearly polarized light to circularly polarized light or vice versa. It is used in applications requiring polarization manipulation, such as antennas, imaging systems, and optical communications. The 2D leaky wave cone antenna (Figure 3.1 (h)) is a metasurface antenna that emits electromagnetic waves with a cone pattern. A focusing transmit array (Figure 3.1 (i)) and a focusing reflective array (Figure 3.1 (j)) are a metasurfaces capable of focusing electromagnetic waves to a specific point or region in space. A flat Luneburg lens (figure 3.1 (k)) is a metasurface-based lens with properties similar to conventional Luneburg lenses but with a flat and compact structure. A metasurface hologram (figure 3.1 (l)) is a two-dimensional optical element capable of reconstructing three-dimensional images or patterns when illuminated with coherent light. These selected features demonstrate the versatility and potential of metasurfaces to control electromagnetic waves.

In metamaterials and metasurfaces, unit cells, often called artificial or metaatoms, have a much shorter lattice period relative to wavelength ($a << \lambda$). As a result, the electromagnetic wave "sees" only the effective parameters rather than interacting with individual unit cells. Metamaterials and metasurfaces can be described using effective magnetic permeability (μ_{eff}), effective electrical permeability (ε_{eff}), or effective conductivity (σ_{eff}). Similarly to metasurface, photonic crystals (PCs) consist of periodical sub wavelength unit cells. The concept of PCs predates metamaterials and metasurfaces. Still, both concepts are now widely discussed in various scientific and engineering fields, and the boundary between them is not strictly defined. Nevertheless, we try to distinguish between the concepts of metasurfaces and PCs. In PC, the unit cell and lattice constant must be comparable in size to the wavelength ($a \approx \lambda$) to manipulate the electromagnetic wave by its diffraction on the lattice. We discuss PCs in more detail in the next Chapter.

Metasurfaces and PCs are known for their ability to manipulate nearby sources, enhancing or suppressing their emission [77]. It was demonstrated for different sources, including microwave antennas [78] and near-infrared quantum dots [79]. In addition, they promote diffraction-free propagation and long-range supercollimation [80, 81, 82], enabling alignment-free self-guiding at specific frequencies [83]. These effects appear due to the change in the local density of states through smoothing of the isofrequency contours at given frequencies[84, 85, 86, 87]. By tailoring the geometry, composition, and arrangement of meta-atoms, metasurfaces, and PCs offer

a powerful platform for realizing advanced optical and electromagnetic devices with new features and capabilities. The versatility of metasurfaces has found applications in various fields such as optical, photonic, and telecommunications, highlighting their importance in modern technological advances.

3.1.2 Dispersion and isofrequency contours

Metasurfaces and PCs are periodic structures, and they require special tools for their analysis and description, such as a dispersion diagram and isofrequency contours (IFCs). The dispersion diagram illustrates how the frequency ω (or wavelength λ) of electromagnetic waves propagating through a periodic structure is related to their wave vector k. The dispersion relations may vary depending on the specific geometry and material properties of the periodic structure. It shows the allowed propagation modes or bands of the structure, the bands represent ranges of allowed frequencies and wave vectors for which electromagnetic waves can propagate through the structure. An IFC is a k-space curve representing all possible wave vectors k corresponding to a specific frequency ω (or wavelength λ) of electromagnetic waves propagating through a periodic structure. It provides a visual representation of how the wave vector varies depending on the direction of propagation. Isofrequency contours can be used to analyze dispersion properties such as directivity and anisotropy of wave propagation within a structure. The IFCs of the media allow us to find all possible states of light accessible for scattering. The curvature and topology of IFCs crucially affect the structure of transmitted and reflected waves[88, 89]. Usually, the desperation diagram and the IFCs represent the wavevectors in the first Brillouin zone [90]. The first Brillouin zone describes a unit cell in the k space associated with the periodicity of the structure and contains all possible wavevectors for propagating waves in the periodic structure.

3.1.3 Types of anisotropy and Hyperbolic Metasurface

In conventional isotropic surfaces, the IFCs in k-space are described by $k_x^2 + k_y^2 = \omega^2/c^2$ and appear as a circle. Here, the propagating wave is represented by wave vector $\overrightarrow{k} = [k_x, k_y]$, and ω is the frequency. In such materials, the conductivity is uniform $\sigma_{xx} = \sigma_{yy}$. Such metasurfaces do not have directional dependence in their properties, and the waves propagate uniformly in all directions, as shown in Figure 3.2 (a). They are usually composed of symmetric meta-atoms. In anisotropic materials, the propagating vector depends on the direction of propagation. Unlike isotropic metasurfaces, anisotropic metasurfaces have a different response along different axes. This usually means $\sigma_x \neq \sigma_y$. For anisotropic materials, IFCs have the shape of a closed contour rather than a round shape; they can be an ellipse, a flattened square, or a hexagon. The anisotropy arises from the asymmetry of the meta-atoms or their asymmetrical arrangement. Such structure we will consider in the next Chapter on the example of the PC with a hexagonal lattice. Extremely anisotropic materials are a special class of anisotropic metamaterials whose properties exhibit extreme direction

dependence. One example of highly anisotropic metasurfaces is chiral metasurfaces. Their distinguishing feature is that they do not have mirror symmetry and interact differently with left- and right-handed circularly polarized light. Chiral metasurfaces typically consist of arrays of asymmetric metaatoms, such as twisted structures, or planar meta-atoms with broken mirror symmetry.

Another example of the extreme case of anisotropy is hyperbolic metasurfaces. The term "hyperbolic" is derived from the shape of its k-space topology when the IFC opens up into a hyperboloid, as indicated in Figure 3.2 (b) - (c). The magnitude of the wave vector at the IFC indicates the energy propagated in that direction. The hyperbolic shape of IFCs theoretically allows for infinitely large wave vector values. In such a surface there is a different sign of the imaginary part of the principal components of the conductivity tensors in the x and y directions, i.e., $\mathrm{Im}(\sigma_{xx})\mathrm{Im}(\sigma_{yy}) < 0$ [91]. When the imaginary part of one component of the conductivity tensor is much smaller than the other or equal to zero, the IFC opens into an almost flat shape, which causes the field to propagate in the direction of the smaller imaginary conductivity component [92]. This regime is called a self-colimation of surface waves and corresponds to the flat phase front and flat IFC (Figure 3.2 (d)) In the literature it can also be called guiding, channeling, and tunneling [91, 81].

Such metasurfaces are generated by compression of a 3D hyperbolic metamaterial [93, 94] onto a 2D surface and support hyperbolic surface waves [95, 96]. The unique shape of IFCs that characterize a hyperbolic medium defines its remarkable properties, including negative refraction [97], diffraction-free propagation [96, 91], canalization of the incoming energy [98] and many more [93]. Such phenomena find a variety of applications in various fields. They make it possible to obtain subdiffraction images [99], planar hyperlensing [100, 101], and states of increased photon density, which leads to an increase of the spontaneous emission rate [102] and for tasks such as engineering of wavefront and bending [95, 96, 100].

In visible and near-infrared spectra, the hyperbolic regime can be achieved in two-dimensional materials [103, 104], graphene-patterned structures [96, 100], plasmonic gratings [97] and metasurfaces [95]. In microwaves, hyperbolic metasurfaces are usually implemented using LC-circuits [105] and metallic patterns like in self-complementary metasurfaces [91].

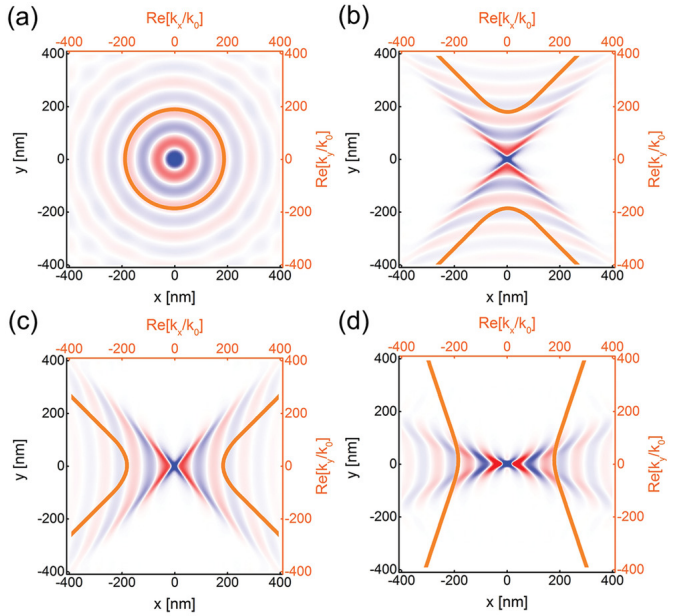

Figure 3.2 – Examples of metasurface IFCs. The color map is the vertically polarized electric field E_z excited by a dipole oriented z placed above the metasurface. The curves in the graphs are IFCs of each metasurface. a) Isotropic metasurface, $\sigma_{xx} = \sigma_{yy} = 1.5 + i20\ \mu S$. b) Hyperbolic metasurface, $\sigma_{xx} = 1.5–i20\ \mu S$, $\sigma_{yy} = 1.5 + i20\ \mu S$. c) Hyperbolic metasurface, $\sigma_{xx} = 1.5 + i20\ \mu S$, $\sigma_{yy} = 1.5–i20\ \mu S$. d) σ-near-zero metasurface, $\sigma_{xx} = 1.5 + i20\ \mu S$, $\sigma_{yy} = 1.5\ \mu S$ (Source: [92]).

3.1.4 Complementary and Self-Complementary Metasurface

Complementary metasurfaces are a type of metasurfaces that were created based on the concept of complementary electric and magnetic responses. Thus, these surfaces have complementary geometrical structures and, consequently, they have complementary electric and magnetic properties. This principle of complementarity is called the Babinet principle and arises from Maxwell's equations. According to Maxwell's equations, electric fields and magnetic fields are interrelated, and changes in one field can induce corresponding changes in the other field. Complementary structures exploit this relationship by designing materials with complementary responses to electric and magnetic fields. Complementary metasurfaces are aperture- and pach-type metasurfaces that appear as Babinet inversions of each other. Such metasurfaces have a capacitive and inductive response type, respectively. In aperture-type metasurfaces, the unit cells are composed of apertures or slots into a thin metallic film. Patch-type metasurfaces consist of metallic patches placed on a planar dielectric substrate.

Self-complementary metasurfaces are single-layer metasurfaces that remain unchanged after Babinet's inversion of itself, i.e. contain elements of both aperture- and pach-types of complementary unit cells. When aperture and patch-type unit cells are arranged as alternating stripes in anisotropic self-complementary metasurfaces, as is

shown in Figure 3.3, the imaginary part of the conductivity has the opposite sign in the direction parallel and perpendicular to these stripes. Surface waves on anisotropic self-complementary metasurfaces and their fundamental properties were previously studied in [91] and it was shown that such surfaces remain hyperbolic in all frequency ranges.

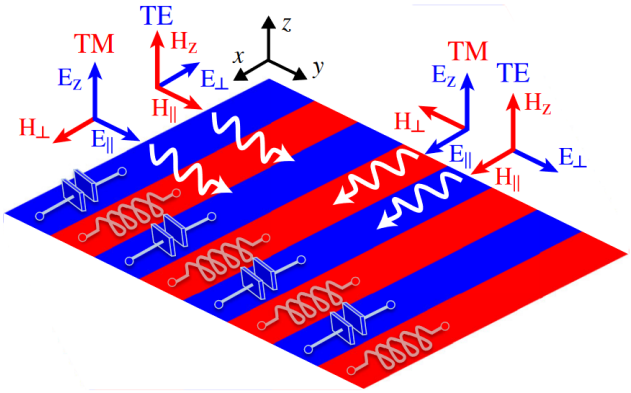

Figure 3.3 – Schematic geometry of a self-complementary metasurface constructed as an array of inductive and capacitive parallel strips. The polarization of TE and TM surface-wave modes with a parallel and orthogonal propagation direction is shown on top of the metasurface (Source: [91]).

3.1.5 Anomalous Reflection From Hyperbolic Media

An interesting phenomena can occur on the boundary of two media. The example of how the boundary problem can be described by the IFCs is shown in the Figure 3.4 (a). Drawing a straight line on the IFC corresponding to the incident wave $k_x = k_{x_{inc}}$, we can find wave vectors for the refracted $k_{x_{ref}}$ and transmitted $k_{x_{tr}}$ waves. Here we consider a paradox of the boundary between an isotropic dielectric and hyperbolic media (Fig. 3.4 (b)). In the isotropic media with closed IFCs, electromagnetic waves can propagate in all directions, whereas media with open IFCs, like hyperbolic media, have no IFCs in some directions of their k-space. It results in unusual behavior of the reflected or transmitted waves [106]. Due to the open topology of the IFC, by properly aligning the hyperbolic medium's optical axis to the interface with an isotropic dielectric, it is possible to obtain a regime in which the existence of the reflected wave is forbidden. This regime can be achieved when the asymptotes of the IFC are perpendicular to the boundary. Using the conservation of in-plane momentum it is possible to show that (for $k_x > 0$) there is no IFC branch for the reflected wave as shown in Figure 3.4 (b). If the wavevector in hyperbolic media is larger than the wavevector in an isotropic dielectric, there will also be no propagating transmitted wave. Thus, there will be a constant energy inflow due to the presence of the incident wave and no channels for its consumption (neither for dissipation nor for scattering). We call the described situation a no-reflection paradox.

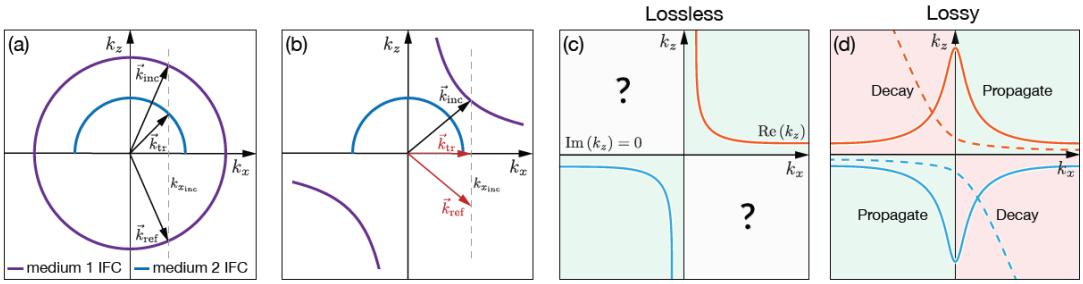

Figure 3.4 – IFCs and refraction at the interface between two media. (a) Example of the solution of a refraction problem using IFCs for two isotropic media. (b) The illustration of the no-reflection paradox, when there is no point on the hyperbolic IFC, corresponding to the reflected wave. Here is also shown that when the wavevector in the first medium is larger than the wavevector in the second medium, the transmitted wave is absent as well. In both figures (a) and (b) it is assumed that electromagnetic wave is incident from the first medium. (c), (d) - Schematic representation of IFCs for a lossless and a lossy hyperbolic medium. In the lossless case, there are two quadrants in the phase plane, in which IFC is absent, while, in the lossy case, IFC is present in all quadrants (Source: [2]).

The paradox of the absence of the reflected field was discussed in Ref. [9], and mentioned in Ref. [10]. The resolution of this paradox was formulated by our colleagues in [2]: the reflected wave is present in the system but is highly decaying as the loss parameter tends to zero. The paradox is resolved by introducing infinitesimal losses in the hyperbolic medium when we consider the problem of the boundary between a hyperbolic medium and an isotropic dielectric.

The explanation of this paradox is for the 3D hyperbolic medium rather than for a 2D surface. For this reason, we will use the permittivity tensor to characterize it, instead of the conductivity. For hyperbolic 3D media, one component of the permittivity tensor has a different sign from that of the other components. For the lossless hyperbolic medium (Figure 3.4 (b)) The permittivity tensor in the principal axes is equal to $\hat{\varepsilon} = \mathrm{diag}[\varepsilon, \varepsilon, -\varepsilon]$. If the hyperbolic medium is rotated by $\pi/4$ in such a way that the asymptotic lines of the dispersion are parallel to k_x and k_z, the relation between the wavevector components is equal to

$$k_z = -\frac{1}{2}\frac{\varepsilon}{k_x}k_0^2. \tag{3.1}$$

This equation gives us the IFCs only in two quadrants as shown in Figure 3.4 (c). As a consequence, both the reflected and transmitted waves will be absent in such a system. When we introduce isotropic losses κ to the system, the permittivity tensor of

the hyperbolic medium turns into

$$\hat{\varepsilon} = \begin{bmatrix} i\kappa & 0 & \varepsilon \\ 0 & i\kappa + \varepsilon & 0 \\ \varepsilon & 0 & i\kappa \end{bmatrix}, \tag{3.2}$$

where $\varepsilon, \kappa \in \mathbb{R}$. Here, $\kappa > 0$ corresponds to lossy media, while $\kappa < 0$ corresponds to media with gain. For such a permittivity tensor, the relation between wavevector components is given by

$$k_{z_\pm} = \frac{i}{\kappa}(k_x\varepsilon \pm \sqrt{(k_x^2 - i\kappa k_0^2)(k^2 + \varepsilon^2)}). \tag{3.3}$$

Figure 3.5 shows the real part of $k_{z_\pm}$ from Eq. (3.3) as a function of k_x for a hyperbolic medium with $\varepsilon = 1$ for different values of κ. Even for small losses, there exists a branch of the IFCs in each quadrant of the k-space. In these figures (Figures 3.5. (a)-(c)), for the same k_x upper and lower branches of IFC, which are usually associated with $k_{z_{\text{inc}}}$ and $k_{z_{\text{ref}}}$ are no longer related to $k_{z_{\text{inc}}} = -k_{z_{\text{ref}}}$ as is usually taken and the imaginary part decreases for one branch and increases for another as $\kappa \to 0$.

In the lossy media ghost modes appear at the quadrant, whereas for the lossless media, no IFC is present. These modes are concentrated at the interface, highly decaying, and are usually neglected. The counter-intuitive conclusion from this study it that that the smaller the loss, the higher the decaying rate of the ghost waves. As a consequence, all of the energy scattered into the reflected channel is absorbed near the interface.

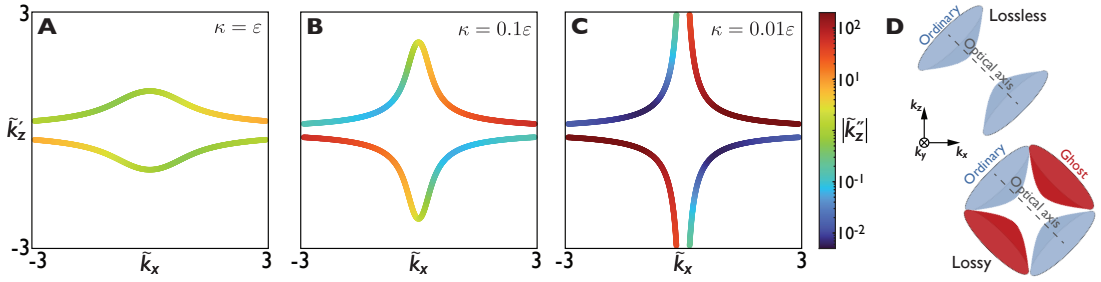

Figure 3.5 – Isofrequency contours for lossy hyperbolic media with $\varepsilon = 1$, $Re[k_z] \equiv k_z'$, $Im\,[k_z] \equiv k_z''$ and $\tilde{k}_{x,z} = k_{x,z}/k_0$ for different values of loss parameter κ, $\kappa = \varepsilon, \kappa = 0.1\varepsilon, \kappa = 0.01\varepsilon$. Colorbar encodes the modulus of the imaginary part of $\tilde{k}_z$. Panels A, B, and C show that as $\kappa \to 0$, precisely in those quadrants in which the branches of the dispersion equation are absent for the lossless hyperbolic media, the imaginary part of k_z is going to infinity, $Im(k_z) \to \pm\infty$. Panel D shows a schematical representation of the IFC for ordinary and ghost modes in lossless and lossy hyperbolic medium.

3.1.6 Near-field scanning in the Microwave range

For the experimental demonstration of this effect, we decided to use a hyperbolic self-complementary metasurface described in [91] with the 7mm unit cell period and an FR-4 substrate with relative permittivity $\varepsilon = 4.3$, loss tangent $\tan\delta = 0.025$ and thickness $h = 1$ mm. These parameters were used to obtain the hyperbolic regime at 4 GHz. The unit cell and the photo of the surface are shown in Figs. 3.6 (a) and (b). The unit cell consists of complementary aperture and pach-type parts (in the figure 3.6 (a) the metallic components are displayed in yellow and the dielectric material in white). As mentioned above, the absence of a reflected wave can be achieved when the IFC asymptotes are perpendicular to the edge of the hyperbolic metasurface. To test this, we designed two samples with different unit cell orientations relative to the metasurface edge. The samples had dimensions of 280 mm × 280 mm and contained 40 × 40 unit cells. The first'square sample' is shown in Figure 3.6 (c); the edge of the unit cells here is aligned with the edge of the whole sample. The second sample is the "rhombic" one (Fig. 3.6 d), where the unit cells are rotated by 45° relative to those of the square sample.

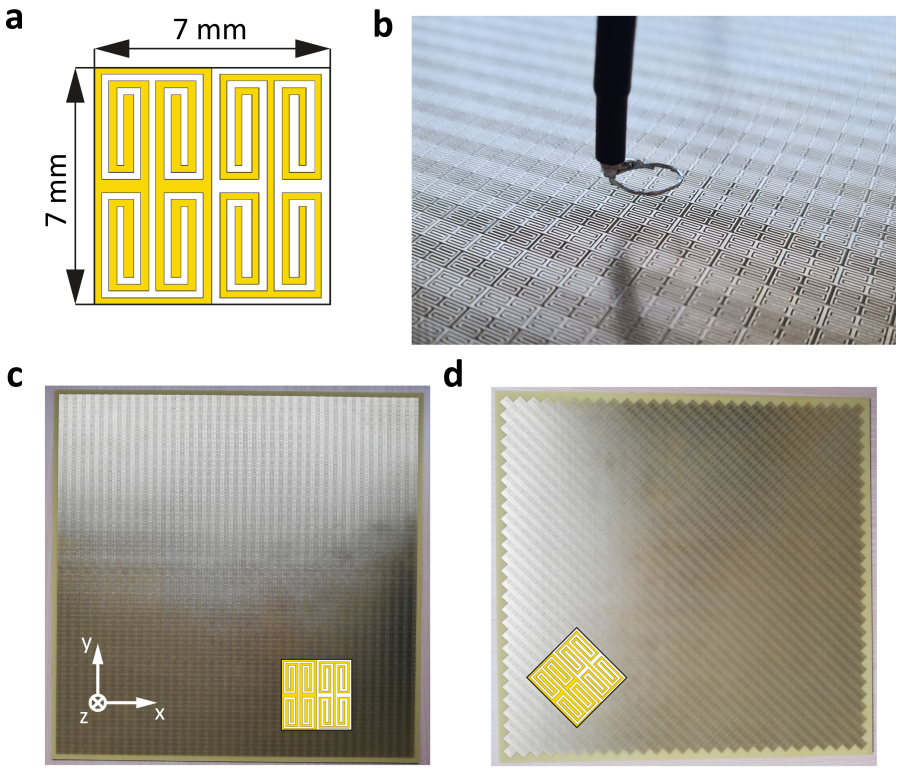

Figure 3.6 – Self-complementary hyperbolic metasurface. (a) unit cell of the metasurface. (b) photo of the excitation loop over a metasurface. (c) square and rhombic samples respectively. The insets show the orientation of the unit cell.

As a source of excitation of the surface wave, we used a vertical magnetic dipole.

The excitation loop (Fig. 3.6 b) with diameter d = 7 mm, was placed in the center of the sample at a distance of 4 mm. A similar loop was used to probe the normal component of the magnetic field H_z and placed on the other side of the sample. Both loops were connected to the two-port VNA to measure the transmission coefficient. The manufactured sample was fixed using a foam substrate and the probe was fixed on the 3D positioning system for near-field measurements (the same as in the previous chapters), parallel to the metasurface on the opposite side of the structure such that the gap between the probe and sample was equal to 7 mm.

After measuring the spatial distribution of the magnetic field, we applied the two-dimensional Fourier transform to extract the IFCs, as was done in Refs. [107, 91]. The same transform was done for the numerically calculated field maps obtained using CST Microwave Studio transient solver. Results of the numerical simulation and the experiment, for both square and rhombic structures, are presented in Fig. 3.7. On the top color maps, we show the results for the "square sample" when the asymptotes of the IFC are not perpendicular to the edge of the metasurface. It results in the presence of reflected waves and pronounced fringes due to the interference of incident and reflected waves. However, as discussed previously, when the IFC asymptotes are perpendicular to the edge of the hyperbolic metasurface, it is for the "rombic" sample (bottom colormaps) that the reflected wave becomes highly decaying. As a result, the amplitude of the reflected wave is negligible compared to the amplitude of the incident wave; therefore, the interference pattern is absent for the rhombic structure (see Figs. 3.7).

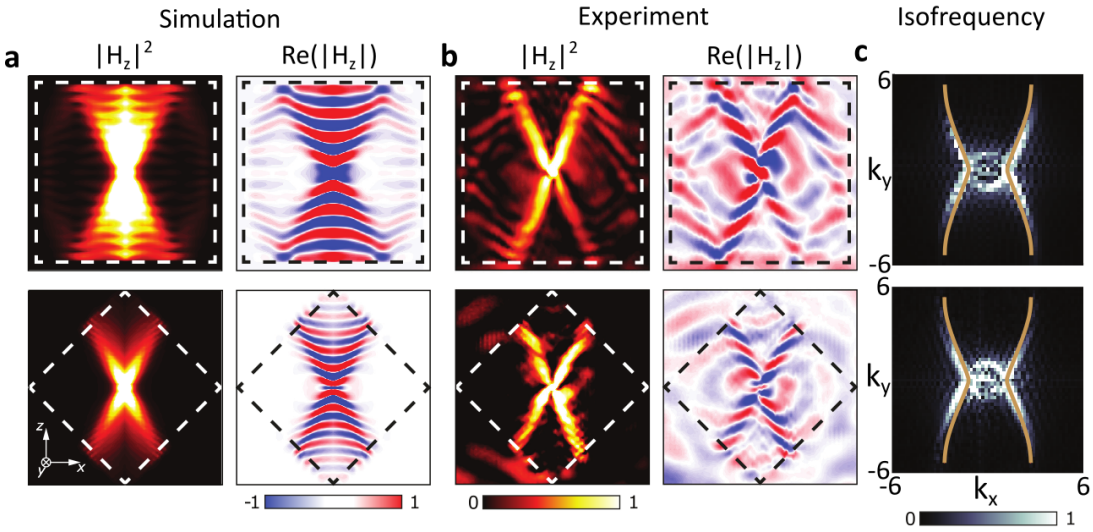

Figure 3.7 – Numerical simulation and experimental results. (a) and (b) numerical and experimental results for rhombic and square samples, respectively. modulus and real parts of H_y, respectively. Dashed rectangles represent the edge of the sample. (c) - two-dimensional Fourier transform of the experimentally measured normal component of the magnetic field, for the square and rhombic samples, respectively, showing the hyperbolic dispersion of the metasurface. Brown lines correspond to the numerically calculated IFCs using the Eigenfrequency Solver of CST Microwave Studio.

With this experimental method, we can measure an electromagnetic near field of the metasurface at the microwave range. It was shown that the presence of a pronounced reflection from the edge of a hyperbolic metasurface strongly depends on the orientation of the edge relative to the IFC asymptotes of the hyperbolic metasurface. The case in which the propagation of the refracted waves is forbidden corresponds to negligible reflection. This was observed as there was no interference between the incident and reflected waves. As stated above, this effect can be explained by rapid decay caused by losses in FR4 material and copper unit cells in the microwave range.

3.2 Energy-transfer enhanced by surface waves

3.2.1 Introduction Surface Plasmons

Surface Plasmons (SP) are waves that propagate along the interface of a conductor, usually a metal, and a dielectric, usually air or glass. They appear as an electromagnetic field at this interface, as shown in Figure 3.8 (a), and decay exponentially, as shown in Figure 3.8 (b). These surface waves occur when a magnetic field propagates parallel to the surface, called a transverse magnetic (TM) wave, or when an electric field propagates parallel to the surface, called a transverse electric (TE) wave.

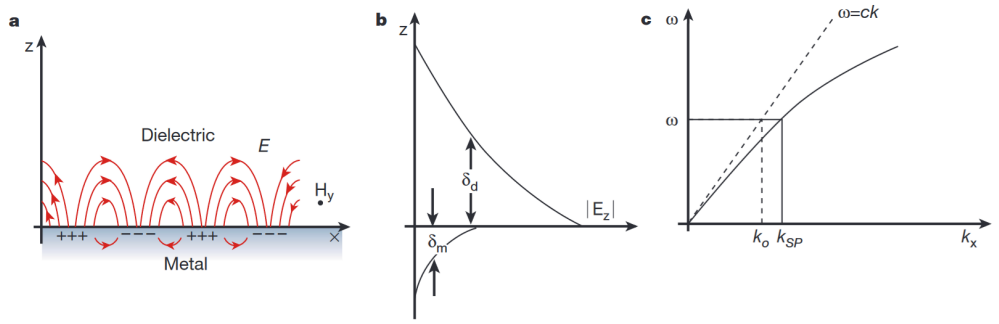

Figure 3.8 – SPs at the interface between a metal and a dielectric material (a) A transverse magnetic field in the y direction, and an electric field E normal to the metallic surface. The field component perpendicular to the surface is enhanced near the surface and decays exponentially with distance away from it (b). The field in this perpendicular direction is evanescent, reflecting the bound, non-radiative nature of SPs, and it prevents power from propagating away from the surface. In the dielectric medium above the metal the decay length of the field, δ_d is of the order of half the wavelength, whereas the decay length into the metal, δ_m is determined by the skin depth. (c) the dispersion relation of the SP (k_{SP}) (Source: [72])

The concentration of light in subwavelength structures appears from the difference between the dispersive relative permittivity of the metals ε_m and the non-dispersive relative permittivity of the surrounding dielectric media ε_d. The SP has a frequency-dependent wave vector k_{SP}

$$k_{SP} = k_0 \sqrt{\frac{\varepsilon_d \varepsilon_m}{\varepsilon_d + \varepsilon_m}} \tag{3.4}$$

When the ε_m has a sign opposite to the permittivity of the dielectric material ε_d, the SPs are possible at such an interface. This condition is satisfied for metals at optical frequencies because ε_m is complex with a negative real part. The resulting dispersive diagram is shown in Figure 3.8 (c). Pendry suggested the use of metasurface to mimic spoof plasmons in [73].

The effect of SPs on FRET rate and LDOS is still an unsolved problem in optics. For a non-dispersive medium, the theory states that the FRET rate is independent of LDOS [8, 7], but the influence of SPs on real metals is still unclear [11, 6, 12, 8, 13, 14]. The extensive theoretical work by Cortez [108] is consistent with experimental observations, and our further experiments clarify this issue.

3.2.2 Design of the metasurface that supports surface modes

For this study, we chose a Jerusalem cross-type metasurface with frequency-selective properties, known for its ability to support plasmon-like surface waves. This metasurface has already been well studied in the terahertz (THz) range [109, 110] and in the

microwave range [111]. The unit cell of this metasurface consists of miniature crossed slits cut in a metallic sheet with subwavelength periodicity in both spatial directions. The particular metasurface that we used is an aperture-type metallic metasurface, as shown in Figure 3.9 (a). This configuration exhibits an inductive response that allows propagating low-order TM surface modes. We can note that the complementary metasurface, constructed according to Babinet's principle simply by interchanging the holes and the metal, is also known as a patch-type metasurface [74]. It consists of metal strips placed on a dielectric substrate, which gives it a capacitive response and the ability to support TE surface waves. The chosen design and type of metasurface play a critical role in determining its electromagnetic characteristics and application within the study.

The manufactured sample of the metasurface is shown in Figure 3.9 (b). It was etched in a 20 μm-thick copper film placed on a dielectric FR-4 substrate with permittivity $\varepsilon_r = 4.9 + 0.1i$. The entire metsaurface sample consists of 25×25 unit cells which is 200×200 mm^2. The unit cell has dimensions $a = 8$ mm, $h = 1.9$ mm, $w_1 = 7$ mm, $w_2 = 5$ mm, and $w_3 = 0.5$ mm to operate at frequencies below 4.5 GHz, making the period of the metasurface approximately $\lambda/8.5$. As shown by the frequency-normalized dispersion diagram of the first propagating mode (Figure 3.9(c)), the dispersion curve of our metasurface (blue curve in figure 3.9 (c)) closely resembles that of a flat silver mirror in optics (orange curve).

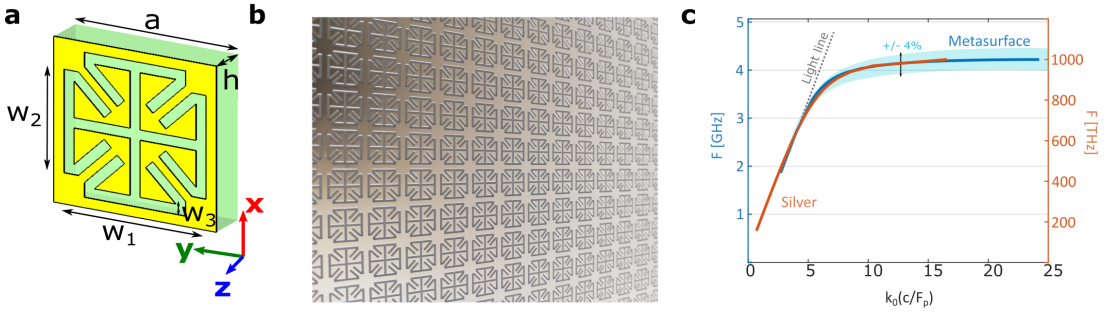

Figure 3.9 – Metasurface supporting surface waves in the microwave regime. (a) Illustration of the unit cell (a=8 mm, h=1.9 mm, $w_1 = 7$ mm, $w_2 = 5$ mm, and $w_3 = 0.5$ mm). (b) Photograph of the metasurface. (c) Dispersion curve of the first propagating surface mode of the metasurface (blue curve). The shaded region indicates the deviation range due to ±4% variations in the unit cell dimensions. The orange curve is the dispersion of the silver in the optical range. Both dispersion curves are normalized by their plasmon frequency (F_p)

The silver dispersion diagram was calculated using the formula 3.4. The complex relative permittivity of silver in the optical range ε_m is shown in Figure 3.11 (a). The metasurface can also be characterized by an effective permittivity ε_{eff} and it can be calculated numerically in CST Microwave Studio 2019 for normal incidence (Figure 3.11 (b)). For this calculation to be able to describe a metasurface with a volumetric pa-

rameter such as permittivity, we considered the metasurface as a slab of material with a finite thickness. Despite the different frequency ranges, the real part of permittivity behaves similarly for both the silver and metasurface.

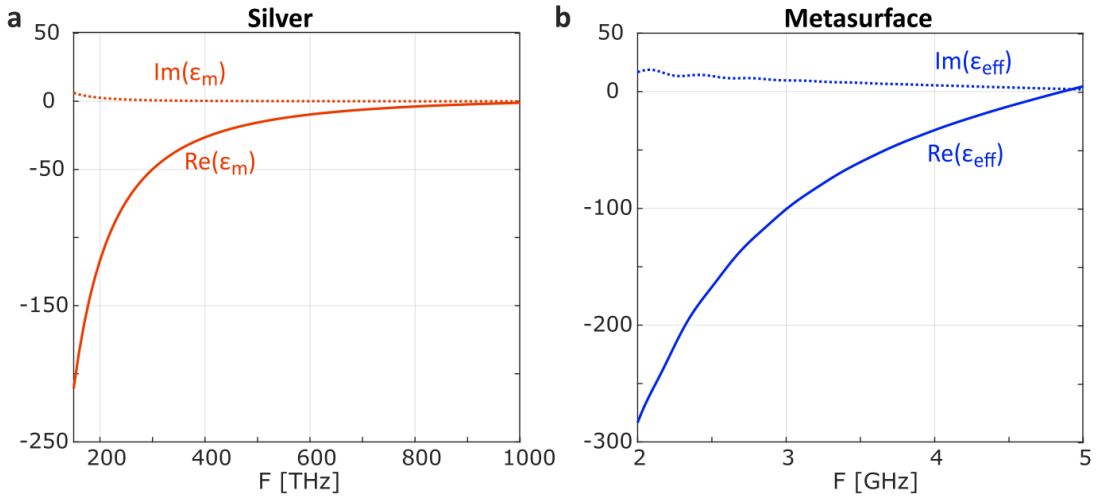

Figure 3.10 – The effective permittivity ε_{eff} of the metasurface in the microwave range for the normal incidence and the permittivity of the silver ε_m in the optical range

3.2.3 Influence of the dipole's position respective to the metasurface unit cell

As in the previous chapter, we measured the energy transfer enhancement between two dipole antennas and LDOS for a single dipole antenna. In the numerical simulations and experiments, we use dipole antennas with a total length of 10 mm, a width of 1 mm, and a gap between branches of 1 mm. In this chapter, we use antennas that are similar to the antennas we used in the Chapter 2. Here, we consider only the energy-transfer enhancement, which is the energy-transfer normalized by the reference case of the free space, and which is an analogy of the FRET rate enhancement in optics. As we have shown, this quantity is less sensitive to changes in dipole length than the energy transfer itself. We work in the frequency range between 3.5 and 4.5 GHz, so the dipole length is approximately $[\lambda/6.5, \lambda/8.5]$. The frequency of the dipole resonance remains well outside the work range and the dipoles are small enough to allow us to see the effect of the SPs on the energy transfer while still providing sufficient signal. Moreover, in the considered range of distances of $k_0 R$ between $\lambda/20$ and $\lambda/2$, dipoles of this length give a small error compared to point dipoles in the energy transfer enhancement measurements. In the measurements with the metasurface, we are interested in coupling the antenna to the surface mode. Unlike the PEC mirror, the metasurface is a resonant structure, and the design of the unit cell leads to the formation of the hot spots at distances shorter than the periods at the resonant frequency. To find these best positions for coupling the dipoles to the metasurface

mode, the electric field near the unit cell was calculated using the Eigenmode solver of CST Microwave Studio 2019 software (Figure 3.11).

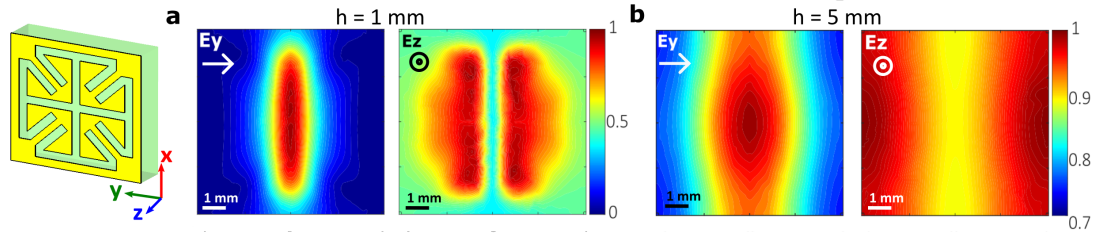

Figure 3.11 – Electric field distribution (E_y and E_z components) of the surface wave eigenmode of the metasurface at 4 GHz on top of the unit cell: for the height from the surface $h = 1$ mm and the height $h = 5$ mm.

The electric field maps were calculated for the two heights h from the edge of the unit cell: $h = 1$ mm Figure 3.11 (a) and $h = 5$ mm Figure 3.11 (b). For both cases, the maximum component E_y is in the center of the unit cell along the x-axis; this is the best position to couple with the parallel dipole. The parallel orientation of the dipole is consistent with the maximum position of the E_y component of the mode field map. For the perpendicular orientation, the minimum reachable h is 5 mm (due to the finite length of the dipole), and the coupling occurs with the component E_z. Thus, the best position for the perpendicular dipole is between the unit cells. In all further simulations and experiments, the excitation dipoles were placed in these positions depending on their orientation. In the perpendicular case, the entire dipole field is of the TM type, whereas in the parallel case, there is still a nonzero TM-polarized component that interacts with the TM-polarized surface wave supported by the metasurface at a given frequency. This means that the subperiod shift of the emitter is important for maximizing coupling.

3.2.4 Surface mode of the metasurface

To numerically test the presence of a surface wave on a metasurface, we built a numerical model of a metasurface sample of 25 × 25 unit cells (200 × 200 mm^2) using the CST Microwave Studio 2019 software. The surface wave was exited by a dipole antenna made of PEC and driven through a discrete port located in the gap between the branches. The dipoles were placed perpendicular and parallel to the surface at the best position for coupling for each orientation. To calculate the near-field, we used a transient solver, the same solver we used in the following LDOS, and energy transfer enhancement simulations.

For experimental mapping of surface mode, we use a near-field microprobe (Langer EMV-Technik MFA 01) to map the magnetic near-field. In this section, we chose to measure the magnetic field rather than the electric field because we could use a high-quality magnetic probe, which results in improved signal-to-noise ratio and image contrast in our experimental data.

As we show in the simulation below in Figure 3.12, both magnetic and electric fields exhibit equal contributions from surface modes as a result of their connection by Maxwell's equations. The main interest of our figure 3.12 is the experimental and numerical demonstration of the occurrence of surface waves in the presence of a metasurface compared to a PEC mirror. For both dipole orientations (perpendicular and parallel dipoles), the surface wave is observed as a field associated with the metasurface far from the source, which is in excellent agreement with the numerical simulations. When the metasurface is replaced by the PEC mirror, the surface wave is not detected. Together, these experimental data demonstrate that surface waves are supported by our metasurface and are very similar to surface plasmon polaritons in optics. [15].

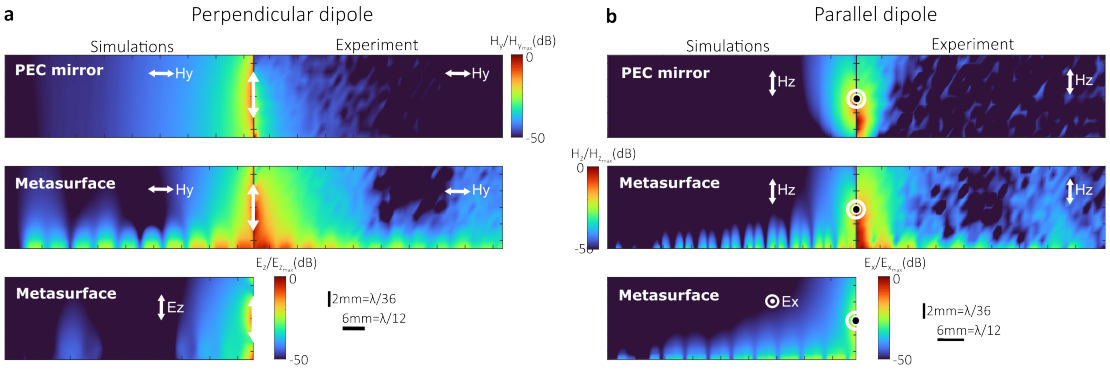

Figure 3.12 – Simulated and measured magnetic field maps and simulated electric field maps of a parallel and perpendicular dipole in the presence of a metasurface and PEC mirror, showing that surface waves are excited near the metasurface. The source dipole is located at a distance of 5 mm ($\lambda/14$) from the surface.

3.3 Energy transfer enhancement and LDOS of the dipole antennas near the metasurface

3.3.1 Measurements methods

For further measurements of energy transfer enhancement and LDOS, we used the same methods as in the previous chapter. In this chapter, the dependence of energy transfer on the dipole-dipole distance R was additionally measured. Schematic images of the experimental setups are shown in Figures 3.13 (a) and (b), and the photo of the metasurface with the dipole antenna is shown in Figure 3.13 (c). To measure energy transfer enhancement and LDOS as a function of height h, two dipoles were fixed 10 mm apart, and the center of the plane (copper plane or metasurface) was moved using a programmable 3D positioning system for near-field measurements. To evaluate the energy transfer as a function of distance R, one of the dipoles was fixed on the plane, and the second was moved using the same positioning system away

from the first dipole and parallel to the plane. The highest measured LDOS values near metasurfaces are at $F = 4.23$ GHz and $F = 3.98$ GHz for parallel and perpendicular orientations. The corresponding simulation results are $F = 4.32$ GHz and $F = 4.22$ GHz, respectively. All experiments described here are performed at these frequencies. The difference between the numerical simulation and the experiment is probably due to the uncertainty in the etching of the unit cell dimensions (the production limit corresponds to an uncertainty in the unit cell dimensions of approximately 4%). These measurements are very sensitive to the position of the dipole on the unit cell, the position of the cables, and the position of the second dipole.

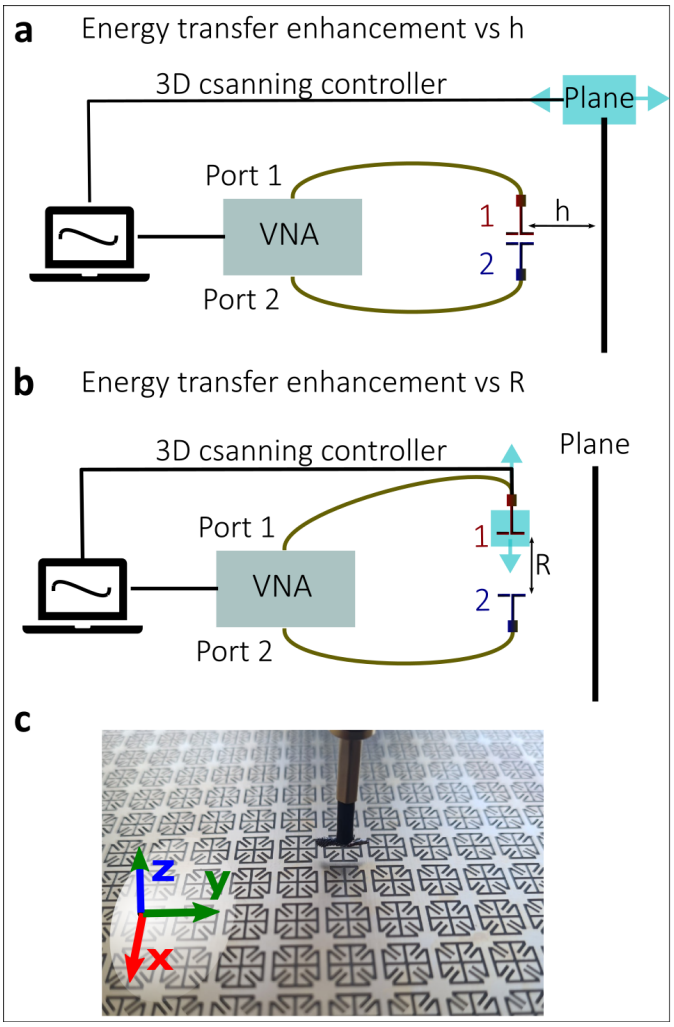

Figure 3.13 – Experimental setup for measuring energy transfer in the microwave range: (a) schematic view of the setup for energy transfer enhancement vs h measurements ; (b) schematic view of the setup for energy transfer enhancement vs R measurements ; (c) photo of the dipole antenna near the metasurface

3.3.2 LDOS near the metasurface

We begin our analysis by illustrating the evolution of LDOS with height h in Figure 3.14 (a) and (b). To ensure the reliability of our experimental data, we used measurements with the PEC mirror as a reference, the geometry which was discussed in detail in the previous chapter. Similarly to the behavior of plasmonic metals in optics [112], excitation of surface modes opens new energy decay pathways, leading to a marked increase in LDOS for parallel (Figure 3.14 (a)) and perpendicular (Figure 3.14 (b)) orientations [18, 23]. The replacement of the PEC mirror with a metasurface leads to a significant change in LDOS at short distances, where $k_0 h < 1$, especially for the parallel orientation. When we expect quenching of the LDOS near the PEC mirror, the presence of the surface wave leads to its increase. These results agree well with our numerical models and experimental results. With increasing height h, the surface mode decays exponentially, and consequently, the LDOS. Therefore, to effectively excite surface waves, the source dipole must approach the boundary at a distance not exceeding $\lambda/6$ ($k_0 h < 1$).

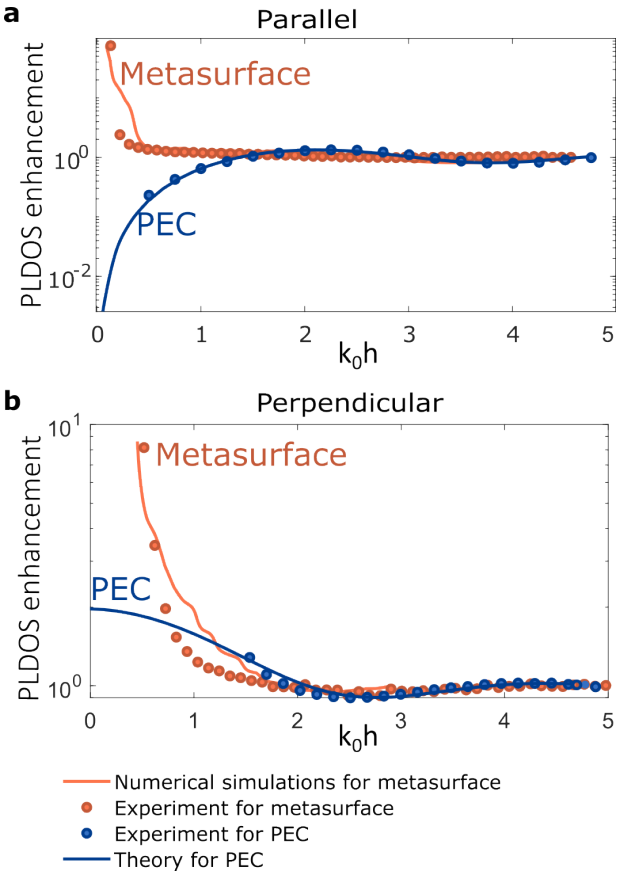

Figure 3.14 – The influence of surface-wave excitation on the LDOS detected by the dipole antenna. LDOS as a function of the height h between the plane of the dipole's center and the boundary plane for parallel (a) and perpendicular (b) dipoles orientation.

3.3.3 Energy transfer near the metasurface

Now we shift our focus to the energy transfer measurements, to illustrate how it varies with height above the surface h. For these measurements, we keep the dipole spacing constant at $R = \lambda/7$ ($k_0 R = 0.9$) moving the surface away from the dipole varying h, as shown in figure 3.13 (a). The results of the numerical simulations and measurements are shown in Figures 3.15 (a) and (b) for the parallel and perpendicular orientations. In the case of a PEC mirror, the energy transfer is suppressed in parallel orientations at short distances from the mirror, mirroring the behavior observed in LDOS. Conversely, with a perpendicular orientation, the energy transfer enhancement increases to 4, taking into account the coherent addition of the dipole and its image. For the metasurface, a noticeable increase in energy transfer enhancement exceeding 10× is achieved for both orientations at heights where $k_0 h < 1$. The presence of surface waves supported by the metasurface causes a transformation in energy transfer by introducing new coupling paths between dipoles in the near-field. This emphasizes the special role and influence of surface waves in the energy transfer process.

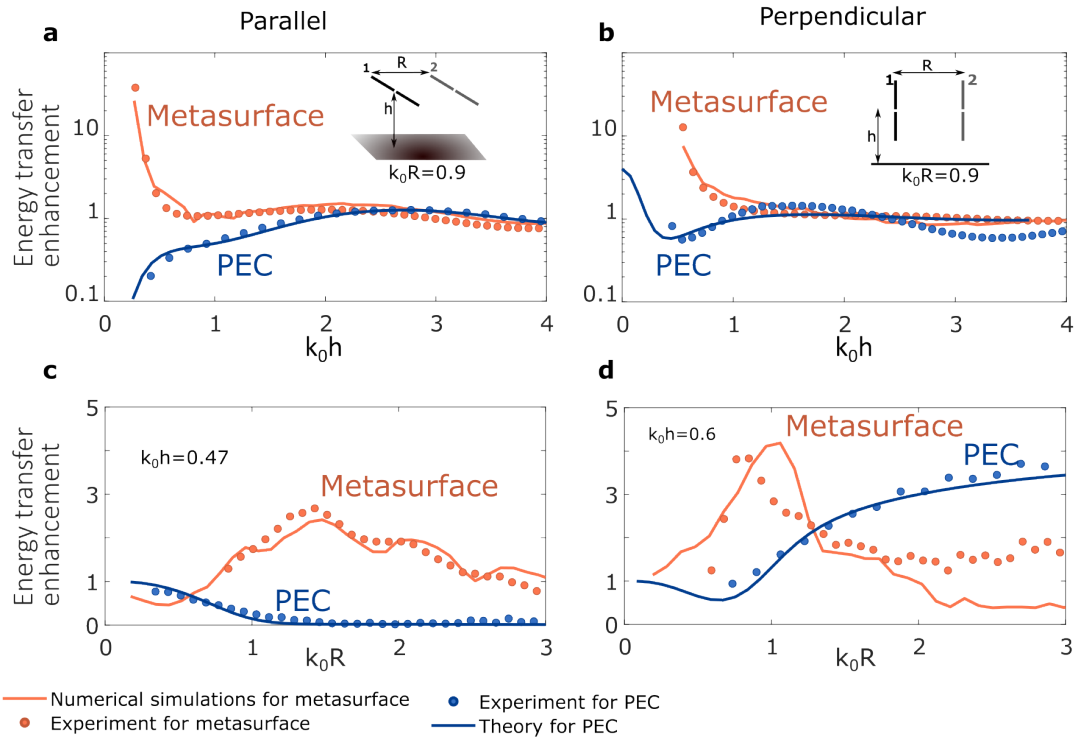

Figure 3.15 – The influence of surface-wave excitation on the near-field interaction processes between two dipoles. (a,b) energy transfer enhancement as a function of height h between the dipole antennas and the surface. The dipole-dipole distance is set at $k_0R = 0.9$, corresponding to $R = \lambda/7$. (c, d) energy transfer enhancement as a function of the distance R between the two dipoles. For (d), the height is set at $k_0h = 0.47$, while for (c) due to the finite size of the dipoles, we switch to $k_0h = 0.45$. In (a, c), both dipoles have parallel orientation to the surface and perpendicular orientation in (b, d). In all graphs, markers correspond to experimental data, while lines are numerical calculations.

In the next step, we show the evolution of energy transfer with the separation of the dipoles R, as shown in Figures 3.15 (c) and (d). Throughout all experiments, the height of the dipole above the surface is kept constant and is $h = \lambda/14$ for the parallel orientation and $h = \lambda/10$ for the perpendicular configuration. Since we used in the experiment dipole antennas with finite size, we are limited in the minimum distance to the boundary for the perpendicular orientation. In this set of measurements, the acceptor dipole moves away from the donor dipole, maintaining the same orientation and distance to the boundary, the scheme of the experimental setup is shown in Figure 3.13 (b).

In the case of a lossless PEC mirror, the enhancement of energy transfer at distances $k_0R > 2$ tends to be consistent with the radiative rate of the source donor dipole. This is especially true since at such large values of k_0R the energy transfer is mainly dominated by far-field radiative transfer. In the case of a parallel dipole placed next to

a PEC mirror, destructive interference between the dipole and its mirror image [18], leads to cancellation of the intensity emitted by the donor dipole. Consequently, the energy transfer decreases faster compared to the free space reference and the energy transfer enhancement tends to 0. On the other hand, in the perpendicular case, the dipole and its mirror image are in phase, resulting in a doubling of the generated field compared to free space. Therefore, for larger values of $k_0R > 2$, the energy transfer enhancement tends to be 4.

For both parallel and perpendicular orientations, the results obtained with the metasurface differ from those with the PEC mirror, highlighting the key role of the surface waves in mediating dipole–dipole energy transfer. The presence of surface waves and non-radiative losses leads to significant changes in the behavior of energy transfer enhancement. It is noteworthy that the energy transfer enhancement is observed in a certain region of distances between $\lambda/9$ and $\lambda/3$, corresponding to $k_0R = 0.7$ and $k_0R = 2.5$. The metasurface consists of discrete unit cells, which leads to the non-uniform field distribution along the surface, and these oscillations are detected as the acceptor moves away from the source, as can be seen by the nodes in Figure 3.12. The numerical simulations further confirm this behavior. The typical oscillation period is determined to be 0.7 or more precisely at $k_0R = 1.1, 1.8, 2.5...$ in Figure 3.15(c), which is in good agreement with the unit cell size of 8 mm. It is worth noting that the finite size of the dipoles used in our experiment leads to the averaging of the measured field over their surface, which leads to a decrease in the resolution of field fluctuations in the experimental data. However, the general trend is still clearly visible.

3.3.4 Correlation of the energy transfer enhancement with the LDOS

With data on both the LDOS and the energy transfer enhancement as a function of distance from the boundary, we can evaluate the impact of the surface wave on both compared to PEC and study the correlation between LDOS and energy transfer. To quantify this impact, we calculated the ratio of the metasurface case to the PEC case for both LDOS and energy transfer enhancement. A comparison of the energy transfer and LDOS gains achieved by using a metasurface instead of PEC is shown in Figure 3.16 for parallel (a) and perpendicular (b) antennas.

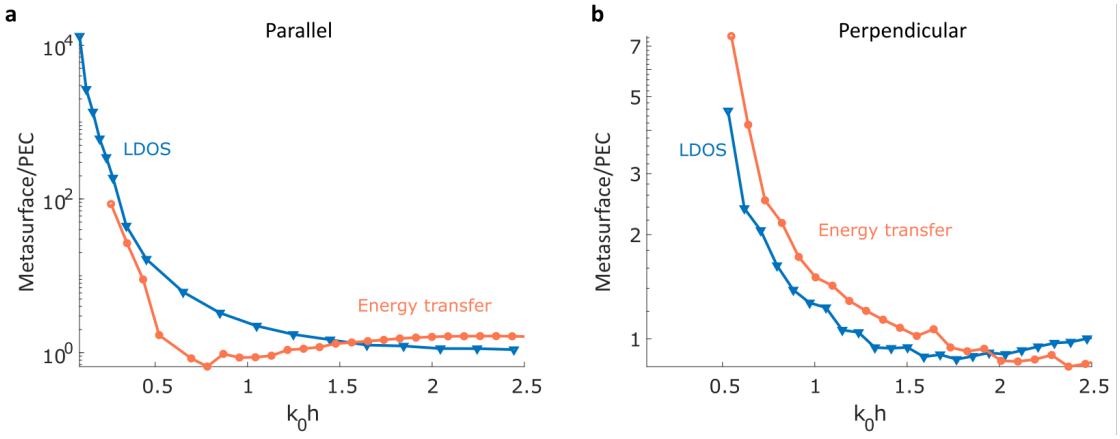

Figure 3.16 – A comparison of the gains in energy transfer and LDOS found with the metasurface to the PEC shows the spatial distribution of the surface wave impact. The dipole-dipole distance for the energy transfer enhancement corresponds to $k_0R = 0.9$ as for the results above.

An increase in both energy transfer and LDOS is observed close to the surface, which is attributed to the presence of a surface wave. It is noteworthy that for parallel antennas the surface wave has a more pronounced effect compared to the PEC mirror. This difference arises because the PEC mirror tends to reduce the levels of LDOS and energy transfer, whereas the presence of a surface wave, in contrast, leads to an increase in these two parameters. However, when k_0h is exceeded, the influence of the surface wave decreases exponentially.

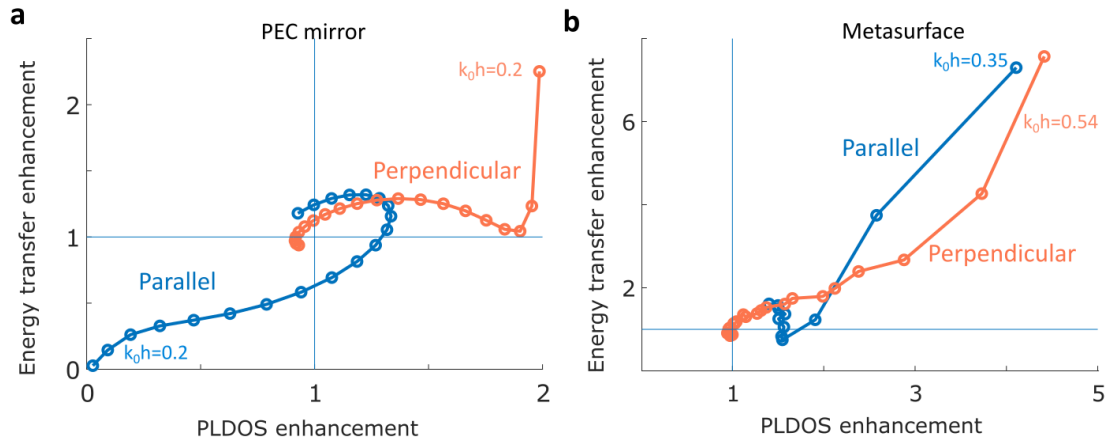

Figure 3.17 – The LDOS vs. Energy transfer enhancement diagrams for the PEC mirror (a) and for the metasurface (b). The data corresponds to the numerical results of Fig. 3.15 (a) and (b) with a dipole-dipole distance $R = \lambda/7$ and Fig. 3.14. The markers are shown for different heights k_0h to the surface. When the distance h increases, all the curves converge towards the free space (1,1) value

It is well known that LDOS depends on the imaginary part of the donor field at the source position, whereas energy transfer depends on the square modulus of the donor field at the acceptor position [20, 6]. We can study their relation for both the metasurface and the PEC mirror using the data in Figures 3.15 (a) and (b) and in Figure 3.14. In the work of [7] the relationship of the LDOS and FRET rate enhancement has already been studied for absorption-less and dispersion-less media on the example of PEC mirror at $k_0R = \lambda/100$ where the FRET rate does not show a linear correlation with the LDOS. In Figure 3.17 (a) we show the correlation of the energy transfer and LDOS near the PEC mirror, but for a larger distance k_0R than the one shown in [7]. In this example, the LDOS and FRET rate still has no linear correlation and we can see the dramatically different behavior for the parallel and perpendicular orientations.

For the metasurface, the relationship between energy transfer and LDOS has a linear trend for both dipole orientations, when the antennas are close to the surface. In this case, the surface waves play a major role in controlling both the LDOS and energy transfer in the near field. Surface waves contribute to the enhancement of the donor dipole electric field that defines the Green function, which in turn leads to an increase in both LDOS and energy transfer [15]. Consequently, an approximately linear relationship between energy transfer and LDOS appears in the case of the metasurface. This result can be extended to other geometries used in the visible regime, such as cylindrical metal apertures [12, 16, 29], plasmonic nanoparticles [26, 35, 37], and nanoantennas [28, 24, 34], where surface waves also play a key role.

In the considered intermediate range of donor-acceptor separation k_0R, the metasurface waves play a key role in energy transfer and the difference between the metasurface and PEC mirror becomes the most noticeable. However, for a smaller distance with $k_0R < 0.3$, the donor's field at the acceptor position remains essentially unchanged as compared to free space. We can notice that in Figure 3.15(c), (d) for both the metasurface and the PEC mirror, the energy transfer enhancement is around 1, which means that the energy transfer remains unchanged compared to the free space. Although the LDOS may still be affected by the presence of the surface. Our data set makes a significant contribution to resolving the long-standing debate about the relationship between energy transfer and LDOS [11, 8] by convincingly highlighting the special role and influence of surface waves on plane mirrors.

3.4 Outline

In this chapter, we have used the existing method to measure the near-field of the metasurface in the microwave range. We considered the hyperbolic metasurface to show the resolution of the no-reflection paradox on the boundary of the hyperbolic media and isotropic dielectric. We have studied numerically and experimentally how the presence of the surface wave can mediate energy transfer and LDOS. This influence of surface waves on the FRET rate has not previously been studied in detail, primarily due to experimental challenges in the optical range [11, 6, 12, 8, 13, 14]. Here, we overcome these difficulties using the analogy of the FRET rate in the mi-

crowave range. By employing dipole antennas and the microwave metasurface that can support surface waves similarly to the metals in optics, we captured the impact of the surface mode on the energy transfer between the antennas. When comparing the dispersive metasurface with the nondispersive and nonresonant PEC mirror discussed in detail in the previous chapter, we find qualitatively different effects on both energy transfer and LDOS. We have shown that the surface waves enhance the electric field at the donor dipole position and at the acceptor position defined by the Green function, which in turn leads to an increase in both the LDOS and the energy transfer. We highlight the influence of the metasurface by demonstrating a prominent linear relationship between energy transfer and LDOS when the donor and acceptor are close to the metasurface. It was shown for the near-field range (for $k_0 R$ between $\lambda/20$ and $\lambda/2$), which is the region in optics that is the most difficult to measure [16, 17]. Additionally, as was shown in the previous chapter, antennas with the length of $\lambda/7$ can be considered small at this distance range for energy transfer enhancement measurements. These results allow us to draw an analogy with the FERT rate and show its behavior near SPs of the metals in the optical range.

4 Methods of the near-field measurements in the THz range

In this chapter, we move on to the near-field measurements and the shorter wavelength in the terahertz (THz) range placed between the microwave and optical ranges. In the THz range, unlike the microwave range near-field measurements remain challenging. In this chapter, we perform near-field measurements to study a broadband terahertz emitter's emission properties near a photonic crystal (PC). Such measurements have not previously been observed experimentally at his range. We identified three distinct effects in the 0.3 to 0.5 THz range: field suppression at the quasi-TE bandgap; frequency-dependent directional radiation outside the bandgap region; and redirection of directional radiation by rotating the PC according to the orientation of the dipole. Simulations confirm that the observed behavior is consistent with the underlying band structure. Our experimental approaches advance the capabilities of terahertz spectroscopy, especially for the characterization of terahertz modes in real fabricated samples, where inherent imperfections pose modeling challenges, especially in highly dispersive frequency ranges.

Related Articles

— Kseniia Lezhennikova, Sahand Mahmoodian, Boris T. Kuhlmey, Redha Abdeddaim, Stefan Enoch, C. Martijn De Sterke, and Alessandro Tuniz. "Broadband Terahertz Near-Field Excitation and Detection of Silicon Photonic Crystal Modes". en. In: *ACS Photonics* 10.12 (2023), pp. 4447–4455. ISSN: 2330-4022, 2330-4022. DOI: 10.1021/acsphotonics.3c01312

4.1 Experimental methods in the terahertz range

4.1.1 Introduction to terahertz range

The transition from the microwave spectrum to higher frequencies in the THz range represents a change in experimental objectives. However, technologies and devices are advancing rapidly. This frequency range lies between 0.1 to 10 THz and corresponds to wavelengths of 3 mm to 30 μ m. The THz frequency range has enormous potential for a variety of applications, including biosensing [113, 114], non-destructive imaging [115], spectroscopy [116], space communications [117] and telecommunications[118]. In particular, recent years have seen a noticeable interest in 6G telecommunications networks that promise terabit/s data transfer speeds[119]. These networks are critical to supporting new technologies such as connected vehicles, augmented and virtual reality, and artificial intelligence systems [120]. Consequently, significant efforts have been devoted to developing more efficient, compact, and reliable interconnection solutions in the terahertz range [121, 122].

For communications, terahertz radiation acts as an intermediary, organically connecting the fields of optics and microwaves. It combines the strengths of both infrared waves, with characteristics such as high directivity and increased bandwidth, and microwaves, providing reduced diffraction. This dual advantage makes terahertz radiation a promising field for innovative communications technologies. However, practical implementation highly depends on atmospheric conditions [123], water and steam absorption [124], signal interference [125], long-range path loss in free space [126] and precision matching requirements between source and recipient [127]. In response to these challenges, new solutions have been developed in the form of waveguide-based terahertz communications systems, also called wired terahertz communications. Examples of such platforms include PC [128], topological [129], and suspended waveguides [130]. Metasurfaces and PC have proven to be particularly attractive solutions at higher frequencies in the THz range [131]. Their chip-based design allows the manipulation of millimeter waves, paving the way for high-speed technologies critical to potential 6G wireless applications [131].

The rise in popularity of THz devices has led to the emergence of a variety of passive components, such as directional couplers, splitters [132], and frequency multiplexers [133, 134]. Ideally, these components should occupy minimal space, making them optimal for integration with near-field communication devices. Float-zone silicon is the material of choice for short-distance applications [135], known for its extremely low loss in the THz range. Such silicon crystals have an extremely high level of purity and low impurity levels. This makes Float-zone silicon ideal for semiconductor devices, solar cells, and other high-tech applications where purity and stability are critical. This material with a refractive index of 3.42, can improve the performance and reliability of electronic devices and is compatible with established deep etch fabrication processes [136]. The realization of beam steering often requires specially designed waveguide configurations. These configurations may include leaky-wave structures [137] or coupled metal wires [134], as well as special defects in PCs [133] and metasurfaces

[138, 139]. However, it is widely known that bulk PCs [140] and metasurfaces [107] have complex band structures and are capable of supporting self-guided wave propagation or directional emission at certain frequencies even without defects. These effects occur depending on whether the input signal is a collimated beam or a point dipole [83, 140]. Although self-guided wave propagation or directional emission has been known for more than two decades, direct measurements have been made mainly at microwave and near-infrared frequencies [141, 142]. Directional radiation from a dipole antenna placed directly in the near field of the PC or metasurface has been observed in the microwave range [143, 144, 107, 91, 145] with a maximum frequency of 40 GHz in PCs [86], mainly due to experimental problems in other spectral areas. Terahertz devices typically use far-field techniques, which provide limited information about their internal workings. With the growing set of chip-based functionalities, there is a need for new characterization methods. These methods can help reveal nuanced effects associated with the structural features of the device.

4.1.2 Photonic crystals

As mentioned in Chapter 3, PCs are periodic structures similar to metamaterials, but they use the diffraction of electromagnetic waves to control the electromagnetic field. PCs are usually defined as structures that have a photonic bandgap. The photonic bandgap refers to the range of frequencies in which the propagation of electromagnetic waves through a periodic structure is prohibited or greatly suppressed.

Another property of PC is self-collimation when an electromagnetic wave propagates without diffraction and dispersion over relatively long distances. Self-collimating waves do not spread when propagating in a PC. This can be realized when the IFCs of the PC have flat areas and all wave vectors end on that line. It prohibits beam spreading and concentrates power flow in one direction. Typically the flat region can only occur at very limited beam orientations relative to the crystal lattice and with a limited beam width. For some frequencies, the form of the IFC mimics the form of the first Brillouin zone of the crystal, as shown in Figure 4.1 for a square and hexagonal lattice [146]. With changing frequency, the anisotropy of a PC changes dramatically, and its iso-frequency contours evolve from red contours (Figure 4.1) to black and then to blue. An iso-frequency contour forms an almost perfect square or hexagon at some frequencies, where the flat iso-frequency contours occur.

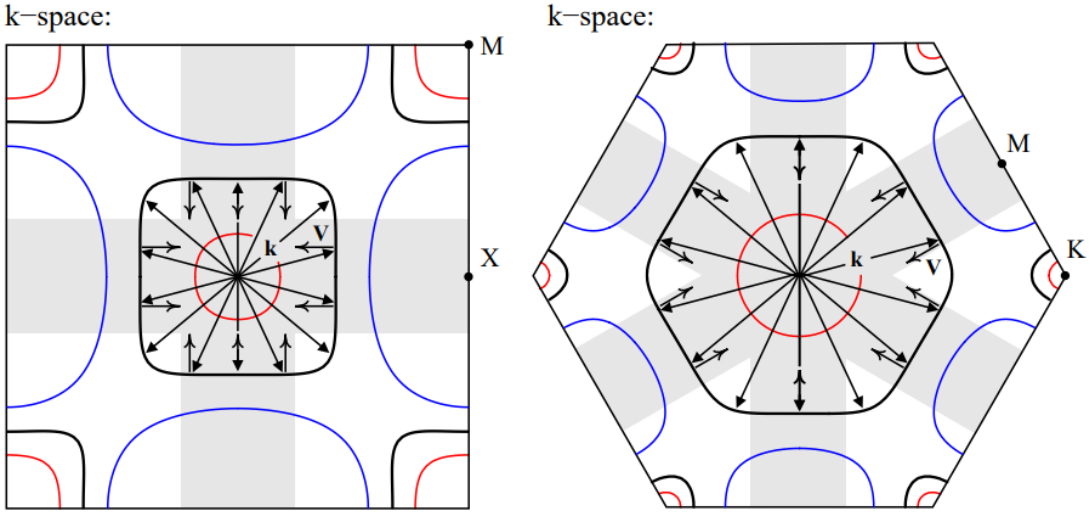

Figure 4.1 – Convex (red), concave (blue) and flat (black) iso-frequency contours. Iso-frequency contours on the left (right) panel correspond to the second band of a two-dimensional square (triangular) lattice PC made of dielectric rods in free space. The wave vectors resulting in the Bloch eigenwaves with the group velocity pointing to the direction normal to the Brillouin zone boundary are depicted with arrows (Source: [146])

In this Chapter, we consider a PC made with silicon. The PC consists of a hexagonal lattice of subwavelength diameter holes, as we show in Figures 4.2 (a) and (b). Figure 4.2(b) shows a micrograph of the PC, formed by hexagonal arranged air holes in the silicon slab and manufactured using deep etching [136]. The thickness of the slab is 250 μm, the radius of the hole is $r = 72\ \mu m$, and the pitch from center to center is $a = 240\ \mu m$. The size of the PC sample is more than 2 cm in diameter, far beyond the work wavelength. The PC band structure, calculated using the plane-wave expansion method [147], is shown in Fig. 4.2(c): as expected [148], this structure has two quasi-TE band gaps at ~ 0.35 THz and ~ 0.5 THz, which should suppress the dipole emission. Furthermore, close to the band edge, we expect directed emission that subtly depends on the relative orientation of the dipole to the PC lattice [140]. The emission of a broadband terahertz near-field x-polarized point dipole near the surface of a PC interacts with the Bloch modes of a PC sample. The dipole antenna is shown in Figures 4.2 (a) and (b) with a red arrow. The resulting emission highly depends on the frequency as a result of the underlying band structure. At frequency f_1, corresponding to the band gap in the band diagram, dipole radiation in the PC is suppressed. At the second frequency f_2, the dipole radiates predominantly in certain directions, leading to local field concentration. At the neighboring frequency f_3 the direction of radiation changes.

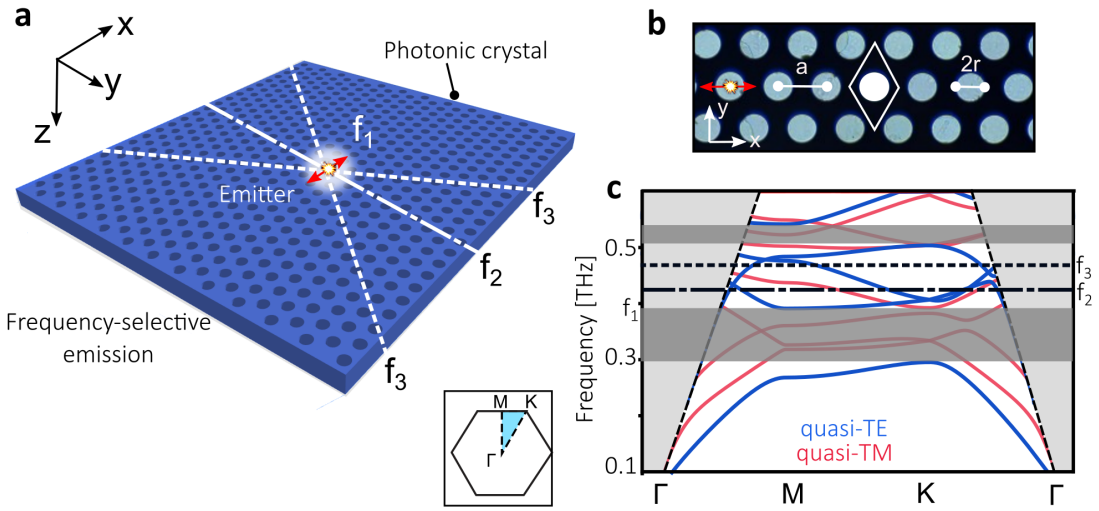

Figure 4.2 – Silicon PC with hexagonal periodic lattice. (a) The emission of the x-polarized point dipole near the surface of a PC and the emitter is placed at the center of the sample. The direction of the emission is highly dependent on the frequency: f_1 corresponds to the suppression of the emission and redirection of the emission at frequencies f_2 and f_3 which are shown with white dashed lines (b) PC micrograph. Black: silicon; white: air; period: $a = 240$ μm; hole radius: $r = 72$ μm. The unit cell is highlighted in white, the emitter dipole direction is shown by red arrows. (d) Calculated PC band structure. Grey-shaded regions highlight the first and second quasi-TE band gaps, respectively, and the dashed black lines highlight the first and second frequencies of the directional emission in (a). The first Brillouin zone is shown in the inset.

4.1.3 Setup for THz measurements

We set up our experiment using a commercially available THz Time Domain Spectroscopy (THz-TDS) System, specifically the Menlo TERAK15 model. This system works by pumping photoconductive antennas (Protemics [149]) with pulses of near-infrared light to generate THz radiation. These light pulses, with a pulse width of 90 fs and a wavelength of 1560 nm, are converted to 780 nm using a second harmonic generation (SHG) module. This conversion is necessary to stimulate the generation of terahertz photocurrent in low-temperature GaAs material.

The full schematic view of the experimental setup is shown in Figure 4.3(a) together with a photo of the emitter and detector antenna near the PC and a detailed image of the antenna (Figures 4.3 (b) and (c)). The fixed x-oriented dipole terahertz emitter, highlighted in red in Figure 4.3(a), was placed near one side of the PC. On the opposite side of the sample, there is another photoconductive antenna module, identical to the first one, mounted on a movable terahertz detector. This module acts as a detector (highlighted in blue in Figure 4.3(a)) and is placed on a moving platform to spatially scan the near field and sample the resulting field as a time delay function at each

position. The movement of the near-field scanning stage and the operation of the Menlo system are controlled by an application written through the Design App in Matlab 2022.

A similar setup has recently been used in studies on terahertz range, to measure the terahertz local density of states on metal and dielectric surfaces, study the symmetry protection properties of bound states in the continuum, and study other topological near-field effects [150]. However, a notable difference in our approach is that we placed the emitter and detector on opposite sides of the sample, unlike previous studies where both the emitter and detector were placed on the same side [151]. This difference has two significant advantages: first, it allows us to scan the entire surface of the sample since we are not limited to areas far from the bulky emitter antenna. Secondly, by recording the damped field of plate modes excited by the emitter itself, our setup excludes the possibility of measuring the direct contribution of the radiated field mediated by surface waves of plate modes. Although a similar approach has been described in the microwave range, for example, in experiments on the characterization of hyperbolic media [91], topological effects [152], and synthetic frequencies [153] where sources and detectors are macroscopic, but has not been shown to the best of our knowledge at THz frequencies.

Figure 4.2 (b) shows a photograph of the experimental setup, which is a modified terahertz time-domain spectroscopy system [154]. The electric field is polarized in x, using the sample orientation and reference frame shown in Fig. 4.3. We estimate the distance between the sample and the emitter/detector to be $\sim 200\,\mu$ m, reducing the risk of sample and antenna damage during such large-area scans.

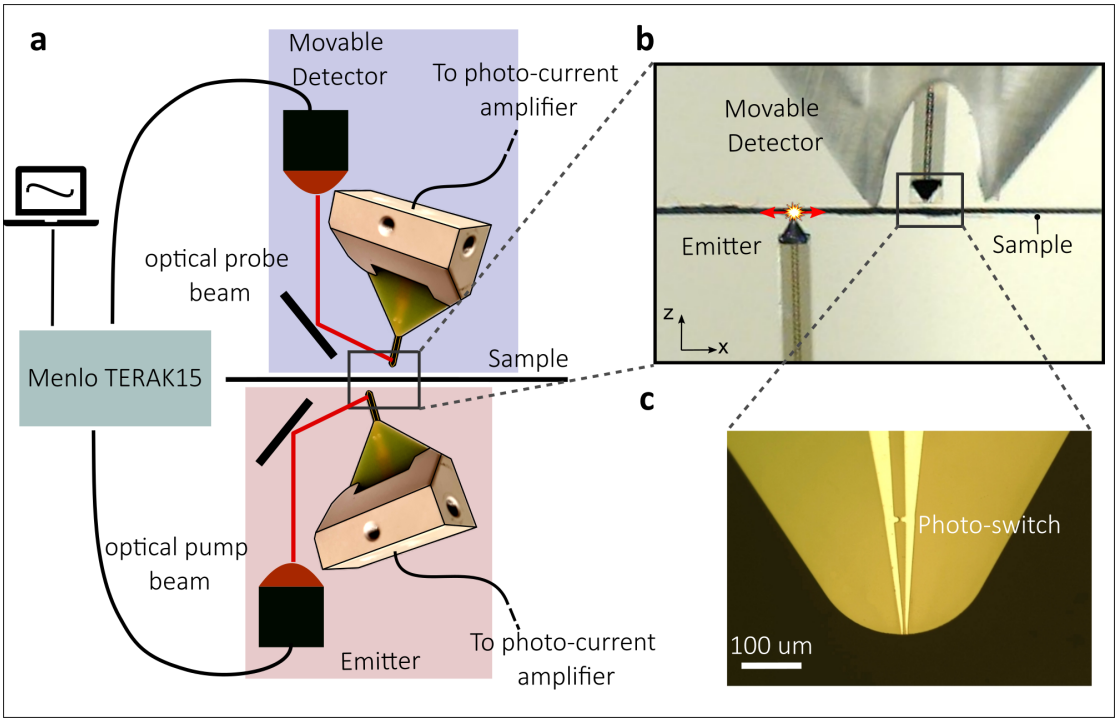

Figure 4.3 – Experimental setup. (a) Schematic representation of the experiment; (b) Photograph of the fixed x-oriented terahertz dipole emitter (red arrows) and moveable terahertz detector placed on either side of the PC; (c) Detailed image of the antenna tip.

Then we performed a reference scan when the PC was absent to make sure that the measured field distributions corresponded to the near-field of the x-polarized electric point dipole. A thorough 2D scan was realized by moving the detector along the surface parallel to the PC, each step was 100 μm and the window size was 8 × 8 mm in each measurement run. This scanning technique allows us to study the near field in detail, capturing both its spatial and temporal aspects. We then analyze the temporal response at each position and, using a fast Fourier transform, extract spectral information. With this method, we achieve a spectral resolution of 0.005 THz, providing detailed field amplitude and phase data. The temporal signal measured with the detector and the calculated spectra are shown in Figure 4.4 (a). The resulting field maps of the electric field $|E_x^0|$ and its imaginary part imag(E_x^0) are shown in Figure 4.4 (b) at 0.265 THz and Figure 4.4 (c) at 0.495 THz. For the following measurements, we placed the PC sample between the emitter and the detector as it is shown in figures 4.3 (a) and (b).

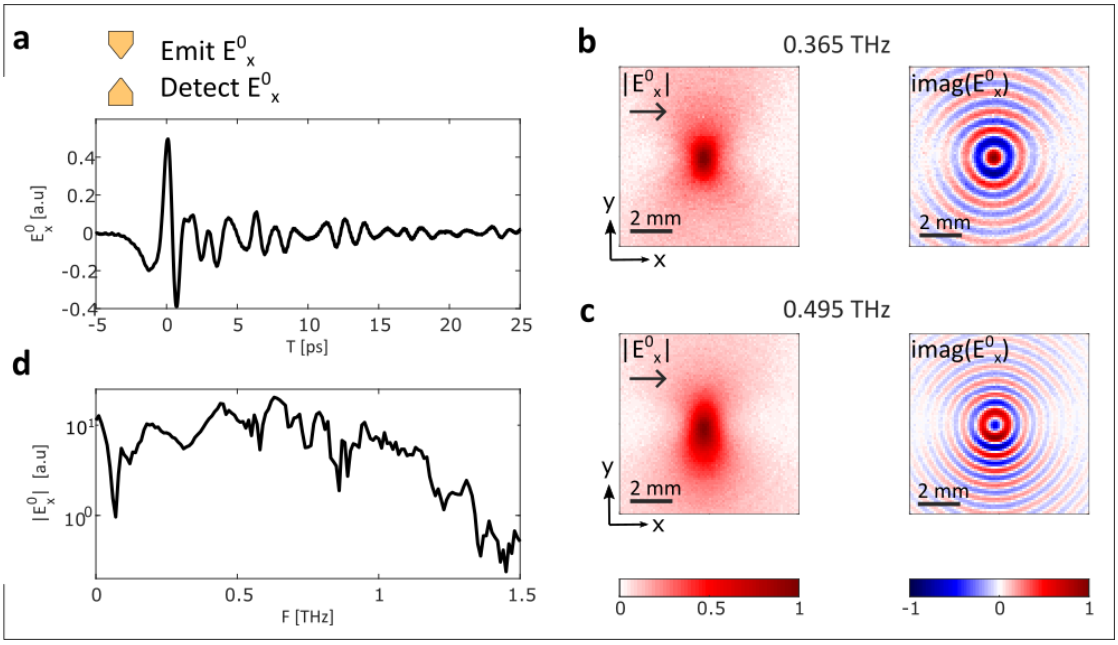

Figure 4.4 – Signal, detected by the detector placed near the emitter in the free space with the presence of only emitter. (a) temporal response when the detector is placed right on top of the emitter; (b) associated signal in the frequency domain, obtained by using Fast Fourier Transforms; (b) 2D Measurements of the near electric field $|E_x^0|$ and its imaginary part imag(E_x^0) at 0.365 THz; (c) An electric field $|E_x^0|$ and it's imaginary part imag(E_x^0) at 0.495 THz; These free-space measurements are used as a reference case in the following experiments

4.2 Broadband terahertz near-field excitation and detection of silicon PC modes

4.2.1 Emission Suppression at the TE Bandgap

We start by looking at the TE band gap, highlighted by the gray areas in Figure 4.2(c). In Figure 4.5(a), the left field map displays the measured x amplitude of the polarized electric field $|E_x|$ detected at 0.365 THz. The emitter's position on the opposite side of the PC corresponds to the central bright red area. In contrast, no directional emission or diffraction is observed elsewhere in the color map, nor is the usual emission shape of the x polarized electric dipole shown in figure 4.4 (b). To confirm this observation, compare this case with the electric field in the reference case when the PC is removed and the emitter and detector are placed in free space, leaving all other experimental conditions unchanged, denoted as $|E_x^0|$. In Figure 4.5(a), the field map on the right shows the relationship of these two cases $|E_x|/|E_x^0|$. We display this amplitude ratio in the color scale chosen so that blue and red represent values below and above unity,

respectively. The central region of the color map remains white, indicating that directly below the emitter the field amplitude does not change significantly ($|E_x|/|E_x^0| = 1$). Overall, the calculated ratio indicates suppression of emission in the vertical direction since there is no emission in the y direction as expected for an x-polarized electric dipole shown in Figure 4.4.

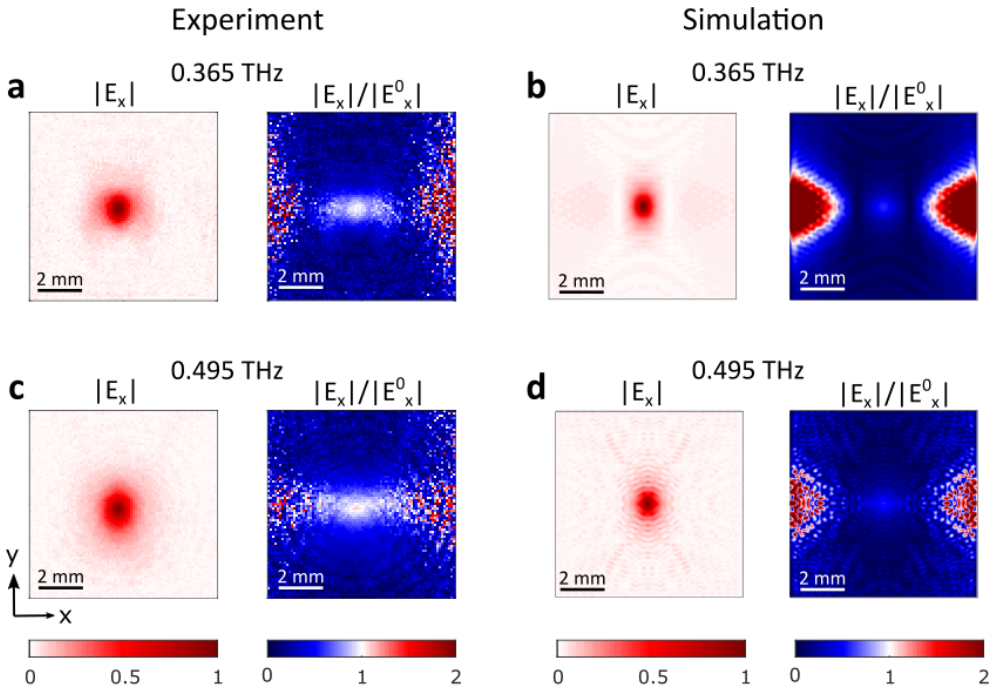

Figure 4.5 – Dipole emission suppression within the two band gaps. (a) Measured x-component of the electric field magnitude $|E_x|$ near the surface of the PC for an x-polarized emitter, at 0.365 THz (left) and the ratio $|E_x|/|E_x^0|$ (right), revealing suppression of dipole emission. (b) Corresponding FDTD numerical simulations. (c) and (d) respectively show the corresponding experiment and simulation at 0.495 THz within the second band gap. All window sizes are 8 mm × 8 mm.

A comparison with corresponding finite difference time domain (FDTD) simulations conducted in CST Microwave Studio is shown in Fig. 4.5(b). A PC was modeled in the form of a 250-μm-thick slab consisting of a dielectric material with a refractive index $n = 3.42$ and modeled in the frequency range 0.3–0.5 THz, simulating the properties of our sample [135]. The PC had a hexagonal lattice of cylindrical holes with diameters and period that corresponded to the specifications of our sample. The entire slab area had dimensions of 1× 1 cm and open boundary conditions were used in all directions. The x polarized electric dipole source was located at a distance $h_e = 200\mu$m above the PC and in the center of the slab area to provide a fair comparison with the experiments. The polarized electric field x was probed at a distance $h_d = 200\mu$m on the opposite side of the PC. The corresponding E_x^0 was obtained by running the same simulation

setup with a PC removed. A good agreement was observed between the experiment and simulation, confirming the suppression of dipole emission in the y direction due to the presence of the TE bandgap. In both experiments and simulations, when calculating the ratio with free space, red spots appeared in the x direction. These spots appear due to the absence of radiation in this direction from the x-polarized dipole in free space. Conversely, the suppressed emission near the PC was more evenly distributed around the source, resulting in the enhancement regions in the ratio colormap due to division by a smaller number.

We used the wide operating frequency range of our THz probe to study the second TE bandgap and show the suppression of quasi-TE modes at 0.495 THz. Figures4.5(c) and (d) show experimental and simulated results at this frequency, obtained under the same conditions as for the first band gap. All frames show emission suppression and remarkable agreement between experiment and numerical simulation. These results highlight the possibility of achieving similar emission profiles in different frequency ranges using the same sample.

4.2.2 Directed emission and field concentration

Continuing our investigation, we now study the emission profile of two frequencies between the two quasi-TE bandgaps of the PC considered in the previous section. In figure 4.2 these frequencies are designated as f_2 and f_3 and, according to the simulations, are equal to 0.43 and 0.45 THz. Due to the complex band structure of PC, directional emission [140] is supported at these frequencies, usually limited to a narrow band. This highlights the importance of accurate post-fabrication experimental measurements to verify the absence of defects or inaccuracies introduced during the manufacturing process, ensuring the integrity of the final device assembly. The wide bandwidth of the THz source we use allows us to scan all frequencies in this range, making it easier to identify the frequencies at which directional emission occurs.

Figure 4.6 shows the results of experiments and simulations carried out under the same conditions as discussed in the previous section but at frequencies f_2 and f_3. In Figure 4.6 (a), the left field map shows the measured x-polarized electric field amplitude $|E_x|$ exited by the x-polarized electric dipole at 0.445 THz. The orientation of the PC unit cell is depicted in the inset in the upper left corner of the color map. On the right color map, we plot the ratio of the measured electric field $|E_x|$ and the field measured in free space $|E_x^0|$ with the PC removed (reference case). These measurements reveal a directional emission along the y coordinate and weak radiation in two diagonal regions. This ratio with the reference case indicates that the field in these directions is enhanced more than twice and suppressed in the other directions ($|E_x|/|E_x^0| < 1$).

Figure 4.6 (b) shows the corresponding FDTD simulations, showing good agreement with the measurements. However, the simulation frequency is shifted to 0.43 THz, which is deviated by 0.015 THz from the measured frequency. This difference can be explained by the extreme sensitivity of these effects to minor deviations of the sample from the ideal design, such as manufacturing defects, differences in hole size, pitch,

plate thickness, and refractive index.

To interpret the observed behavior, the calculated corresponding IFCs for the quasi-TE (red) and quasi-TM (blue) modes are shown in Fig. 4.6 (c). A horizontally polarized dipole excites quasi-TE Bloch modes with almost flat contours close to the light line at the point $(k_x/k_0, k_y/k_0) \sim (0, \pm 1)$, which corresponds to vertical radiation. In addition, diagonal quasi-TE modes are excited, although weaker, near the light line $(k_x/k_0, k_y/k_0) \sim (\pm\sqrt{3}/2, \pm 1/2)$, due to less overlap between the point dipole field pattern and the diagonally directed Bloch modes.

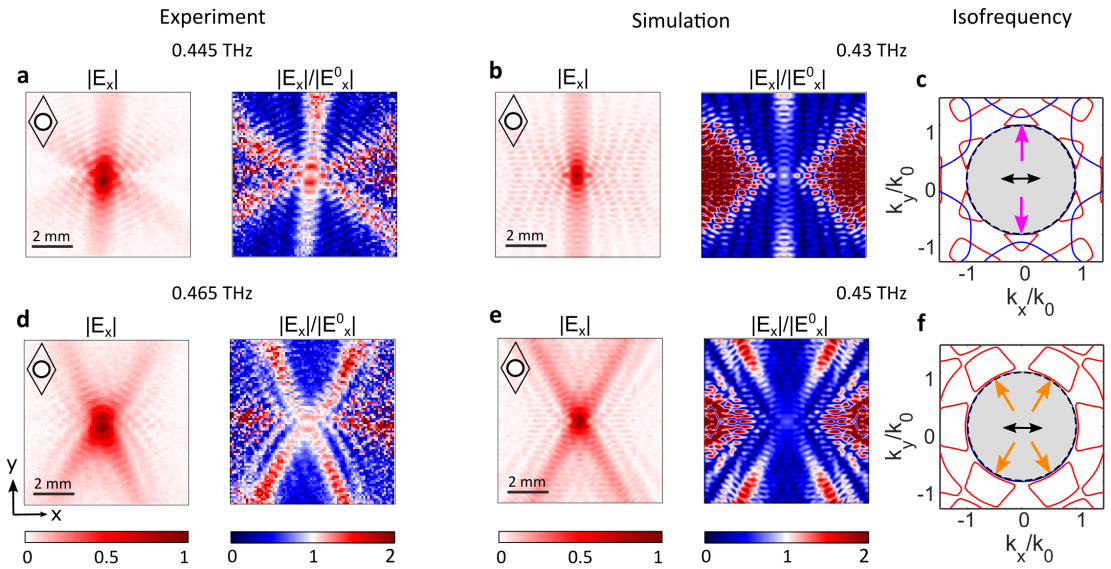

Figure 4.6 – Directed emission of the x-polarized dipole. The PC and dipole are oriented as in Fig. 4.3 (b). (a) The measured x component of the electric field magnitude $|E_x|$ for a x polarized emitter at 0.445 THz. (b) the ratio with the reference case of the free-space $|E_x|/|E_x^0|$. (b) Shows the corresponding FDTD numerical simulations. (c) Corresponding IFC for quasi-TE (red) and quasi-TM (blue) modes. The black arrow corresponds to dipole orientation, which preferentially excites the quasi-TE Bloch modes that are close to the light line and propagated perpendicular to it (purple arrows). (d) Show the corresponding experiment at 0.465 THz and simulation (e) at 0.45 THz, and (f) IFC. The Bloch modes close to the light line are excited by the dipole that lies on the diagonal axes, as observed in both experiment and simulation. The window sizes for all field maps are 8 mm × 8 mm. All the field maps are normalized by the maximum of $|E_x|$.

Moving to a slightly higher frequency f_3 at 0.465 THz, as shown in Fig. 4.6(d), we observe radiation along two diagonal axes, now forming an X-shaped radiation pattern. At this frequency, the hexagonal radiation pattern is rotated by $\pi/6$ compared to the case shown in Fig. 4.6(a). The corresponding ratio with the reference case (right colormap) shows the directional emission and field concentration in the diagonal

direction, highlighted in red areas. The corresponding FDTD simulations agree well with the experiments, although they are shifted from 0.015 to 0.45 THz, as shown in Fig. 4.6(e). The corresponding calculated IFC shown in Fig. 4.6 (f) now indicates the presence of only quasi-TE Bloch modes at this frequency, indicating a band gap for the TM modes. The IFC close to the light line follow the directional emission of the electric field and are rotated by $\pi/6$ compared to those shown in Fig. 4.6(c), highlighted by orange arrows pointing to $(k_x/k_0, k_y/k_0) \sim (\pm 1/2, \pm\sqrt{3}/2)$. In this case, the overlap between the x polarized dipole and quasi-TE Bloch modes at $(k_x/k_0, k_y/k_0) \sim (\pm 1, 0)$ is equal to zero, leading to the absence of field emission along x.

The calculated IFCs can be compared with the two-dimensional Fourier transform of the resulting field maps. In Figure 4.7 we present the imaginary part of the electric field and the corresponding two-dimensional Fourier transform for both experimental and simulated data for frequencies f_2 and f_3. The highlighted areas near the light line indicate where we expect excited modes to be present. However, due to non-uniform excitation of the x polarized dipole in x and y directions, we cannot excite modes in the y direction. In addition, at such distances between the antennas and the PC, it is impossible to detect modes distant from the light line. We address these issues one by one in additional experiments and simulations.

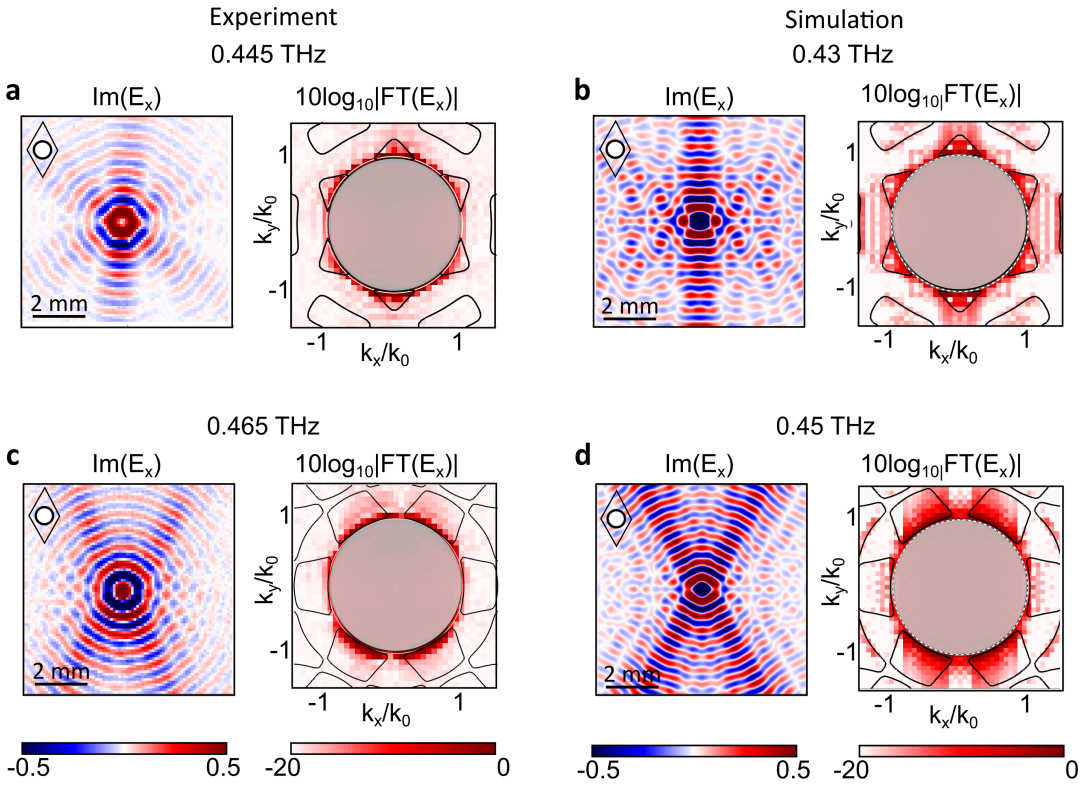

Figure 4.7 – Two-dimensional Fourier transform of the experimentally measured and simulated electric field E_x (a) Measurements of the transmitted electric field $Im(E_x)$ of a x polarized electric dipole (left), the associated amplitude of the 2D Fourier transform of the complex field (right) at 0.445 THz and in a dB scale, superimposed with simulated TE IFCs. Its regions of maximum intensity overlap with parts of the IFCs that are close to the light line. (b) The corresponding numerical simulations at 0.43 THz. Dipole excitation and field detection are at 200 μm from the edge of the membrane. The x-polarized dipole in b) excites only a subset of the quasi-TE modes shown in d). The data set in (a) and (b) is the same as in Figure 4.2.

4.2.3 Impact of the emitter position on the emission

At both frequencies considered, the IFCs have a hexagonal pattern following the geometry of the unit cells, offering six directions of field propagation. However, the x-polarized electric dipole emits a field only in the y direction and cannot excite modes in the x direction. Figure 4.8(a) (left) depicts the measured x polarized electric field amplitude E_x detected at 0.445 THz, but the PC cell is rotated by $\pi/6$ relative to Fig. 4.6, as shown in the diagram in the upper left corner of the field map of Fig. 4.8. In this configuration, in contrast to the results shown in Fig. 4.6, an X-shaped radiation pattern is observed at the lower frequency, consistent with the simulation at 0.43 THz shown in Fig. 4.8(b). This result arises from the associated rotation of the IFCs, as

shown in Fig. 4.8 (c). Consequently, at a higher frequency of 0.465 THz, predominantly y-directed emission is observed (Fig. 4.8(d)), which is consistent with the FDTD simulation (Fig. 4.8(e))) and to the corresponding rotated IFC (Fig. 4.8(f)). This suggests that the direction of emission can be controlled not only by changing the excitation frequency but also by changing the orientation of the source dipole according to the orientation of the PC, opening up potential additional possibilities for spatial and frequency multiplexing on a single chip-based platform.

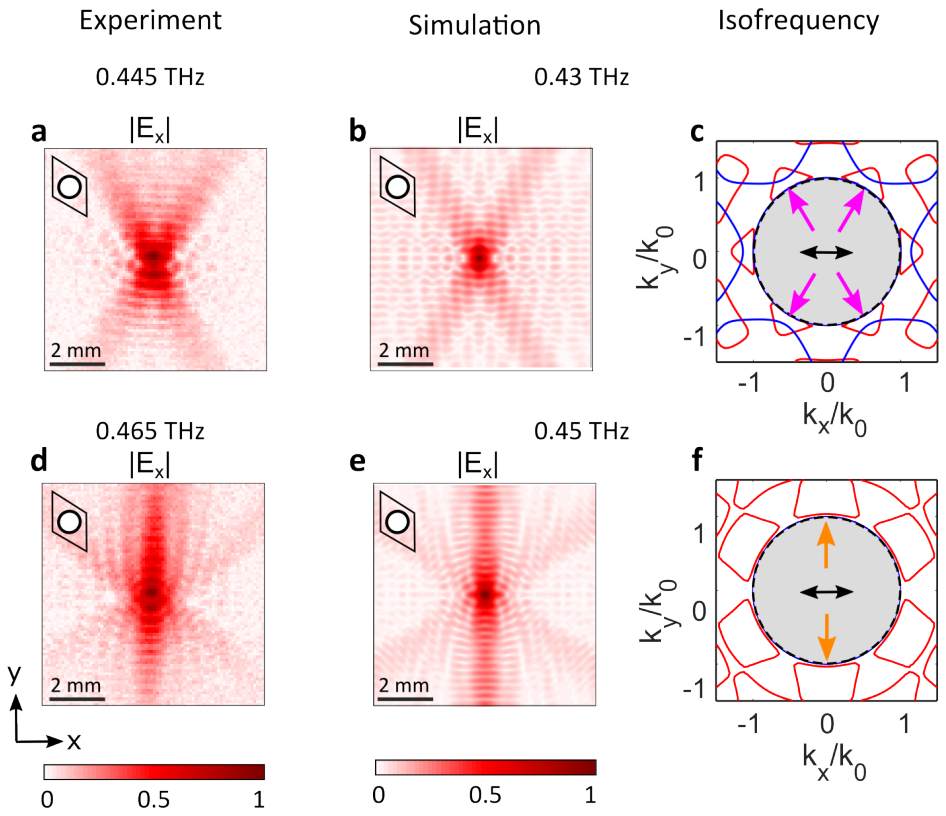

Figure 4.8 – Redirection of the emission by rotating the PC keeping the dipole at the same position, as highlighted by the schematics of the unit cell in the corner of the field-maps. (a) Measured x-component of the electric field magnitude for an x-polarized emitter placed on the opposite side and at 0.445 THz. (b) Corresponding numerical simulations at 0.43 THz. (c) and (f) show the corresponding IFC. (d) and (e) are the experiment and simulation at 0.465 THz, and 0.45 THz. Black arrows in (c) and (f) indicate dipole orientation on the surface.

Then, we investigate how the distance between antennas and the PC can influence the detected field distribution. In our experimental configuration, the emitter and detector antenna are placed at an approximate distance $h_e = h_d = 200\mu$m from the edge of the PC such that it lies in the radiating near-field (i.e., such that $\lambda/2\pi < h < \lambda$ [155]). At this position, the higher k Bloch modes cannot be pressed, as shown in Figure 4.7,

where we show the 2D Fourier transforms of the measured complex fields. Although the distance from the PC is critical for antenna Bloch mode coupling, our experimental setup lacks precise control of this distance. To study the impact of varying distances between the antenna and the PC, we conducted additional simulations. In these simulations, we fixed the emitter at height $h_e = 200\mu m$ and varied the detector distance from the PC h_d. The results are shown in figure 4.9. According to the reciprocity theorem, changing the height h_e to the PC with the fixed h_d will give the same results as changing the height h_d with the fixed h_e . In figure 4.9(b) we can see that the main characteristics of the measured images depend weakly on the distance to the detector, as long as it remains within approximately one wavelength of the sample surface. Field distributions maintain the expected X shape for all considered distances. However, field enhancement decreases compared to free space, especially at longer distances ($h_d > 300\mu m$). For shorter distances, in the calculated ratio with reference case (see figure 4.9(c)) the direction of the field propagation is highlighted in red, indicating that the field has been enhanced by more than a factor of 2. In contrast, for large distances, this ratio approaches 1. By examining the calculated 2D Fourier transform of the simulated field maps (Fig. 4.9(d)), we observe that at $h_d = 0\mu m$ the detector can couple two modes, even those far from the light line. We can conclude that even when the emitter is placed at $h_e = 200\mu m$ these modes still can be exited. However, at $h_d = 200\mu m$, only the closest modes are detected.

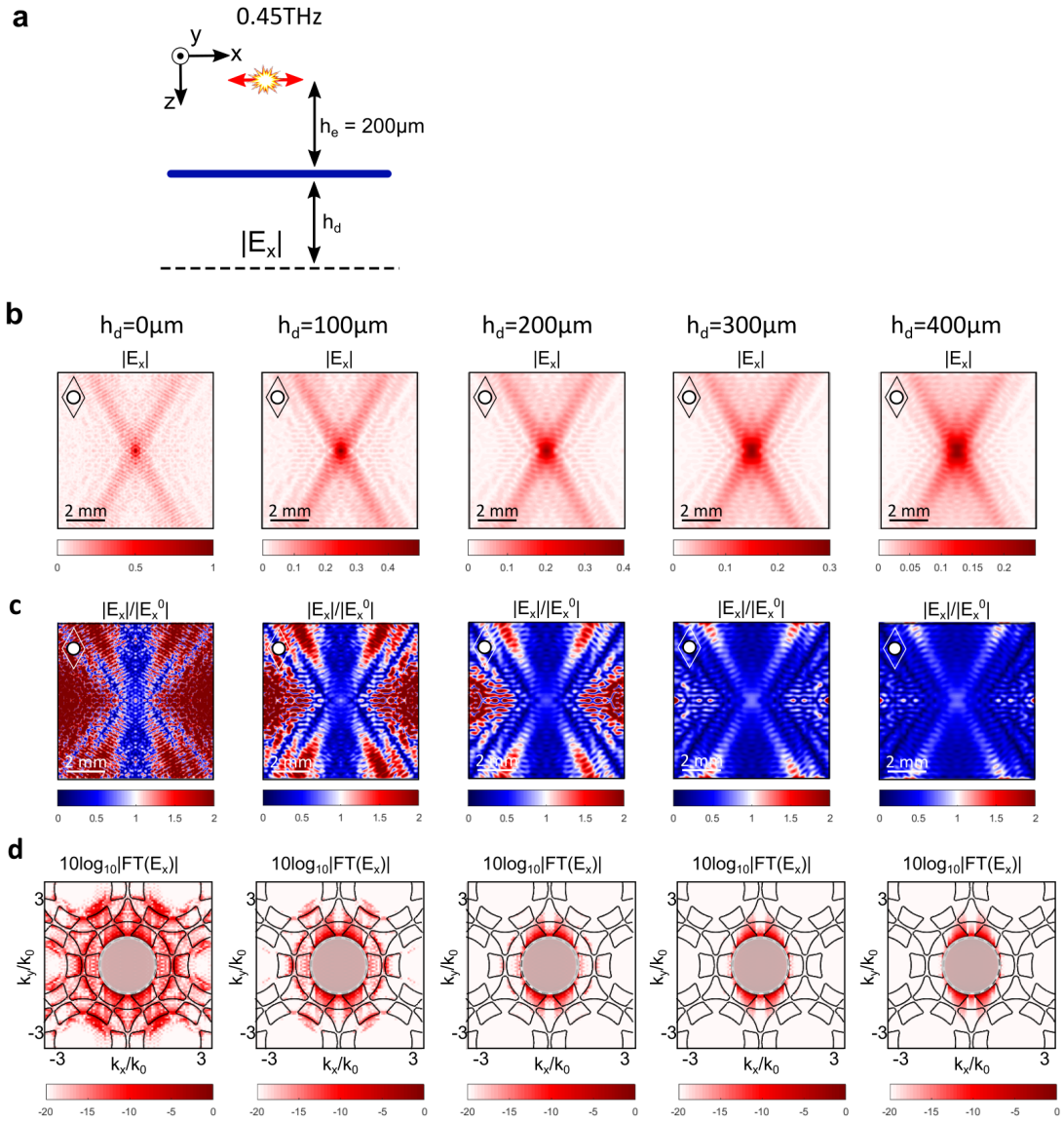

Figure 4.9 – FDTD simulations show the effect of increasing detector distance. (a) We consider the same emitter configuration as in previous simulations at 0.45 THz, keeping the distance $h_e = 200\,\mu$m between the emitter and the PC constant, but we vary the distance h_d between the detector and the PC. (b) The field magnitude $|E_x|$ is shown for $h_d = 0\,\mu$m, $h_d = 100\,\mu$m, $h_d = 200\,\mu$m $h_d = 300\,\mu$m, and $h_d = 400\,\mu$m. All amplitudes are normalized to the maximum of the $h_d = 0\,\mu$m. (c) The ratio of the electric field $|E_x|$ to the reference case of the free space. Note that the overall emission pattern is nominally unchanged, but the field amplitude goes down as the detector distance increases. (d) Two-dimensional Fourier transform of the simulated electric field.

Access to higher Bloch modes can be achieved by placing dipoles with appropriate

polarization inside the PC and detecting the field directly on the PC surface. However, this configuration is not currently available in the experimental setup. To further explore this problem, we performed additional FDTD simulations at 0.43 THz to excite both TM and TE modes using z-polarized electric and magnetic dipoles, as shown in the figures 4.10 (a) and (b). We present the imaginary part of the vertically polarized electric field (E_z) for the TM modes, the imaginary part of the magnetic field (Hz) for the TE modes, and the 2D Fourier transform compared to the calculated IFCs. The field has an extremely complex distribution in both cases, since all modes are excited, even outside the first Brillouin zone. Typically, most of these modes decay quickly and are not detected. However, this configuration excites unwanted high k modes, which may harm guided emission in this context.

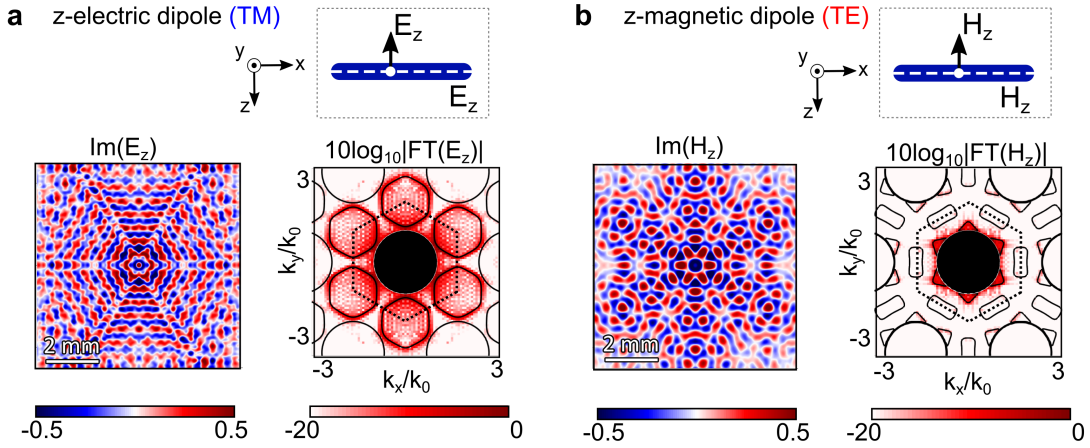

Figure 4.10 – Simulations when a z-polarized (a) electric- and (b) magnetic- dipole is placed at the center of the PC. In this case, the high-k quasi-TM and quasi-TE Bloch modes can be excited independently. In contrast, the x-polarized dipole in b) excites only a subset of the quasi-TE modes shown in d). The schematics on top, show the reference frame and simulation configurations. The dark blue region represents the PC.

4.3 Outline

Metasurfaces and PCs are powerful tools for manipulating the electromagnetic field, helping to suppress, concentrate, and redirect emitted radiation. Although existing methodologies for measuring metasurface near fields in the microwave range have been reviewed in the previous chapters, similar measurements in the terahertz (THz) range, in between microwave and optical ranges, have yet to be performed due to technical challenges. Our innovative terahertz near-field emission/detection setup with broadband antennas that are located on opposite sides of the sample provides a breakthrough in making such measurements. Using this versatile method, we characterized the directional emission properties of a silicon-based PC. Our experiments

reveal near-field suppression in two quasi-TE band gaps at 0.365 THz and 0.495 THz, and directional emission at 0.445 and 0.465 THz with only 20 GHz differences. The directional emission we observed is influenced by the complex band structure of the PC. Interestingly, a small change in the orientation of the dipole axis with respect to the PC's unit cell caused the signal to change direction. Our experimental results align well with the simulations, with a prediction error of 3%. This underscores the need for comprehensive measurements on real samples, addressing imperfections that are inaccessible to simulations alone. These results highlight the potential of bulk PCs as a promising direction for 6G circuit elements and highlight the versatility of PCs for customized emission on chip-based platforms.

Conclusion and Perspective

This thesis investigates the complex dynamics of near-field interactions and control in the microwave, terahertz (THz), and optical frequency ranges. Our research spans from fundamental theoretical concepts to practical experimental confirmations, widening our understanding of the complex behavior of energy transfer processes and their control with a nanophotonic media.

In Chapter 1, we introduced fundamental concepts such as FRET rate and spontaneous emission. Using analogies between optical FRET rate measurements and microwave antenna experiments, we discussed methodologies to overcome challenges such as weak signals and limited spatial resolution. Chapter 2 examines energy transfer between dipole antennas in the microwave range. We studied the effect of antenna size on energy transfer in free space and energy transfer enhancement near the PEC mirror. By developing analytical models and conducting microwave experiments, we looked into the relationship between antenna geometry and energy transfer. We compared our results with existing optical experiments, highlighted the importance of dipole orientation for energy transfer, and suggested the orientation averaging technique for FRET rate enhancement measurements. In Chapter 3, our attention turned to metasurfaces and their role in controlling near-field energy transfer. Through microwave measurements and numerical simulations, we investigated the hyperbolic metasurface known for its extreme anisotropy. We designed the metasurface that supports surface modes, similar to surface plasmons in optical physics, to study its influence on energy transfer and LDOS. By drawing parallels with optical experiments, we have shown an enhancement of energy transfer and LDOS when the surface mode is present. Like this, using these measurement methods, variety of geometries can be studied to find the relationship between the LDOS and FRET rate.

As the next step in this direction, an analogy between microwave experiments and FRET efficiency can be studied. The FRET efficiency shows the probability that the donor will transfer its energy to the acceptor over all other possible decay paths. The FRET efficiency, as a FRET rate, is influenced by the distance between the donor and acceptor molecules, their relative dipole orientations, and the spectral overlap between the donor emission and acceptor absorption and it can be modeled as:

$$E_{FRET} = \frac{1}{1 + \frac{R^6}{R_0^6 k^2}} \tag{4.1}$$

where R is the distance between the donor and acceptor molecules, and R_0 is the Förster distance, where the efficiency is exactly 0.5 [156]. The Förster distance is a characteristic distance at which the FRET efficiency is 50%. The Förster distance

depends on the spectral properties of quantum emitters and their mutual orientation. When two dipoles are parallel to each other, we have the probability of having a high energy efficiency. If the dipole moments are perpendicular to each other, the FRET efficiency approaches zero. k^2 factor changes from 0 to 4 and often is taken at 2/3 assuming both dipoles rotate freely on a timescale faster than the fluorescence lifetime of the donor in the presence of the acceptor. For the parallel dipoles k is equal to 1 and for the aligned is 4. It means that for the same dipoles, the Förster distance is going to be 1.26 times more for the aligned configuration, than for the parallel. E_{FRET} calculated with Eq 4.1 for the different dipole orientations is shown in Figure 4.11

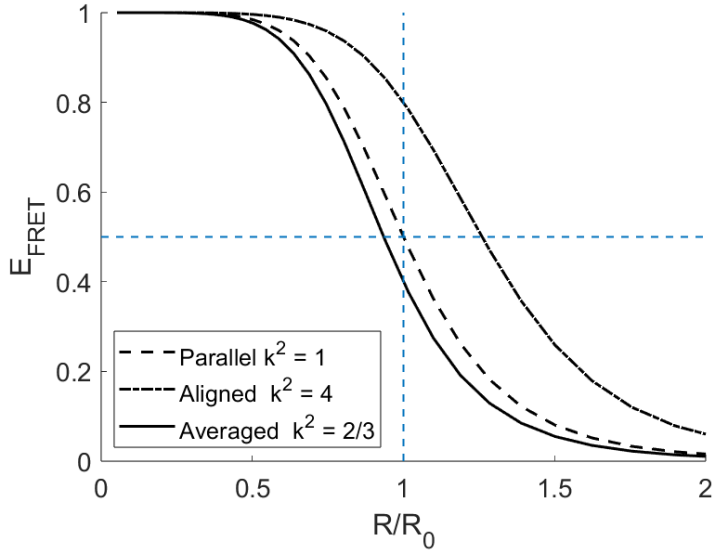

Figure 4.11 – Distance dependence of FRET efficiency for the parallel, aligned, and averaged orientated dipoles in the vacuum. R is the dipole-dipole distance, k_0 is the wave number for the vacuum

However, an analogy to this parameter in the microwave regime was never discussed before. Here, we briefly discuss the possibility of measuring similar values with real-sized antennas at microwave frequencies. The effectiveness of energy transfer in microwave experiments can be expressed as a fraction of the donor energy that is transferred to the acceptor through all possible energy dissipation pathways. This can be expressed using the transmission coefficient S_{21}, which is normalized by the reflection coefficient S_{11} at the donor input in the free space.

$$E_{ET} = \frac{|S_{21}|^2}{1-|S_{11}|^2} \tag{4.2}$$

The fraction of power delivered to the acceptor is represented by $(S_{21})^2$, while the total power radiated by the donor is $(1-(S_{11})^2)$. We conducted numerical simulations in the time-domain (FDTD) solver of CST Microwave Studio 2019 to find a size dependence of this value of the dipole length. In figure 4.12 we show the results of

the numerical simulations of E_{ET} for (a) parallel and (b) aligned dipoles. The results for different antenna sizes ($L = \lambda/60,\ \lambda/30,\ \lambda/10,\ \lambda/6$) are shown with colorful lines. With black dashed lines, we show analytical curves to fit the results, and a horizontal blue dashed line measures the efficiency level of 0.5, which corresponds to the Forster radius R_0.

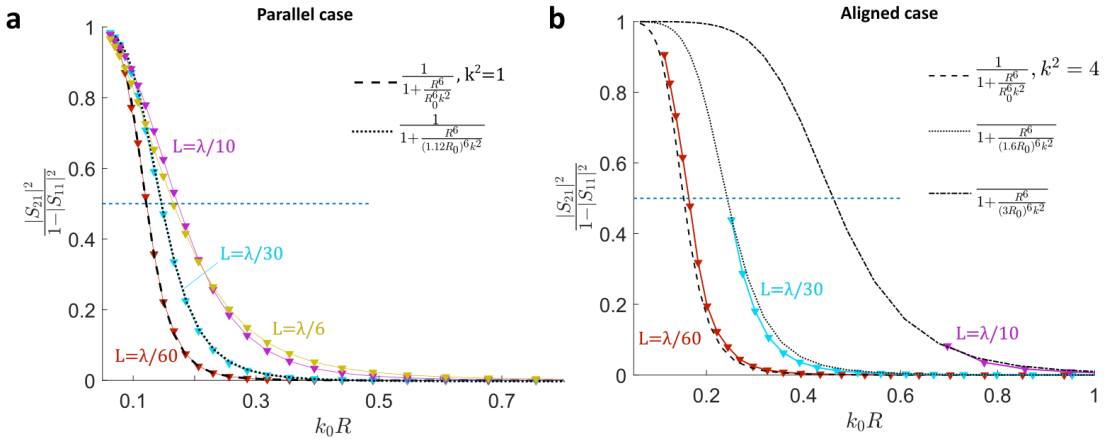

Figure 4.12 – Numerical simulations of the Energy transfer efficiency compared for real-sized antennas (linear scale): a) parallel case; b) aligned

For both orientations, the expected shape of the curve is found for the smallest dipole ($L = \lambda/60$). In the parallel case, the curve is perfectly aligned with the analytical formula when the Forster radius is $R_0 k_0 = 0.1213$. For the aligned case, as expected, the Forster radius remains the same, but with the coefficient $k^2 = 4$. For the bigger dipoles, the Forster radius changes non-uniformly for the parallel and aligned cases. Moreover, for the aligned case, it is no longer possible to measure the efficiency greater than 0.5 for the dipole with $L \geq \lambda/30$. We can conclude that for free space FRET efficiency measurements similar to the FRET rate, we need to use antennas smaller than $\lambda/30$ to get accurate results. This novel approach to measuring the FRET efficiency can open new possibilities for the application of antenna measurements to explore complex near-field effects in the optic range.

Finally, Chapter 4 covered near-field measurements in the terahertz frequency range. By performing innovative experiments in the near field of a photonic crystal, we showed bandgap field suppression and frequency-dependent directional emission. Due to the extreme sensitivity of photonic crystal band structures to specific designs, our experimental technique will provide a valuable tool for refining device development due to practical limits during fabrication. In the field of quantum optics, strongly modified emission properties induced by the photonic crystal could also be used to mediate the strong anisotropic dipole-dipole coupling of individual quantum emitters [140], whose development at terahertz frequencies is in a nascent stage [157, 158]. More broadly, this terahertz near-field excitation and detection scheme may provide a useful and versatile tool for better understanding or revealing new physics over broad bandwidths, particularly in situations where large-scale numerical simula-

tions become prohibitively slow and computationally demanding. Moving back to optical frequencies, near-field control of the use of metamaterials can open a new perspective for the building of new photodetectors for a wide range of applications, from telecommunications and sensing to medical imaging and environmental monitoring. In such devices, a silicon absorber, serves to efficiently absorb incident photons and convert their energy into electron-hole pairs within the semiconductor material of the photodetector [159]. The use of metasurface can enhance the efficiency of such absorbers and reduce the Time-of-flight (ToF) of the hole photodetector system. The reduction in ToF is also critical in medical imaging applications and systems used for autonomous vehicles, robotics, and environmental mapping.

In conclusion, this thesis has contributed to a deeper understanding of near-field interactions and control mechanisms in different frequency ranges. By bridging the gap between theoretical concepts and experimental confirmation, we have laid the foundation for future advances in nanophotonics, optoelectronics, and beyond. This work paves the way for new metasurface concepts where the near-field energy transfer is controlled by engineering surface waves propagation in optics, microwaves, and THz.

Bibliography

[1] Kseniia Lezhennikova, Kaizad Rustomji, Boris T. Kuhlmey, Tryfon Antonakakis, Pierre Jomin, Stanislav Glybovski, C. Martijn De Sterke, Jérôme Wenger, Redha Abdeddaim, and Stefan Enoch. "Experimental evidence of Förster energy transfer enhancement in the near field through engineered metamaterial surface waves". en. In: *Communications Physics* 6.1 (2023), p. 229. ISSN: 2399-3650. DOI: 10.1038/s42005-023-01347-1 (cit. on pp. 3, 67).

[2] Ilya Deriy, Ksenia Lezhennikova, Stanislav Glybovski, Pavel Belov, Ivan Iorsh, Mingzhao Song, and Andrey Bogdanov. "No reflection paradox at the boundary of hyperbolic medium". In: *Optical Manipulation and Structured Materials Conference*. Ed. by Takashige Omatsu, Síle N. Chormaic, and Kishan Dholakia. Yokohama, Japan: SPIE, Sept. 2023, p. 45. DOI: 10.1117/12.3008377 (cit. on pp. 3, 9, 67, 74).

[3] Kseniia Lezhennikova, Sahand Mahmoodian, Boris T. Kuhlmey, Redha Abdeddaim, Stefan Enoch, C. Martijn De Sterke, and Alessandro Tuniz. "Broadband Terahertz Near-Field Excitation and Detection of Silicon Photonic Crystal Modes". en. In: *ACS Photonics* 10.12 (2023), pp. 4447–4455. ISSN: 2330-4022, 2330-4022. DOI: 10.1021/acsphotonics.3c01312 (cit. on pp. 3, 92).

[4] Kseniia Lezhennikova, Kaizad Rustomji, Pierre Jomin, Stanislav Glybovski, C. Martijn De Sterke, Jerome Wenger, Redha Abdeddaim, and Stefan Enoch. "Microwave analogy of Förster resonance energy transfer and effect of finite antenna length". en. In: *Scientific Reports* 14.1 (May 2024), p. 10485. ISSN: 2045-2322. DOI: 10.1038/s41598-024-59824-8 (cit. on pp. 3, 45).

[5] Cristian L. Cortes and Zubin Jacob. "Fundamental figures of merit for engineering Förster resonance energy transfer". en. In: *Optics Express* 26.15 (July 2018), p. 19371. ISSN: 1094-4087 (cit. on pp. 7, 32, 35).

[6] Kaizad Rustomji, Marc Dubois, Boris Kuhlmey, C. Martijn De Sterke, Stefan Enoch, Redha Abdeddaim, and Jérôme Wenger. "Direct Imaging of the Energy-Transfer Enhancement between Two Dipoles in a Photonic Cavity". en. In: *Physical Review X* 9.1 (Mar. 2019), p. 011041. ISSN: 2160-3308 (cit. on pp. 7, 10, 27, 30, 35, 36, 41–43, 48, 79, 90).

[7] Martijn Wubs and Willem L Vos. "Förster resonance energy transfer rate in any dielectric nanophotonic medium with weak dispersion". In: *New Journal of Physics* 18.5 (May 2016), p. 053037. ISSN: 1367-2630 (cit. on pp. 8, 10, 43, 46, 47, 63, 79, 90).

[8] Christian Blum, Niels Zijlstra, Ad Lagendijk, Martijn Wubs, Allard P. Mosk, Vinod Subramaniam, and Willem L. Vos. “Nanophotonic Control of the Förster Resonance Energy Transfer Efficiency”. en. In: *Physical Review Letters* 109.20 (Nov. 2012), p. 203601. ISSN: 0031-9007, 1079-7114 (cit. on pp. 8, 10, 35, 36, 46, 47, 63, 79, 90).

[9] Zhiwei Guo, Haitao Jiang, and Hong Chen. “Abnormal Wave Propagation in Tilted Linear-Crossing Metamaterials”. en. In: *Advanced Photonics Research* 2.1 (Jan. 2021), p. 2000071. ISSN: 2699-9293, 2699-9293. DOI: 10.1002/adpr.202000071 (cit. on pp. 9, 74).

[10] Zhigao Dai et al. “Edge-oriented and steerable hyperbolic polaritons in anisotropic van der Waals nanocavities”. en. In: *Nature Communications* 11.1 (Nov. 2020), p. 6086. ISSN: 2041-1723. DOI: 10.1038/s41467-020-19913-4 (cit. on pp. 9, 74).

[11] Piers Andrew and William L. Barnes. “Förster Energy Transfer in an Optical Microcavity”. en. In: *Science* 290.5492 (Oct. 2000), pp. 785–788. ISSN: 0036-8075, 1095-9203. DOI: 10.1126/science.290.5492.785 (cit. on pp. 10, 35, 79, 90).

[12] Petru Ghenuche, Juan De Torres, Satish Babu Moparthi, Victor Grigoriev, and Jérôme Wenger. “Nanophotonic Enhancement of the Förster Resonance Energy-Transfer Rate with Single Nanoapertures”. en. In: *Nano Letters* 14.8 (Aug. 2014), pp. 4707–4714. ISSN: 1530-6984, 1530-6992 (cit. on pp. 10, 35, 79, 90).

[13] Alexander Konrad, Michael Metzger, Andreas M. Kern, Marc Brecht, and Alfred J. Meixner. “Controlling the dynamics of Förster resonance energy transfer inside a tunable sub-wavelength Fabry–Pérot-resonator”. en. In: *Nanoscale* 7.22 (2015), pp. 10204–10209. ISSN: 2040-3364, 2040-3372 (cit. on pp. 10, 35, 36, 79, 90).

[14] Jhih-Sheng Wu, Yen-Cheng Lin, Yae-Lin Sheu, and Liang-Yan Hsu. “Characteristic Distance of Resonance Energy Transfer Coupled with Surface Plasmon Polaritons”. en. In: *The Journal of Physical Chemistry Letters* 9.24 (Dec. 2018), pp. 7032–7039. ISSN: 1948-7185, 1948-7185 (cit. on pp. 10, 36, 79, 90).

[15] Lukas Novotny and Bert Hecht. *Principles of Nano-Optics*. 1st ed. Cambridge University Press, June 2006 (cit. on pp. 10, 31, 33, 34, 62, 83, 90).

[16] Mikhail Baibakov, Satyajit Patra, Jean-Benoît Claude, Antonin Moreau, Julien Lumeau, and Jérôme Wenger. “Extending Single-Molecule Förster Resonance Energy Transfer (FRET) Range beyond 10 Nanometers in Zero-Mode Waveguides”. en. In: *ACS Nano* 13.7 (July 2019), pp. 8469–8480. ISSN: 1936-0851, 1936-086X (cit. on pp. 11, 35, 36, 90, 91).

[17] Ashwin K. Boddeti, Jun Guan, Tyler Sentz, Xitlali Juarez, Ward Newman, Cristian Cortes, Teri W. Odom, and Zubin Jacob. “Long-Range Dipole–Dipole Interactions in a Plasmonic Lattice”. en. In: *Nano Letters* 22.1 (Jan. 2022), pp. 22–28. ISSN: 1530-6984, 1530-6992 (cit. on pp. 11, 36, 91).

[18] William L Barnes, Simon A R Horsley, and Willem L Vos. “Classical antennas, quantum emitters, and densities of optical states”. In: *Journal of Optics* 22.7 (July 2020), p. 073501. ISSN: 2040-8978, 2040-8986 (cit. on pp. 31, 32, 35, 36, 40, 85, 88).

[19] Edward M Purcell, Henry Cutler Torrey, and Robert V Pound. “Resonance absorption by nuclear magnetic moments in a solid”. In: *Physical review* 69.1-2 (1946), p. 37 (cit. on p. 32).

[20] Kaizad Rustomji, Marc Dubois, Pierre Jomin, Stefan Enoch, Jérôme Wenger, C. Martijn De Sterke, and Redha Abdeddaim. “Complete Electromagnetic Dyadic Green Function Characterization in a Complex Environment – Resonant Dipole-Dipole Interaction and Cooperative Effects”. en. In: *Physical Review X* 11.2 (Apr. 2021), p. 021004. ISSN: 2160-3308 (cit. on pp. 32, 41, 48, 90).

[21] Th. Förster. “Zwischenmolekulare Energiewanderung und Fluoreszenz”. en. In: *Annalen der Physik* 437.1-2 (Jan. 1948), pp. 55–75. ISSN: 0003-3804, 1521-3889 (cit. on p. 33).

[22] Constantine A. Balanis. *Advanced engineering electromagnetics*. 2nd ed. Hoboken, N.J: John Wiley & Sons, 2012. ISBN: 978-0-470-58948-9 (cit. on pp. 34, 38).

[23] R. Carminati, A. Cazé, D. Cao, F. Peragut, V. Krachmalnicoff, R. Pierrat, and Y. De Wilde. “Electromagnetic density of states in complex plasmonic systems”. en. In: *Surface Science Reports* 70.1 (Mar. 2015), pp. 1–41. ISSN: 01675729 (cit. on pp. 35, 85).

[24] Abdullah O. Hamza, Francesco N. Viscomi, Jean-Sebastien G. Bouillard, and Ali M. Adawi. “Förster Resonance Energy Transfer and the Local Optical Density of States in Plasmonic Nanogaps”. en. In: *The Journal of Physical Chemistry Letters* 12.5 (Feb. 2021), pp. 1507–1513. ISSN: 1948-7185, 1948-7185 (cit. on pp. 35, 90).

[25] M. Hopmeier, W. Guss, M. Deussen, E. O. Göbel, and R. F. Mahrt. “Enhanced Dipole-Dipole Interaction in a Polymer Microcavity”. en. In: *Physical Review Letters* 82.20 (May 1999), pp. 4118–4121. ISSN: 0031-9007, 1079-7114 (cit. on p. 35).

[26] Nesrine Aissaoui, Kasper Moth-Poulsen, Mikael Käll, Peter Johansson, L. Marcus Wilhelmsson, and Bo Albinsson. “FRET enhancement close to gold nanoparticles positioned in DNA origami constructs”. en. In: *Nanoscale* 9.2 (2017), pp. 673–683. ISSN: 2040-3364, 2040-3372 (cit. on pp. 35, 90).

[27] Juan De Torres, Mathieu Mivelle, Satish Babu Moparthi, Hervé Rigneault, Niek F. Van Hulst, María F. García-Parajó, Emmanuel Margeat, and Jérôme Wenger. “Plasmonic Nanoantennas Enable Forbidden Förster Dipole–Dipole Energy Transfer and Enhance the FRET Efficiency”. en. In: *Nano Letters* 16.10 (Oct. 2016), pp. 6222–6230. ISSN: 1530-6984, 1530-6992 (cit. on pp. 35, 36).

[28] Sébastien Bidault, Alexis Devilez, Petru Ghenuche, Brian Stout, Nicolas Bonod, and Jérôme Wenger. "Competition between Förster Resonance Energy Transfer and Donor Photodynamics in Plasmonic Dimer Nanoantennas". en. In: *ACS Photonics* 3.5 (May 2016), pp. 895–903. ISSN: 2330-4022, 2330-4022 (cit. on pp. 35, 90).

[29] Satyajit Patra, Jean-Benoît Claude, and Jérôme Wenger. "Fluorescence Brightness, Photostability, and Energy Transfer Enhancement of Immobilized Single Molecules in Zero-Mode Waveguide Nanoapertures". en. In: *ACS Photonics* 9.6 (June 2022), pp. 2109–2118. ISSN: 2330-4022, 2330-4022 (cit. on pp. 35, 90).

[30] Freddy T. Rabouw, Stephan A. Den Hartog, Tim Senden, and Andries Meijerink. "Photonic effects on the Förster resonance energy transfer efficiency". en. In: *Nature Communications* 5.1 (Apr. 2014), p. 3610. ISSN: 2041-1723 (cit. on p. 35).

[31] Frank Schleifenbaum, Andreas M. Kern, Alexander Konrad, and Alfred J. Meixner. "Dynamic control of Förster energy transfer in a photonic environment". en. In: *Phys. Chem. Chem. Phys.* 16.25 (2014), pp. 12812–12817. ISSN: 1463-9076, 1463-9084 (cit. on p. 35).

[32] Diane J. Roth, Mazhar E. Nasir, Pavel Ginzburg, Pan Wang, Alix Le Marois, Klaus Suhling, David Richards, and Anatoly V. Zayats. "Förster Resonance Energy Transfer inside Hyperbolic Metamaterials". en. In: *ACS Photonics* 5.11 (Nov. 2018), pp. 4594–4603. ISSN: 2330-4022, 2330-4022 (cit. on p. 35).

[33] Natalia A. Kostina, Denis A. Kislov, Aliaksandra N. Ivinskaya, Alexey Proskurin, Dmitrii N. Redka, Andrey Novitsky, Pavel Ginzburg, and Alexander S. Shalin. "Nanoscale Tunable Optical Binding Mediated by Hyperbolic Metamaterials". en. In: *ACS Photonics* 7.2 (Feb. 2020), pp. 425–433. ISSN: 2330-4022, 2330-4022. DOI: 10.1021/acsphotonics.9b01378 (cit. on p. 35).

[34] Maria Sanz-Paz, Jerome Wenger, Niek F. Van Hulst, Mathieu Mivelle, and Maria F. Garcia-Parajo. "Nanoscale control of single molecule Förster resonance energy transfer by a scanning photonic nanoantenna". en. In: *Nanophotonics* 9.12 (Sept. 2020), pp. 4021–4031. ISSN: 2192-8614, 2192-8606 (cit. on pp. 35, 36, 90).

[35] J. Bohlen, Á. Cuartero-González, E. Pibiri, D. Ruhlandt, A. I. Fernández-Domínguez, P. Tinnefeld, and G. P. Acuna. "Plasmon-assisted Förster resonance energy transfer at the single-molecule level in the moderate quenching regime". en. In: *Nanoscale* 11.16 (2019), pp. 7674–7681. ISSN: 2040-3364, 2040-3372 (cit. on pp. 35, 36, 90).

[36] Dilusha Weeraddana, Malin Premaratne, Sarath D. Gunapala, and David L. Andrews. "Controlling resonance energy transfer in nanostructure emitters by positioning near a mirror". en. In: *The Journal of Chemical Physics* 147.7 (Aug. 2017), p. 074117. ISSN: 0021-9606, 1089-7690 (cit. on p. 35).

[37] Yeonjun Jeong and George C. Schatz. “Enhancement and Suppression of Resonance Energy Transfer Near Metal Nanoparticles”. en. In: *The Journal of Physical Chemistry C* 124.37 (Sept. 2020), pp. 20589–20597. ISSN: 1932-7447, 1932-7455 (cit. on pp. 35, 90).

[38] Robert Collison, Juan B. Pérez-Sánchez, Matthew Du, Jacob Trevino, Joel Yuen-Zhou, Stephen O’Brien, and Vinod M. Menon. “Purcell Effect of Plasmonic Surface Lattice Resonances and Its Influence on Energy Transfer”. en. In: *ACS Photonics* 8.8 (Aug. 2021), pp. 2211–2219. ISSN: 2330-4022, 2330-4022 (cit. on p. 35).

[39] Gregory D. Scholes. “Long-Range Resonance Energy Transfer in Molecular Systems”. In: *Annual Review of Physical Chemistry* 54.1 (2003), pp. 57–87 (cit. on p. 35).

[40] Igor Nabiev, Aliaksandra Rakovich, Alyona Sukhanova, Evgeniy Lukashev, Vadim Zagidullin, Vladimir Pachenko, Yury P. Rakovich, John F. Donegan, Andrei B. Rubin, and Alexander O. Govorov. “Fluorescent Quantum Dots as Artificial Antennas for Enhanced Light Harvesting and Energy Transfer to Photosynthetic Reaction Centers”. en. In: *Angewandte Chemie International Edition* 49.40 (Aug. 2010), pp. 7217–7221. ISSN: 14337851 (cit. on p. 35).

[41] Gregory D. Scholes and Graham R. Fleming. “On the Mechanism of Light Harvesting in Photosynthetic Purple Bacteria: B800 to B850 Energy Transfer”. en. In: *The Journal of Physical Chemistry B* 104.8 (Mar. 2000), pp. 1854–1868. ISSN: 1520-6106, 1520-5207 (cit. on p. 35).

[42] Gregory D. Scholes, Xanthipe J. Jordanides, and Graham R. Fleming. “Adapting the Förster Theory of Energy Transfer for Modeling Dynamics in Aggregated Molecular Assemblies”. en. In: *The Journal of Physical Chemistry B* 105.8 (Mar. 2001), pp. 1640–1651. ISSN: 1520-6106, 1520-5207. DOI: 10.1021/jp003571m (cit. on p. 35).

[43] M. A. Baldo, M. E. Thompson, and S. R. Forrest. “High-efficiency fluorescent organic light-emitting devices using a phosphorescent sensitizer”. en. In: *Nature* 403.6771 (Feb. 2000), pp. 750–753. ISSN: 0028-0836, 1476-4687 (cit. on p. 35).

[44] B. W. D’Andrade and S. R. Forrest. “White Organic Light-Emitting Devices for Solid-State Lighting”. en. In: *Advanced Materials* 16.18 (Sept. 2004), pp. 1585–1595. ISSN: 0935-9648, 1521-4095 (cit. on p. 35).

[45] Eitan Lerner, Thorben Cordes, Antonino Ingargiola, Yazan Alhadid, SangYoon Chung, Xavier Michalet, and Shimon Weiss. “Toward dynamic structural biology: Two decades of single-molecule Förster resonance energy transfer”. en. In: *Science* 359.6373 (Jan. 2018), eaan1133. ISSN: 0036-8075, 1095-9203 (cit. on p. 35).

[46] Igor L. Medintz, Aaron R. Clapp, Hedi Mattoussi, Ellen R. Goldman, Brent Fisher, and J. Matthew Mauro. “Self-assembled nanoscale biosensors based on quantum dot FRET donors”. en. In: *Nature Materials* 2.9 (Sept. 2003), pp. 630–638. ISSN: 1476-1122, 1476-4660 (cit. on p. 35).

[47] Niko Hildebrandt, Christopher M. Spillmann, W. Russ Algar, Thomas Pons, Michael H. Stewart, Eunkeu Oh, Kimihiro Susumu, Sebastian A. Díaz, James B. Delehanty, and Igor L. Medintz. “Energy Transfer with Semiconductor Quantum Dot Bioconjugates: A Versatile Platform for Biosensing, Energy Harvesting, and Other Developing Applications”. en. In: *Chemical Reviews* 117.2 (Jan. 2017), pp. 536–711. ISSN: 0009-2665, 1520-6890. DOI: 10.1021/acs.chemrev.6b00030 (cit. on p. 35).

[48] David M. Coles, Niccolo Somaschi, Paolo Michetti, Caspar Clark, Pavlos G. Lagoudakis, Pavlos G. Savvidis, and David G. Lidzey. “Polariton-mediated energy transfer between organic dyes in a strongly coupled optical microcavity”. en. In: *Nature Materials* 13.7 (July 2014), pp. 712–719. ISSN: 1476-1122, 1476-4660 (cit. on p. 35).

[49] Xiaolan Zhong, Thibault Chervy, Shaojun Wang, Jino George, Anoop Thomas, James A. Hutchison, Eloise Devaux, Cyriaque Genet, and Thomas W. Ebbesen. “Non-Radiative Energy Transfer Mediated by Hybrid Light-Matter States”. en. In: *Angewandte Chemie International Edition* 55.21 (May 2016), pp. 6202–6206. ISSN: 14337851 (cit. on p. 35).

[50] Francisco J. Garcia-Vidal and Johannes Feist. “Long-distance operator for energy transfer”. en. In: *Science* 357.6358 (Sept. 2017), pp. 1357–1358. ISSN: 0036-8075, 1095-9203 (cit. on p. 35).

[51] Renate Landig, Lorenz Hruby, Nishant Dogra, Manuele Landini, Rafael Mottl, Tobias Donner, and Tilman Esslinger. “Quantum phases from competing short- and long-range interactions in an optical lattice”. en. In: *Nature* 532.7600 (Apr. 2016), pp. 476–479. ISSN: 0028-0836, 1476-4687 (cit. on p. 35).

[52] D. Bluvstein et al. “Controlling quantum many-body dynamics in driven Rydberg atom arrays”. en. In: *Science* 371.6536 (Mar. 2021), pp. 1355–1359. ISSN: 0036-8075, 1095-9203 (cit. on p. 35).

[53] Klaus Osterloh, Nuria Barberán, and Maciej Lewenstein. “Strongly Correlated States of Ultracold Rotating Dipolar Fermi Gases”. en. In: *Physical Review Letters* 99.16 (Oct. 2007), p. 160403. ISSN: 0031-9007, 1079-7114 (cit. on p. 35).

[54] Cristian L. Cortes and Zubin Jacob. “Super-Coulombic atom–atom interactions in hyperbolic media”. en. In: *Nature Communications* 8.1 (Jan. 2017), p. 14144. ISSN: 2041-1723 (cit. on p. 36).

[55] J. Keaveney, A. Sargsyan, U. Krohn, I. G. Hughes, D. Sarkisyan, and C. S. Adams. “Cooperative Lamb Shift in an Atomic Vapor Layer of Nanometer Thickness”. en. In: *Physical Review Letters* 108.17 (Apr. 2012), p. 173601. ISSN: 0031-9007, 1079-7114 (cit. on p. 36).

[56] Vitaliy N. Pustovit and Tigran V. Shahbazyan. “Cooperative emission of light by an ensemble of dipoles near a metal nanoparticle: The plasmonic Dicke effect”. en. In: *Physical Review Letters* 102.7 (Feb. 2009), p. 077401. ISSN: 0031-9007, 1079-7114 (cit. on p. 36).

[57] D. Bouchet, D. Cao, R. Carminati, Y. De Wilde, and V. Krachmalnicoff. “Long-Range Plasmon-Assisted Energy Transfer between Fluorescent Emitters”. en. In: *Physical Review Letters* 116.3 (Jan. 2016), p. 037401. ISSN: 0031-9007, 1079-7114 (cit. on p. 36).

[58] Yu-Chen Wei, Ming-Wei Lee, Pi-Tai Chou, Gregory D. Scholes, George C. Schatz, and Liang-Yan Hsu. “Can Nanocavities Significantly Enhance Resonance Energy Transfer in a Single Donor–Acceptor Pair?” en. In: *The Journal of Physical Chemistry C* 125.33 (Aug. 2021), pp. 18119–18128. ISSN: 1932-7447, 1932-7455 (cit. on p. 36).

[59] P M De Roque, N F Van Hulst, and R Sapienza. “Nanophotonic boost of intermolecular energy transfer”. In: *New Journal of Physics* 17.11 (Nov. 2015), p. 113052. ISSN: 1367-2630 (cit. on p. 36).

[60] Juan De Torres, Patrick Ferrand, Gérard Colas Des Francs, and Jérôme Wenger. “Coupling Emitters and Silver Nanowires to Achieve Long-Range Plasmon-Mediated Fluorescence Energy Transfer”. en. In: *ACS Nano* 10.4 (Apr. 2016), pp. 3968–3976. ISSN: 1936-0851, 1936-086X (cit. on p. 36).

[61] P. Andrew and W. L. Barnes. “Energy Transfer Across a Metal Film Mediated by Surface Plasmon Polaritons”. en. In: *Science* 306.5698 (Nov. 2004), pp. 1002–1005. ISSN: 0036-8075, 1095-9203 (cit. on p. 36).

[62] Ward D. Newman, Cristian L. Cortes, Amir Afshar, Ken Cadien, Al Meldrum, Robert Fedosejevs, and Zubin Jacob. “Observation of long-range dipole-dipole interactions in hyperbolic metamaterials”. en. In: *Science Advances* 4.10 (Oct. 2018), eaar5278. ISSN: 2375-2548 (cit. on p. 36).

[63] Frederick D. Lewis, Ligang Zhang, and Xiaobing Zuo. “Orientation Control of Fluorescence Resonance Energy Transfer Using DNA as a Helical Scaffold”. en. In: *Journal of the American Chemical Society* 127.28 (July 2005), pp. 10002–10003. ISSN: 0002-7863, 1520-5126 (cit. on p. 36).

[64] Asif Iqbal, Sinan Arslan, Burak Okumus, Timothy J. Wilson, Gerard Giraud, David G. Norman, Taekjip Ha, and David M. J. Lilley. “Orientation dependence in fluorescent energy transfer between Cy3 and Cy5 terminally attached to double-stranded nucleic acids”. en. In: *Proceedings of the National Academy of Sciences* 105.32 (Aug. 2008), pp. 11176–11181. ISSN: 0027-8424, 1091-6490 (cit. on p. 36).

[65] “Precision and accuracy of single-molecule FRET measurements—a multi-laboratory benchmark study”. en. In: *Nature Methods* 15.9 (Sept. 2018), pp. 669–676. ISSN: 1548-7091, 1548-7105 (cit. on p. 36).

[66] Constantine A. Balanis. *Antenna theory: analysis and design*. eng. 3. ed. Hoboken, N.J: Wiley-Interscience, 2005. ISBN: 978-0-471-66782-7 (cit. on pp. 37, 40, 43, 47, 49, 53, 59).

[67] Alexander E. Krasnok, Alexey P. Slobozhanyuk, Constantin R. Simovski, Sergei A. Tretyakov, Alexander N. Poddubny, Andrey E. Miroshnichenko, Yuri S. Kivshar, and Pavel A. Belov. "An antenna model for the Purcell effect". en. In: *Scientific Reports* 5.1 (Aug. 2015), p. 12956. ISSN: 2045-2322 (cit. on pp. 41, 48, 64).

[68] Jean-Jacques Greffet, Marine Laroche, and François Marquier. "Impedance of a Nanoantenna and a Single Quantum Emitter". en. In: *Physical Review Letters* 105.11 (Sept. 2010), p. 117701. ISSN: 0031-9007, 1079-7114. DOI: 10.1103/PhysRevLett.105.117701 (cit. on p. 48).

[69] Kaizad Rustomji, Redha Abdeddaim, C. Martijn De Sterke, Boris Kuhlmey, and Stefan Enoch. "Measurement and simulation of the polarization-dependent Purcell factor in a microwave fishnet metamaterial". en. In: *Physical Review B* 95.3 (Jan. 2017), p. 035156. ISSN: 2469-9950, 2469-9969 (cit. on p. 48).

[70] Julius Adams Stratton. *Electromagnetic Theory*. en. 1st ed. Wiley, Oct. 2015. DOI: 10.1002/9781119134640 (cit. on p. 54).

[71] John David Jackson. *Classical electrodynamics*. 2d ed. New York: Wiley, 1975. ISBN: 978-0-471-43132-9 (cit. on p. 54).

[72] William L. Barnes, Alain Dereux, and Thomas W. Ebbesen. "Surface plasmon subwavelength optics". en. In: *Nature* 424.6950 (Aug. 2003), pp. 824–830. ISSN: 0028-0836, 1476-4687. DOI: 10.1038/nature01937 (cit. on pp. 67, 79).

[73] J. B. Pendry, L. Martín-Moreno, and F. J. Garcia-Vidal. "Mimicking Surface Plasmons with Structured Surfaces". en. In: *Science* 305.5685 (Aug. 2004), pp. 847–848. ISSN: 0036-8075, 1095-9203 (cit. on pp. 67, 79).

[74] Stanislav B. Glybovski, Sergei A. Tretyakov, Pavel A. Belov, Yuri S. Kivshar, and Constantin R. Simovski. "Metasurfaces: From microwaves to visible". en. In: *Physics Reports* 634 (May 2016), pp. 1–72. ISSN: 03701573 (cit. on pp. 67, 68, 80).

[75] I. Anderson. "On the Theory of Self-Resonant Grids". en. In: *Bell System Technical Journal* 54.10 (Dec. 1975), pp. 1725–1731. ISSN: 00058580. DOI: 10.1002/j.1538-7305.1975.tb03551.x (cit. on p. 68).

[76] Olli Luukkonen, Constantin Simovski, GÉrard Granet, George Goussetis, Dmitri Lioubtchenko, Antti V. Raisanen, and Sergei A. Tretyakov. "Simple and Accurate Analytical Model of Planar Grids and High-Impedance Surfaces Comprising Metal Strips or Patches". In: *IEEE Transactions on Antennas and Propagation* 56.6 (June 2008), pp. 1624–1632. ISSN: 0018-926X. DOI: 10.1109/TAP.2008.923327 (cit. on p. 68).

[77] Susumu Noda, Masayuki Fujita, and Takashi Asano. "Spontaneous-emission control by photonic crystals and nanocavities". In: *Nature Photonics* 1.8 (2007), pp. 449–458 (cit. on p. 69).

[78] Ulrich Hoeppe, Christian Wolff, Jens Küchenmeister, Jens Niegemann, Malte Drescher, Hartmut Benner, and Kurt Busch. "Direct observation of non-Markovian radiation dynamics in 3D bulk photonic crystals". In: *Physical Review Letters* 108.4 (2012), p. 043603 (cit. on p. 69).

[79] K Kounoike, M Yamaguchi, M Fujita, T Asano, J Nakanishi, and S Noda. "Investigation of spontaneous emission from quantum dots embedded in two-dimensional photonic-crystal slab". In: *Electronics Letters* 41.25 (2005), pp. 1402–1403 (cit. on p. 69).

[80] R Iliew, C Etrich, U Peschel, F Lederer, M Augustin, H-J Fuchs, D Schelle, E-B Kley, S Nolte, and A Tünnermann. "Diffractionless propagation of light in a low-index photonic-crystal film". In: *Applied Physics Letters* 85.24 (2004), pp. 5854–5856 (cit. on p. 69).

[81] Hideo Kosaka, Takayuki Kawashima, Akihisa Tomita, Masaya Notomi, Toshiaki Tamamura, Takashi Sato, and Shojiro Kawakami. "Self-collimating phenomena in photonic crystals". In: *Applied Physics Letters* 74.9 (1999), pp. 1212–1214 (cit. on pp. 69, 71).

[82] Peter T. Rakich, Marcus S. Dahlem, Sheila Tandon, Mihai Ibanescu, Marin Soljačić, Gale S. Petrich, John D. Joannopoulos, Leslie A. Kolodziejski, and Erich P. Ippen. "Achieving centimetre-scale supercollimation in a large-area two-dimensional photonic crystal". en. In: *Nature Materials* 5.2 (Feb. 2006), pp. 93–96. ISSN: 1476-1122, 1476-4660 (cit. on p. 69).

[83] Xiaofang Yu and Shanhui Fan. "Bends and splitters for self-collimated beams in photonic crystals". In: *Applied Physics Letters* 83.16 (2003), pp. 3251–3253 (cit. on pp. 69, 94).

[84] Boris Gralak, Stefan Enoch, and Gérard Tayeb. "Anomalous refractive properties of photonic crystals". en. In: *Journal of the Optical Society of America A* 17.6 (June 2000), pp. 1012–1020. ISSN: 1084-7529, 1520-8532 (cit. on p. 69).

[85] Aaron F. Matthews, Steven K. Morrison, and Yuri S. Kivshar. "Self-collimation and beam splitting in low-index photonic crystals". en. In: *Optics Communications* 279.2 (Nov. 2007), pp. 313–319. ISSN: 00304018 (cit. on p. 69).

[86] Zhaolin Lu, C.A. Schuetz, Shouyuan Shi, Caihua Chen, G.P. Behrmann, and D.W. Prather. "Experimental demonstration of self-collimation in low-index-contrast photonic crystals in the millimeter-wave regime". In: *IEEE Transactions on Microwave Theory and Techniques* 53.4 (Apr. 2005), pp. 1362–1368. ISSN: 0018-9480 (cit. on pp. 69, 94).

[87] Zhaolin Lu, Shouyuan Shi, Janusz A. Murakowski, Garrett J. Schneider, Christopher A. Schuetz, and Dennis W. Prather. "Experimental Demonstration of Self-Collimation inside a Three-Dimensional Photonic Crystal". en. In: *Physical Review Letters* 96.17 (May 2006), p. 173902. ISSN: 0031-9007, 1079-7114 (cit. on p. 69).

[88] Harish N. S. Krishnamoorthy, Zubin Jacob, Evgenii Narimanov, Ilona Kretzschmar, and Vinod M. Menon. “Topological Transitions in Metamaterials”. en. In: *Science* 336.6078 (Apr. 2012), pp. 205–209. ISSN: 0036-8075, 1095-9203. DOI: 10.1126/science.1219171 (cit. on p. 70).

[89] Alexey A. Orlov, Sergei V. Zhukovsky, Ivan V. Iorsh, and Pavel A. Belov. “Controlling light with plasmonic multilayers”. en. In: *Photonics and Nanostructures - Fundamentals and Applications* 12.3 (June 2014), pp. 213–230. ISSN: 15694410. DOI: 10.1016/j.photonics.2014.03.003 (cit. on p. 70).

[90] L. Brillouin. “Les électrons libres dans les métaux et le role des réflexions de Bragg”. In: *Journal de Physique et le Radium* 1.11 (1930), pp. 377–400. ISSN: 0368-3842. DOI: 10.1051/jphysrad:01930001011037700. URL: http://www.edpsciences.org/10.1051/jphysrad:01930001011037700 (cit. on p. 70).

[91] Oleh Yermakov, Vladimir Lenets, Andrey Sayanskiy, Juan Baena, Enrica Martini, Stanislav Glybovski, and Stefano Maci. “Surface Waves on Self-Complementary Metasurfaces: All-Frequency Hyperbolicity, Extreme Canalization, and TE-TM Polarization Degeneracy”. en. In: *Physical Review X* 11.3 (Aug. 2021), p. 031038. ISSN: 2160-3308. DOI: 10.1103/PhysRevX.11.031038 (cit. on pp. 71, 73, 76, 77, 94, 97).

[92] Pengcheng Huo, Si Zhang, Yuzhang Liang, Yanqing Lu, and Ting Xu. “Hyperbolic Metamaterials and Metasurfaces: Fundamentals and Applications”. en. In: *Advanced Optical Materials* 7.14 (July 2019), p. 1801616. ISSN: 2195-1071, 2195-1071. DOI: 10.1002/adom.201801616 (cit. on pp. 71, 72).

[93] Alexander Poddubny, Ivan Iorsh, Pavel Belov, and Yuri Kivshar. “Hyperbolic metamaterials”. en. In: *Nature Photonics* 7.12 (Dec. 2013), pp. 948–957. ISSN: 1749-4885, 1749-4893. DOI: 10.1038/nphoton.2013.243 (cit. on p. 71).

[94] Prashant Shekhar, Jonathan Atkinson, and Zubin Jacob. “Hyperbolic metamaterials: fundamentals and applications”. en. In: *Nano Convergence* 1.1 (Dec. 2014), p. 14. ISSN: 2196-5404. DOI: 10.1186/s40580-014-0014-6 (cit. on p. 71).

[95] O. Y. Yermakov, A. I. Ovcharenko, M. Song, A. A. Bogdanov, I. V. Iorsh, and Yu. S. Kivshar. “Hybrid waves localized at hyperbolic metasurfaces”. en. In: *Physical Review B* 91.23 (June 2015), p. 235423. ISSN: 1098-0121, 1550-235X. DOI: 10.1103/PhysRevB.91.235423 (cit. on p. 71).

[96] J. Sebastian Gomez-Diaz, Mykhailo Tymchenko, and Andrea Alù. “Hyperbolic Plasmons and Topological Transitions Over Uniaxial Metasurfaces”. en. In: *Physical Review Letters* 114.23 (June 2015), p. 233901. ISSN: 0031-9007, 1079-7114. DOI: 10.1103/PhysRevLett.114.233901 (cit. on p. 71).

[97] Alexander A. High, Robert C. Devlin, Alan Dibos, Mark Polking, Dominik S. Wild, Janos Perczel, Nathalie P. De Leon, Mikhail D. Lukin, and Hongkun Park. "Visible-frequency hyperbolic metasurface". en. In: *Nature* 522.7555 (June 2015), pp. 192–196. ISSN: 0028-0836, 1476-4687. DOI: 10.1038/nature14477 (cit. on p. 71).

[98] Andrei Nemilentsau, Tobias Stauber, Guillermo Gómez-Santos, Mitchell Luskin, and Tony Low. "Switchable and unidirectional plasmonic beacons in hyperbolic two-dimensional materials". en. In: *Physical Review B* 99.20 (May 2019), p. 201405. ISSN: 2469-9950, 2469-9969. DOI: 10.1103/PhysRevB.99.201405 (cit. on p. 71).

[99] Zubin Jacob, Leonid V. Alekseyev, and Evgenii Narimanov. "Optical Hyperlens: Far-field imaging beyond the diffraction limit". en. In: *Optics Express* 14.18 (2006), p. 8247. ISSN: 1094-4087. DOI: 10.1364/OE.14.008247 (cit. on p. 71).

[100] J. S. Gomez-Diaz and Andrea Alù. "Flatland Optics with Hyperbolic Metasurfaces". en. In: *ACS Photonics* 3.12 (Dec. 2016), pp. 2211–2224. ISSN: 2330-4022, 2330-4022. DOI: 10.1021/acsphotonics.6b00645 (cit. on p. 71).

[101] Alessandro Tuniz, Korbinian J Kaltenecker, Bernd M Fischer, Markus Walther, Simon C Fleming, Alexander Argyros, and Boris T Kuhlmey. "Metamaterial fibres for subdiffraction imaging and focusing at terahertz frequencies over optically long distances". In: *Nature Communications* 4.1 (2013), p. 2706 (cit. on p. 71).

[102] Dylan Lu, Jimmy J. Kan, Eric E. Fullerton, and Zhaowei Liu. "Enhancing spontaneous emission rates of molecules using nanopatterned multilayer hyperbolic metamaterials". en. In: *Nature Nanotechnology* 9.1 (Jan. 2014), pp. 48–53. ISSN: 1748-3387, 1748-3395. DOI: 10.1038/nnano.2013.276 (cit. on p. 71).

[103] Siyuan Dai et al. "Manipulation and Steering of Hyperbolic Surface Polaritons in Hexagonal Boron Nitride". en. In: *Advanced Materials* 30.16 (Apr. 2018), p. 1706358. ISSN: 0935-9648, 1521-4095. DOI: 10.1002/adma.201706358 (cit. on p. 71).

[104] Peining Li, Irene Dolado, Francisco Javier Alfaro-Mozaz, Fèlix Casanova, Luis E. Hueso, Song Liu, James H. Edgar, Alexey Y. Nikitin, Saül Vélez, and Rainer Hillenbrand. "Infrared hyperbolic metasurface based on nanostructured van der Waals materials". en. In: *Science* 359.6378 (Feb. 2018), pp. 892–896. ISSN: 0036-8075, 1095-9203. DOI: 10.1126/science.aaq1704 (cit. on p. 71).

[105] Alyona V. Chshelokova, Polina V. Kapitanova, Alexander N. Poddubny, Dmitry S. Filonov, Alexey P. Slobozhanyuk, Yuri S. Kivshar, and Pavel A. Belov. "Hyperbolic transmission-line metamaterials". en. In: *Journal of Applied Physics* 112.7 (Oct. 2012), p. 073116. ISSN: 0021-8979, 1089-7550. DOI: 10.1063/1.4758287 (cit. on p. 71).

[106] Mingze He, Thomas G. Folland, Jiahua Duan, Pablo Alonso-González, Simone De Liberato, Alexander Paarmann, and Joshua D. Caldwell. "Anisotropy and Modal Hybridization in Infrared Nanophotonics Using Low-Symmetry Materials". en. In: *ACS Photonics* 9.4 (Apr. 2022), pp. 1078–1095. ISSN: 2330-4022, 2330-4022. DOI: 10.1021/acsphotonics.1c01486 (cit. on p. 73).

[107] Oleh Y. Yermakov, Anna A. Hurshkainen, Dmitry A. Dobrykh, Polina V. Kapitanova, Ivan V. Iorsh, Stanislav B. Glybovski, and Andrey A. Bogdanov. "Experimental observation of hybrid TE-TM polarized surface waves supported by a hyperbolic metasurface". en. In: *Physical Review B* 98.19 (Nov. 2018), p. 195404. ISSN: 2469-9950, 2469-9969 (cit. on pp. 77, 94).

[108] Rahul Deshmukh, Svend-Age Biehs, Emaad Khwaja, Tal Galfsky, Girish S. Agarwal, and Vinod M. Menon. "Long-Range Resonant Energy Transfer Using Optical Topological Transitions in Metamaterials". en. In: *ACS Photonics* 5.7 (July 2018), pp. 2737–2741. ISSN: 2330-4022, 2330-4022 (cit. on p. 79).

[109] Afsaneh Saee Arezoomand, Ferdows B. Zarrabi, Samaneh Heydari, and Navid P. Gandji. "Independent polarization and multi-band THz absorber base on Jerusalem cross". en. In: *Optics Communications* 352 (Oct. 2015), pp. 121–126. ISSN: 00304018. DOI: 10.1016/j.optcom.2015.05.003 (cit. on p. 79).

[110] Se-Mi Kim, Celso M. Leite, Ju-Yeong Park, Hyo-Jeong Kim, and Jae-Hyung Jang. "Multiband Terahertz Self-Complementary Metasurface". In: *IEEE Access* 8 (2020), pp. 199051–199059. ISSN: 2169-3536. DOI: 10.1109/ACCESS.2020.3034120 (cit. on p. 79).

[111] Guo-Dong Wang, Ming-Hai Liu, Xi-Wei Hu, Ling-Hua Kong, Li-Li Cheng, and Zhao-Quan Chen. "Multi-band microwave metamaterial absorber based on coplanar Jerusalem crosses". In: *Chinese Physics B* 23.1 (Jan. 2014), p. 017802. ISSN: 1674-1056. DOI: 10.1088/1674-1056/23/1/017802 (cit. on p. 80).

[112] Alexey I. Chizhik, Jan Rother, Ingo Gregor, Andreas Janshoff, and Jörg Enderlein. "Metal-induced energy transfer for live cell nanoscopy". en. In: *Nature Photonics* 8.2 (Feb. 2014), pp. 124–127. ISSN: 1749-4885, 1749-4893 (cit. on p. 85).

[113] Andrea G Markelz and Daniel M Mittleman. "Perspective on terahertz applications in bioscience and biotechnology". In: *ACS Photonics* 9.4 (2022), pp. 1117–1126 (cit. on p. 93).

[114] O.A. Smolyanskaya et al. "Terahertz biophotonics as a tool for studies of dielectric and spectral properties of biological tissues and liquids". In: *Progress in Quantum Electronics* 62 (2018), pp. 1–77 (cit. on p. 93).

[115] Geon Lee, Jinwoo Lee, Q-Han Park, and Minah Seo. "Frontiers in Terahertz Imaging Applications beyond Absorption Cross-Section and Diffraction Limits". In: *ACS Photonics* 9.5 (2022), pp. 1500–1512 (cit. on p. 93).

[116] Changwon Seo and Teun-Teun Kim. “Terahertz near-field spectroscopy for various applications”. In: *Journal of the Korean Physical Society* 81 (2022), pp. 549–561. ISSN: 0374-4884 (cit. on p. 93).

[117] Peter H Siegel. “THz instruments for space”. In: *IEEE Transactions on Antennas and Propagation* 55.11 (2007), pp. 2957–2965 (cit. on p. 93).

[118] Thomas Kleine-Ostmann and Tadao Nagatsuma. “A review on terahertz communications research”. In: *Journal of Infrared, Millimeter, and Terahertz Waves* 32 (2011), pp. 143–171 (cit. on p. 93).

[119] Shang-Hua Yang and Mona Jarrahi. “Navigating terahertz spectrum via photomixing”. In: *Optics and Photonics News* 31.7 (2020), pp. 36–43 (cit. on p. 93).

[120] Milad Tatar Mamaghani and Yi Hong. “Aerial intelligent reflecting surface-enabled terahertz covert communications in beyond-5G Internet of Things”. In: *IEEE Internet of Things Journal* 9.19 (2022), pp. 19012–19033 (cit. on p. 93).

[121] Daniel Headland, Withawat Withayachumnankul, Masayuki Fujita, and Tadao Nagatsuma. “Gratingless integrated tunneling multiplexer for terahertz waves”. en. In: *Optica* 8.5 (May 2021), p. 621. ISSN: 2334-2536 (cit. on p. 93).

[122] Zhen Tan, Qin-Yi Zhang, Ya-Lin Lei, Yun Zhao, and Jiang-Qiao Ding. “Terahertz waveguide multiplexers: A review”. en. In: *Microwave and Optical Technology Letters* 65.7 (July 2023), pp. 1925–1935. ISSN: 0895-2477, 1098-2760 (cit. on p. 93).

[123] Jianjun Ma, Rabi Shrestha, Lothar Moeller, and Daniel M Mittleman. “Invited article: Channel performance for indoor and outdoor terahertz wireless links”. In: *APL Photonics* 3.5 (2018), p. 051601 (cit. on p. 93).

[124] John F Federici, Jianjun Ma, and Lothar Moeller. “Review of weather impact on outdoor terahertz wireless communication links”. In: *Nano Communication Networks* 10 (2016), pp. 13–26 (cit. on p. 93).

[125] Rabi Shrestha, Hichem Guerboukha, Zhaoji Fang, Edward Knightly, and Daniel M Mittleman. “Jamming a terahertz wireless link”. In: *Nature Communications* 13.1 (2022), p. 3045 (cit. on p. 93).

[126] Haymen Shams and Alwyn Seeds. “Photonics, fiber and THz wireless communication”. In: *Optics and Photonics News* 28.3 (2017), pp. 24–31 (cit. on p. 93).

[127] Radoslaw Piesiewicz, Martin Jacob, Martin Koch, Joerg Schoebel, and Thomas Kurner. “Performance analysis of future multigigabit wireless communication systems at THz frequencies with highly directive antennas in realistic indoor environments”. In: *IEEE Journal of selected topics in quantum electronics* 14.2 (2008), pp. 421–430 (cit. on p. 93).

[128] Kazuisao Tsuruda, Masayuki Fujita, and Tadao Nagatsuma. “Extremely low-loss terahertz waveguide based on silicon photonic-crystal slab”. In: *Optics Express* 23.25 (2015), pp. 31977–31990 (cit. on p. 93).

[129] Yihao Yang, Yuichiro Yamagami, Xiongbin Yu, Prakash Pitchappa, Julian Webber, Baile Zhang, Masayuki Fujita, Tadao Nagatsuma, and Ranjan Singh. “Terahertz topological photonics for on-chip communication”. In: *Nature Photonics* 14.7 (2020), pp. 446–451 (cit. on p. 93).

[130] Daniel Headland, Withawat Withayachumnankul, Xiongbin Yu, Masayuki Fujita, and Tadao Nagatsuma. “Unclad microphotonics for terahertz waveguides and systems”. In: *Journal of Lightwave Technology* 38.24 (2020), pp. 6853–6862 (cit. on p. 93).

[131] P Uhd Jepsen, David G Cooke, and Martin Koch. “Terahertz spectroscopy and imaging–Modern techniques and applications”. In: *Laser & Photonics Reviews* 5.1 (2011), pp. 124–166 (cit. on p. 93).

[132] M Weidenbach, D Jahn, A Rehn, SF Busch, F Beltrán-Mejıa, JC Balzer, and M Koch. “3D printed dielectric rectangular waveguides, splitters and couplers for 120 GHz”. In: *Optics Express* 24.25 (2016), pp. 28968–28976 (cit. on p. 93).

[133] Masahiro Yata, Masayuki Fujita, and Tadao Nagatsuma. “Photonic-crystal diplexers for terahertz-wave applications”. In: *Optics Express* 24.7 (2016), pp. 7835–7849 (cit. on p. 93).

[134] Yang Cao, Kathirvel Nallappan, Guofu Xu, and Maksim Skorobogatiy. “Add drop multiplexers for terahertz communications using two-wire waveguide-based plasmonic circuits”. In: *Nature Communications* 13.1 (2022), p. 4090 (cit. on p. 93).

[135] Jianming Dai, Jiangquan Zhang, Weili Zhang, and Daniel Grischkowsky. “Terahertz time-domain spectroscopy characterization of the far-infrared absorption and index of refraction of high-resistivity, float-zone silicon”. In: *Journal of the Optical Society of America B* 21.7 (2004), pp. 1379–1386 (cit. on pp. 93, 100).

[136] Claudia Brückner, Thomas Käsebier, Boris Pradarutti, Stefan Riehemann, Gunther Notni, Ernst-Bernhard Kley, and Andreas Tünnermann. “Broadband antireflective structures applied to high resistive float zone silicon in the THz spectral range”. In: *Optics Express* 17.5 (2009), pp. 3063–3077 (cit. on pp. 93, 95).

[137] Daniel Headland, Withawat Withayachumnankul, Masayuki Fujita, and Tadao Nagatsuma. “Gratingless integrated tunneling multiplexer for terahertz waves”. In: *Optica* 8.5 (2021), pp. 621–629 (cit. on p. 93).

[138] Longqing Cong, Yogesh Kumar Srivastava, Huifang Zhang, Xueqian Zhang, Jiaguang Han, and Ranjan Singh. “All-optical active THz metasurfaces for ultrafast polarization switching and dynamic beam splitting”. In: *Light: Science & Applications* 7.1 (2018), p. 28 (cit. on p. 94).

[139] Wanying Liu, Quanlong Yang, Quan Xu, Xiaohan Jiang, Tong Wu, Kemeng Wang, Jianqiang Gu, Jiaguang Han, and Weili Zhang. “Multifunctional All-Dielectric Metasurfaces for Terahertz Multiplexing”. In: *Advanced Optical Materials* 9.19 (2021), p. 2100506 (cit. on p. 94).

[140] Su-Peng Yu, Juan A Muniz, Chen-Lung Hung, and HJ Kimble. "Two-dimensional photonic crystals for engineering atom–light interactions". In: *Proceedings of the National Academy of Sciences* 116.26 (2019), pp. 12743–12751 (cit. on pp. 94, 95, 101, 112).

[141] Aaron F Matthews. "Experimental demonstration of self-collimation beaming and splitting in photonic crystals at microwave frequencies". In: *Optics Communications* 282.9 (2009), pp. 1789–1792 (cit. on p. 94).

[142] J Trull, Lina Maigyte, V Mizeikis, M Malinauskas, Saulius Juodkazis, Crina Cojocaru, Marius Rutkauskas, Martynas Peckus, Valdas Sirutkaitis, and Kestutis Staliunas. "Formation of collimated beams behind the woodpile photonic crystal". In: *Physical Review A* 84.3 (2011), p. 033812 (cit. on p. 94).

[143] Irfan Bulu, Humeyra Caglayan, and Ekmel Ozbay. "Highly directive radiation from sources embedded inside photonic crystals". In: *Applied Physics Letters* 83.16 (2003), pp. 3263–3265 (cit. on p. 94).

[144] Salih Yarga, Kubilay Sertel, and John L Volakis. "Degenerate band edge crystals for directive antennas". In: *IEEE transactions on antennas and propagation* 56.1 (2008), pp. 119–126 (cit. on p. 94).

[145] Irfan Bulu, Humeyra Caglayan, Koray Aydin, and Ekmel Ozbay. "Compact size highly directive antennas based on the SRR metamaterial medium". In: *New Journal of Physics* 7.1 (2005), p. 223 (cit. on p. 94).

[146] Dmitry Chigrin, Stefan Enoch, Clivia Sotomayor Torres, and Gérard Tayeb. "Self-guiding in two-dimensional photonic crystals". en. In: *Optics Express* 11.10 (May 2003), p. 1203. ISSN: 1094-4087. DOI: 10.1364/OE.11.001203. URL: https://opg.optica.org/oe/abstract.cfm?uri=oe-11-10-1203 (cit. on pp. 94, 95).

[147] Momchil Minkov, Ian AD Williamson, Lucio C Andreani, Dario Gerace, Beicheng Lou, Alex Y Song, Tyler W Hughes, and Shanhui Fan. "Inverse design of photonic crystals through automatic differentiation". In: *ACS Photonics* 7.7 (2020), pp. 1729–1741 (cit. on p. 95).

[148] John D. Joannopoulos, Steven G. Johnson, Joshua N. Winn, and Robert D. Meade. *Photonic Crystals: Molding the Flow of Light (Second Edition)*. Princeton University Press, 2008. Chap. 8 (cit. on p. 95).

[149] *Protemics website*. https://www.protemics.com/. [Accessed: 27-October-2022] (cit. on p. 96).

[150] Quanlong Yang, Dongyang Wang, Sergey Kruk, Mingkai Liu, Ivan Kravchenko, Jiaguang Han, Yuri Kivshar, and Ilya Shadrivov. "Topology-empowered membrane devices for terahertz photonics". In: *Advanced Photonics* 4.4 (2022), p. 046002 (cit. on p. 97).

[151] Niels JJ van Hoof, Diego R Abujetas, Stan ET Ter Huurne, Francesco Verdelli, Giel CA Timmermans, José A Sánchez-Gil, and Jaime Gómez Rivas. "Unveiling the Symmetry Protection of Bound States in the Continuum with Terahertz Near-Field Imaging". In: *ACS Photonics* 8.10 (2021), pp. 3010–3016 (cit. on p. 97).

[152] Biao Yang, Qinghua Guo, Ben Tremain, Rongjuan Liu, Lauren E Barr, Qinghui Yan, Wenlong Gao, Hongchao Liu, Yuanjiang Xiang, Jing Chen, et al. "Ideal Weyl points and helicoid surface states in artificial photonic crystal structures". In: *Science* 359.6379 (2018), pp. 1013–1016 (cit. on p. 97).

[153] Fuxin Guan, Xiangdong Guo, Kebo Zeng, Shu Zhang, Zhaoyu Nie, Shaojie Ma, Qing Dai, John Pendry, Xiang Zhang, and Shuang Zhang. "Overcoming losses in superlenses with synthetic waves of complex frequency". In: *Science* 381.6659 (2023), pp. 766–771 (cit. on p. 97).

[154] Alessio Stefani, Boris T. Kuhlmey, Justin Digweed, Benjamin Davies, Zizhen Ding, Hala Zreiqat, Mohammad Mirkhalaf, and Alessandro Tuniz. "Flexible Terahertz Photonic Light-Cage Modules for In-Core Sensing and High Temperature Applications". en. In: *ACS Photonics* 9.6 (June 2022), pp. 2128–2141. ISSN: 2330-4022, 2330-4022 (cit. on p. 97).

[155] Arthur Yaghjian. "An overview of near-field antenna measurements". In: *IEEE Transactions on antennas and propagation* 34.1 (1986), pp. 30–45 (cit. on p. 105).

[156] L Stryer and R P Haugland. "Energy transfer: a spectroscopic ruler." en. In: *Proceedings of the National Academy of Sciences* 58.2 (Aug. 1967), pp. 719–726. ISSN: 0027-8424, 1091-6490. DOI: 10.1073/pnas.58.2.719 (cit. on p. 110).

[157] OV Kibis, G Ya Slepyan, SA Maksimenko, and A Hoffmann. "Matter coupling to strong electromagnetic fields in two-level quantum systems with broken inversion symmetry". In: *Physical Review Letters* 102.2 (2009), p. 023601 (cit. on p. 112).

[158] Caspar Groiseau, Antonio I Fernández Domınguez, Diego Martın Cano, and Carlos Sánchez Muñoz. *Single-photon source over the terahertz regime*. 19 May 2023. arXiv:2305.11754. (Accessed: 2023-09-01) (cit. on p. 112).

[159] S. Enoch, A. Gola, P. Lecoq, and A. Rivetti. "Design considerations for a new generation of SiPMs with unprecedented timing resolution". In: *Journal of Instrumentation* 16.02 (Feb. 2021), P02019–P02019. ISSN: 1748-0221. DOI: 10.1088/1748-0221/16/02/P02019. URL: https://iopscience.iop.org/article/10.1088/1748-0221/16/02/P02019 (cit. on p. 113).